

Modelling Blade Loads in Industry-Scale Large-Eddy Simulations of Wind Farms using an Analytical Body Force Model

Thesis Aerodynamics & Wind Energy
I. Janssen

Modelling Blade Loads in Industry-Scale Large-Eddy Simulations of Wind Farms

using an Analytical Body Force Model

by

I. Janssen

to obtain the degree of Master of Science
at the Delft University of Technology,
to be defended publicly on Monday July 7, 2025 at 09:00 AM.

| | |
|---------------------|--|
| Student number: | 4660900 |
| Project duration: | October 14, 2024 – July 7, 2025 |
| Thesis supervisors: | Dr. W. Yu, TU Delft Dr. M. Folkersma, Whiffle |
| Thesis committee: | Prof. Dr. D.A. von Terzi, TU Delft, Chair Dr.Ir. A.H. van Zuijlen, TU Delft, Examiner |

Cover: Genesal Energy wind turbine[20]

An electronic version of this thesis is available at <http://repository.tudelft.nl/>.

Preface

Just like the wind, life can be turbulent, unpredictable and full of forces we cannot control. Yet, through dedication, passion, and ingenuity, we can find a way to harness its power and deal with the loads.

I would like to thank my supervisors, Wei and Mikko, for all the guidance throughout this project. Their advice brought order to the chaos and helped me find direction when I had drifted off course.

On a personal note, I would like to thank my friends and family for their support, whether the atmosphere was calm or shifting. Their encouragement and belief meant a great deal to me during all stages of this journey.

*I. Janssen
Delft, June 2025*

Summary

Increases in computational power have enabled the growing use of Large Eddy Simulations (LES) for high-fidelity wind farm modelling. These simulations typically rely on Blade Element Momentum (BEM) methods to accurately represent the turbine forces. However, use of BEM in industry is often impossible, as the required turbine geometry is confidential. This limits industry-scale LES to the use of uniform Actuator Disk Models, which cannot resolve the force distribution over the rotor.

This thesis explored the use of Analytical Body Force Models (ABFM) to compute the blade forces within LES, requiring only limited knowledge of the turbine geometry. The ABFM was used to compute the axial and azimuthal force distributions over the rotor disk based on a turbine operating condition. For a given average disk velocity, these operating conditions were obtained from a calibration using the characteristic turbine curves. For uniform inflows, an analytical solution existed, denoted as ABFM-H.

To resolve non-uniform inflows, the ABFM was coupled to the LES by supplying it with the velocity distribution over the rotor disk, including rotor self-induction. Two coupling strategies were proposed. For the two-way coupled ABFM-2W, the computed forces were projected back into the LES to simulate the turbine. The ABFM-1W was one-way coupled, representing the turbine in the LES as a uniform Actuator Disk.

Verification showed that the ABFM-H could correctly reproduce the results of literature. Further investigation confirmed that the ABFM-1W and ABFM-2W converged to the same solution as the ABFM-H for uniform inflow, although some numerical artifacts were observed in the azimuthal force. For uniform inflow, all ABFM models compared well to BEM for velocities up to rated. Above rated velocity, the accuracy decreased, especially for the axial force. Nevertheless, the main trends could still be captured.

The model was tested under increasingly complex inflow conditions. For sheared inflow the time-averaged loading remained consistent with BEM, especially for the ABFM-2W. However, azimuthal fluctuations in loading due to changes in thrust and power at sub-revolution timescales could not be resolved. In partially waked inflows both ABFM-1W and ABFM-2W resolved the mean loading distribution, but only the ABFM-2W successfully captured the standard deviation. The difference was caused by wake characteristics: the wake of the ABFM-1W exhibited significant numerical smoothing, whereas the ABFM-2W showed a more distinct boundary between wake and ambient flow and captured the root vortex. As a result the ABFM-2W wake exhibited a higher turbulence intensity.

While the proposed methodology provided reasonable estimates for the force distributions for different inflow conditions, several areas of improvement remain. It should be investigated whether numerical artifacts can be further reduced when sampling the disk velocity distribution. Higher accuracy could also be achieved if the freestream velocity could be estimated with less uncertainty. Further improvements of the model refer to its ability to resolve more complex flow cases, including corrections for yawed flow, integration of a turbine controller within the LES, and coupling to a structural solver to assess aeroelastic effects.

Contents

| | |
|---|-------------|
| Preface | i |
| Summary | ii |
| List of Figures | iv |
| List of Tables | viii |
| Nomenclature | x |
| 1 Introduction | 1 |
| 2 Literature Review | 3 |
| 2.1 Individual Turbine Analysis | 3 |
| 2.1.1 Blade Element Momentum Theory | 3 |
| 2.1.2 Vortex Models | 5 |
| 2.1.3 Blade Resolved CFD | 6 |
| 2.1.4 CFD with Actuator Models | 8 |
| 2.2 Wind Farm Analysis | 13 |
| 2.2.1 Atmospheric Modeling | 13 |
| 2.2.2 Turbine Interactions on Farm Level | 14 |
| 2.2.3 The ASPIRE solver | 15 |
| 2.3 State-of-the-art | 17 |
| 2.3.1 Applications of LES to Wind Farms | 17 |
| 2.3.2 Challenges in Industry | 20 |
| 2.4 Goals of the thesis | 21 |
| 2.4.1 Research Questions | 21 |
| 2.4.2 Hypothesis | 22 |
| 3 Methodology | 23 |
| 3.1 The Analytical Body Force Model | 23 |
| 3.1.1 Load Model Formulation | 24 |
| 3.1.2 ABFM Solution for Homogeneous Flows | 26 |
| 3.1.3 Accounting for Non-homogeneous Conditions | 27 |
| 3.1.4 Load Model Discretisation | 29 |
| 3.1.5 Determination of Blade Loads | 30 |
| 3.2 Turbine Operating Conditions | 30 |
| 3.2.1 Turbine Curve Parametrization | 30 |
| 3.2.2 Calibration of Freestream Velocity | 32 |
| 3.2.3 Time Scales | 33 |
| 3.3 Coupling Strategies | 33 |
| 3.3.1 Coordinate Transformations | 33 |
| 3.3.2 One-way Coupling | 35 |
| 3.3.3 Two-way Coupling | 36 |
| 3.3.4 Numerical Setup of the LES | 38 |
| 4 Verification | 41 |
| 4.1 Implementation of the ABFM | 41 |
| 4.1.1 Evaluating the Tip Correction | 41 |
| 4.1.2 Verification of Non-dimensional distributions | 42 |
| 4.1.3 Comparison of ABFM-H and BEM | 43 |
| 4.1.4 Numerical Errors of the Discretized ABFM | 44 |

| | | |
|----------|--|-----------|
| 4.2 | Accuracy of the ABFM-1W in Uniform Flow | 46 |
| 4.2.1 | Obtaining the Reference Velocity | 46 |
| 4.2.2 | Consistency in the Degrees of Freedom | 47 |
| 4.2.3 | Evaluation of Disk Parameters | 48 |
| 4.2.4 | Evaluation of Blade Loading | 49 |
| 4.3 | Verification of the ABFM-2W | 50 |
| 4.3.1 | Equivalence of the Force Projection | 50 |
| 4.3.2 | Consistency of the degrees of freedom | 52 |
| 4.3.3 | Reconstruction of the Disk Velocity | 53 |
| 4.3.4 | Accuracy of the Force Distributions | 54 |
| 5 | Results and Discussion | 56 |
| 5.1 | Reconstruction of Turbine Operating Conditions | 56 |
| 5.1.1 | Turbine Thrust | 56 |
| 5.1.2 | Turbine Power | 57 |
| 5.2 | Evaluation of Blade Force Distributions | 58 |
| 5.2.1 | Uniform Flows | 58 |
| 5.2.2 | Sheared Flows | 60 |
| 5.3 | Comparison of Wake Characteristics | 63 |
| 5.3.1 | Uniform Inflow at Rated Velocity | 63 |
| 5.3.2 | Sheared Inflow at Rated Velocity | 66 |
| 5.3.3 | Uniform Inflow at 20m/s | 69 |
| 5.4 | Application to Turbines with a Partially Waked Inflow | 71 |
| 6 | Conclusion | 75 |
| 7 | Recommendations for Future Work | 76 |
| | References | 78 |
| A | Understanding the ABFM Induction | 84 |
| A.1 | Induction Modeling using the ABFM | 84 |
| A.2 | Consequences for Coupling the ABFM | 86 |
| A.2.1 | Understanding the Coupling Procedure of Current Literature | 87 |
| A.2.2 | Generalising the Coupling Procedure | 87 |
| B | BEM Model | 89 |

List of Figures

| | | |
|------|--|----|
| 1.1 | Costs per kWh of different renewables, compared to fossil fuels. Graphic obtained from IRENA[30]. | 1 |
| 1.2 | Average capacity of on-shore and off-shore wind turbines in the period 2014-2023. Graphic obtained from Wind Europe[89] | 2 |
| 2.1 | A Blade Element with its corresponding force and angle definitions. Graphic obtained from [73]. | 4 |
| 2.2 | Lifting Line representation of a wing. Figure obtained from Anderson[2] | 6 |
| 2.3 | Free wake representation of vortex filaments. Figure obtained from Van den Broek et al.[8] | 6 |
| 2.4 | Incorporating the rotor geometry into the mesh. Figure obtained from Sitaraman[68] | 7 |
| 2.5 | The distribution of axial velocity in the rotor disc (A) and iso surfaces of vorticity of the tip and root vortex (B) for an AL method. Figure obtained from Zhao et al.[99] | 10 |
| 2.6 | Comparison of the body force distribution obtained from AL (a), AS (b) and AD(c). Figure obtained from Mohammadi et al.[44] | 12 |
| 2.7 | The numerical grid for discretisation of the equations. Figure obtained from the ASPIRE documentation[85] | 16 |
| 3.1 | Inputs and outputs of the ABFM | 23 |
| 3.2 | The cylindrical axis system of the ABFM | 24 |
| 3.3 | Side view of the rotor disk displaying region 1 and region 2, infinitesimally upstream and downstream of the rotor, respectively | 24 |
| 3.4 | Discretisation of the rotor disk onto a polar grid. Each cell is specified using its inner and outer radius, angular span and cell midpoint | 29 |
| 3.5 | Division of a turbine power curve into four simple regions | 31 |
| 3.6 | Definition of the tilt angle α of the rotor, with respect to the z-axis of the LES and the local horizontal | 34 |
| 3.7 | Definition of the rotor yaw misalignment angle, χ , with respect to the LES grid | 34 |
| 3.8 | Flowchart of the ABFM-1W model used to obtain force distributions from the LES as a post-processing procedure | 35 |
| 3.9 | Interpolating LES results onto the ABFM grid. Gray dots represent the LES grid, red dots the ABFM grid. The blue dot is the ABFM point of interest and the green point indicates the nearest neighbour along each negative Cartesian direction. Other neighbors are indicated in cyan. | 36 |
| 3.10 | Interpolation to the (i, j) node of the ABFM grid by its 8 nearest neighbours on the LES grid. First interpolation along x gives points aa, ab, ba and bb . Then interpolation along y results in a and b . The value at (i, j) is then found by interpolating along z | 36 |
| 3.11 | Flowchart of the ABFM-2W model to obtain turbine force distributions from the LES and project them onto the grid | 36 |
| 3.12 | Smearing the rotor forces onto a cylinder by applying the convolution kernel $\eta(x_{ax}, \epsilon)$ | 37 |
| 3.13 | Visualisation of the computational domain for all simulations. Dimensions are given in term of the Rotor diameter | 39 |
| 3.14 | Achieved time-averaged freestream velocity profiles at the turbine location | 40 |
| 4.1 | Comparison of different tip corrections for a variety of cases. Blue: The Glauert tip correction of Equation 3.8 calculated using Equation 3.9. Orange: The Glauert tip correction of Equation 3.8 calculated using Equation 4.1. Green: The Prandtl tip correction of Equation 3.7. Case a: $C_T = 0.3, \lambda = 1$. Case b: $C_T = 0.3, \lambda = 3$. Case c: $C_T = 0.5, \lambda = 5$. Case d: $C_T = 0.9, \lambda = 9$ | 42 |

| | | |
|------|---|----|
| 4.2 | Non-dimensional azimuthal velocity distribution at $C_T = 0.3$, values from literature[75] indicated by crosses | 43 |
| 4.3 | Non-dimensional azimuthal velocity distribution at $C_T = 0.9$, values from literature[75] indicated by crosses | 43 |
| 4.4 | Non-dimensional rotor circulation for different thrust coefficients and tip-speed ratios, values from literature[75] indicated by crosses | 43 |
| 4.5 | Axial force coefficient for an IEA-15MW reference turbine operating at $5\frac{m}{s}$, $10.5\frac{m}{s}$ and $20\frac{m}{s}$. Solid lines: ABFM-H, dashed lines: BEM | 44 |
| 4.6 | Azimuthal force coefficient for an IEA-15MW reference turbine operating at $5\frac{m}{s}$, $10.5\frac{m}{s}$ and $20\frac{m}{s}$. Solid lines: ABFM-H, dashed lines: BEM | 44 |
| 4.7 | Convergence of the azimuthal force coefficient of the discretised ABFM for a uniform inflow at $10.5\frac{m}{s}$, as compared to the ABFM-H | 45 |
| 4.8 | Distribution of observed reference velocity of the ABFM-1W for a uniform inflow of $10.5\frac{m}{s}$ | 47 |
| 4.9 | Realised rotor induction of the ABFM-1W for a uniform inflow of $10.5\frac{m}{s}$, as compared to the ABFM-H | 47 |
| 4.10 | Realised ABFM disk velocity of the ABFM-1W for a uniform inflow of $10.5\frac{m}{s}$, as compared to the ABFM-H | 47 |
| 4.11 | Time-averaged disk velocity of the ABFM-1W for a uniform inflow of $10.5\frac{m}{s}$ | 48 |
| 4.12 | Visualisation of the force projection kernel of the ABFM-1W, the red circle indicates the edge of the rotor disk | 48 |
| 4.13 | Time-averaged axial force distribution of the ABFM-1W for a uniform inflow of $10.5\frac{m}{s}$ | 48 |
| 4.14 | Time-averaged azimuthal force distribution of the ABFM-1W for a uniform inflow of $10.5\frac{m}{s}$ | 48 |
| 4.15 | Time and azimuthally averaged axial force coefficient of the ABFM-1W for a uniform inflow of $10.5\frac{m}{s}$, as compared to the ABFM-H | 49 |
| 4.16 | Time and azimuthally averaged azimuthal force coefficient of the ABFM-1W for a uniform inflow of $10.5\frac{m}{s}$, as compared to the ABFM-H | 49 |
| 4.17 | Resulting force projection of a uniform loading using the force projection algorithm of subsection 3.3.3 with $N_r = 30$, $N_\theta = 60$ and $\Delta_{LES} = \frac{D}{8}$. All cells indicated with a dot are within 2.1% of the maximal loading | 51 |
| 4.18 | Resulting force projection of a uniform loading using the force projection algorithm of subsection 3.3.3 with $N_r = 10$, $N_\theta = 60$ and $\Delta_{LES} = \frac{D}{8}$. All cells indicated with a dot are within 3.5% of the maximal loading | 51 |
| 4.19 | Resulting force projection of a uniform loading using the force projection algorithm of subsection 3.3.3 with $N_r = 30$, $N_\theta = 30$ and $\Delta_{LES} = \frac{D}{8}$. All cells indicated with a dot are within 2.7% of the maximal loading | 52 |
| 4.20 | Resulting force projection of a uniform loading using the force projection algorithm of subsection 3.3.3 with $N_r = 30$, $N_\theta = 45$ and $\Delta_{LES} = \frac{D}{8}$. All cells indicated with a dot are within 0.8% of the maximal loading | 52 |
| 4.21 | Distribution of observed reference velocity of the ABFM-2W for a uniform inflow of $10.5\frac{m}{s}$ | 52 |
| 4.22 | Realised rotor induction of the ABFM-2W for a uniform inflow of $10.5\frac{m}{s}$, as compared to the ABFM-H | 53 |
| 4.23 | Realised ABFM disk velocity for the ABFM-2W for a uniform inflow of $10.5\frac{m}{s}$, as compared to the ABFM-H | 53 |
| 4.24 | Time-averaged disk velocity of the ABFM-2W for a uniform inflow of $10.5\frac{m}{s}$ | 53 |
| 4.25 | Time-averaged axial force distribution of the ABFM-2W for a uniform inflow of $10.5\frac{m}{s}$ | 54 |
| 4.26 | Time-averaged azimuthal force distribution of the ABFM-2W for a uniform inflow of $10.5\frac{m}{s}$ | 54 |
| 4.27 | Time and azimuthally averaged axial force coefficient of the ABFM-2W for a uniform inflow of $10.5\frac{m}{s}$ | 55 |
| 4.28 | Time and azimuthally averaged azimuthal force coefficient of the ABFM-2W for a uniform inflow of $10.5\frac{m}{s}$ | 55 |
| 5.1 | Distribution of thrust for the ABFM-1W and ABFM-2W, as compared to the BEM model of Appendix B for a uniform inflow at: $5\frac{m}{s}$ (left), $10.5\frac{m}{s}$ (middle) and $20\frac{m}{s}$ (right) | 56 |
| 5.2 | Distribution of thrust for the ABFM-1W and ABFM-2W, as compared to the BEM model of Appendix B for a sheared inflow at: $5\frac{m}{s}$ (left), $10.5\frac{m}{s}$ (middle) and $20\frac{m}{s}$ (right) | 57 |

| | | |
|------|--|----|
| 5.3 | Distribution of power for the ABFM-1W and ABFM-2W, as compared to the BEM model of Appendix B for a uniform inflow at: $5 \frac{m}{s}$ (left), $10.5 \frac{m}{s}$ (middle) and $20 \frac{m}{s}$ (right) | 57 |
| 5.4 | Distribution of power for the ABFM-1W and ABFM-2W, as compared to the BEM model of Appendix B for a sheared inflow at: $5 \frac{m}{s}$ (left), $10.5 \frac{m}{s}$ (middle) and $20 \frac{m}{s}$ (right) | 58 |
| 5.5 | Axial force coefficient of the ABFM-1W and ABFM-2W, as compared to the BEM model of Appendix B for a uniform inflow. The lines indicate the time-averaged value, while the shaded area shows the area of $\mu \pm 2\sigma$. Cases: $5 \frac{m}{s}$ (left), $10.5 \frac{m}{s}$ (middle) and $20 \frac{m}{s}$ (right) | 58 |
| 5.6 | Azimuthal force coefficient of the ABFM-1W and ABFM-2W, as compared to the BEM model of Appendix B for a uniform inflow. The lines indicate the time-averaged value, while the shaded area shows the area of $\mu \pm 2\sigma$. Cases: $5 \frac{m}{s}$ (left), $10.5 \frac{m}{s}$ (middle) and $20 \frac{m}{s}$ (right) | 59 |
| 5.7 | Axial force coefficient of the ABFM-1W and ABFM-2W, as compared to the BEM model of Appendix B for a sheared inflow. The lines indicate the time-averaged value, while the shaded area shows the area of $\mu \pm 2\sigma$. Cases: $5 \frac{m}{s}$ (left), $10.5 \frac{m}{s}$ (middle) and $20 \frac{m}{s}$ (right) | 60 |
| 5.8 | Azimuthal force coefficient of the ABFM-1W and ABFM-2W, as compared to the BEM model of Appendix B for a sheared inflow. The lines indicate the time-averaged value, while the shaded area shows the area of $\mu \pm 2\sigma$. Cases: $5 \frac{m}{s}$ (left), $10.5 \frac{m}{s}$ (middle) and $20 \frac{m}{s}$ (right) | 61 |
| 5.9 | Axial force coefficient of the ABFM-1W and ABFM-2W, as compared to the BEM model of Appendix B for a sheared inflow. The lines indicate the time-averaged value at a constant position of $\theta = \frac{\pi}{2}$, while the shaded area shows the area of $\mu \pm 2\sigma$. Cases: $5 \frac{m}{s}$ (left), $10.5 \frac{m}{s}$ (middle) and $20 \frac{m}{s}$ (right) | 61 |
| 5.10 | Axial force coefficient of the ABFM-1W and ABFM-2W, as compared to the BEM model of Appendix B for a sheared inflow. The lines indicate the time-averaged value at a constant position of $\theta = \frac{3\pi}{2}$, while the shaded area shows the area of $\mu \pm 2\sigma$. Cases: $5 \frac{m}{s}$ (left), $10.5 \frac{m}{s}$ (middle) and $20 \frac{m}{s}$ (right) | 62 |
| 5.11 | Azimuthal force coefficient of the ABFM-1W and ABFM-2W, as compared to the BEM model of Appendix B for a sheared inflow. The lines indicate the time-averaged value at a constant position of $\theta = \frac{\pi}{2}$, while the shaded area shows the area of $\mu \pm 2\sigma$. Cases: $5 \frac{m}{s}$ (left), $10.5 \frac{m}{s}$ (middle) and $20 \frac{m}{s}$ (right) | 62 |
| 5.12 | Azimuthal force coefficient of the ABFM-1W and ABFM-2W, as compared to the BEM model of Appendix B for a sheared inflow. The lines indicate the time-averaged value at a constant position of $\theta = \frac{\pi}{2}$, while the shaded area shows the area of $\mu \pm 2\sigma$. Cases: $5 \frac{m}{s}$ (left), $10.5 \frac{m}{s}$ (middle) and $20 \frac{m}{s}$ (right) | 63 |
| 5.13 | Instantaneous velocity profile downstream of the turbine for a uniform inflow profile of $10.5 \frac{m}{s}$. Left: ABFM-1W, Right: ABFM-2W | 64 |
| 5.14 | Non-dimensional time-averaged axial velocity downstream of the turbine at four distinct planes for a uniform inflow at $10.5 \frac{m}{s}$. The rotor disk is indicated by the dotted line. Top: ABFM-1W, Bottom: ABFM-2W | 64 |
| 5.15 | Time-averaged non-dimensional axial velocity profile along the horizontal direction for $\frac{z}{R} = 0$ at multiple downstream locations | 65 |
| 5.16 | Time-averaged non-dimensional axial velocity profile along the vertical direction at $\frac{y}{R} = 0$ at multiple downstream locations | 65 |
| 5.17 | Time-averaged non-dimensional azimuthal velocity profile at multiple downstream locations for the ABFM-1W and the ABFM-2W. | 66 |
| 5.18 | Time-averaged turbulence intensity along the vertical direction for $\frac{y}{R} = 0$ at multiple downstream locations for the ABFM-1W and the ABFM-2W. | 66 |
| 5.19 | Instantaneous velocity profile downstream of the turbine for a sheared inflow profile of $10.5 \frac{m}{s}$. Left: ABFM-1W, Right: ABFM-2W | 67 |
| 5.20 | Non-dimensional time-averaged axial velocity downstream of the turbine at four distinct planes for a sheared inflow at $10.5 \frac{m}{s}$. The rotor disk is indicated by the dotted line. Top: ABFM-1W, Bottom: ABFM-2W | 67 |
| 5.21 | Time-averaged non-dimensional axial velocity profile along the vertical directions for $\frac{y}{R} = 0$ at multiple downstream locations for the ABFM-1W and the ABFM-2W for a sheared inflow. | 68 |

| | | |
|------|--|----|
| 5.22 | Time-averaged non-dimensional azimuthal velocity profile along the vertical direction for $\frac{y}{R} = 0$ at multiple downstream locations for the ABFM-1W and the ABFM-2W for a sheared inflow. | 68 |
| 5.23 | Time-averaged turbulence intensity along the vertical direction for $\frac{y}{R} = 0$ at multiple downstream locations for the ABFM-1W and the ABFM-2W for a sheared inflow. | 68 |
| 5.24 | Instantaneous velocity profile downstream of the turbine for a uniform inflow profile of $20 \frac{m}{s}$. Left: ABFM-1W, Right: ABFM-2W | 69 |
| 5.25 | Time-averaged non-dimensional axial velocity downstream of the turbine at four distinct planes for a uniform inflow at $20 \frac{m}{s}$. The rotor disk is indicated by the dotted line. Top: ABFM-1W, Bottom: ABFM-2W | 69 |
| 5.26 | Time-averaged non-dimensional axial velocity profile along the vertical direction for $\frac{y}{R} = 0$ at multiple downstream locations for the ABFM-1W and the ABFM-2W for a uniform inflow at $20 \frac{m}{s}$ | 70 |
| 5.27 | Time-averaged non dimensional azimuthal velocity profile along the vertical direction for $\frac{y}{R} = 0$ at multiple downstream locations for the ABFM-1W and the ABFM-2W for a uniform inflow at $20 \frac{m}{s}$ | 70 |
| 5.28 | Time-averaged turbulence intensity along the vertical direction for $\frac{y}{R} = 0$ at multiple downstream locations for the ABFM-1W and the ABFM-2W for a uniform inflow at $20 \frac{m}{s}$ | 71 |
| 5.29 | Distribution of the time-averaged disk velocity for a wind turbine placed 5D downstream of another turbine and offset 0.5D laterally for a uniform inflow of $10.5 \frac{m}{s}$. Left: ABFM-1W, Right: ABFM-2W | 71 |
| 5.30 | Distribution of the time-averaged axial force per unit rotor area for a wind turbine placed 5D downstream of another turbine and offset 0.5D laterally for a uniform inflow of $10.5 \frac{m}{s}$. Left: ABFM-1W, Right: ABFM-2W | 72 |
| 5.31 | Distribution of the time-averaged azimuthal force per unit rotor area for a wind turbine placed 5D downstream of another turbine and offset 0.5D laterally for a uniform inflow of $10.5 \frac{m}{s}$. Left: ABFM-1W, Right: ABFM-2W | 73 |
| 5.32 | Distribution of the temporal standard deviation of the axial disk velocity for a wind turbine placed 5D downstream of another turbine and is offset 0.5D laterally, for a uniform inflow of $10.5 \frac{m}{s}$. Left: ABFM-1W, Right: ABFM-2W | 73 |
| 5.33 | Distribution of the temporal standard deviation of the axial force per unit rotor area for a wind turbine placed 5D downstream of another turbine and is offset 0.5D laterally, for a uniform inflow of $10.5 \frac{m}{s}$. Left: ABFM-1W, Right: ABFM-2W | 74 |
| 5.34 | Distribution of the temporal standard deviation of the azimuthal force per unit rotor area for a wind turbine placed 5D downstream of another turbine and is offset 0.5D laterally, for a uniform inflow of $10.5 \frac{m}{s}$. Left: ABFM-1W, Right: ABFM-2W | 74 |
| A.1 | The $\bar{a} - C_T$ curve for an ideal turbine with no rotational losses in the wake, according to 1D momentum theory and the homogeneous ABFM | 85 |
| A.2 | The $\bar{a} - C_T$ curve of the ABFM based on the parametrised turbine curves of the IEA-15MW Reference turbine, compared to an ideal turbine and the 1D approximation | 85 |
| A.3 | The induction predicted by the ABFM for the IEA-15MW reference turbine, as compared to the upper bound for the induction | 86 |
| A.4 | Correction of the induction of the ABFM using Equation A.7. The upper bound and 1D approximation are given as a reference | 86 |
| B.1 | Reference thrust curve of the IEA-15MW Reference turbine | 90 |
| B.2 | Reference power curve of the IEA-15MW Reference turbine | 90 |
| B.3 | Reference turbine RPM curve of the IEA-15MW Reference turbine | 90 |
| B.4 | Reference blade pitch curve of the IEA-15MW Reference turbine | 90 |

List of Tables

| | | |
|-----|--|----|
| 3.1 | The four different control regions used for turbine curve parametrisation | 31 |
| 3.2 | Simulation settings for the different cases | 40 |
| 4.1 | Operating conditions for the IEA-15MW reference turbine at low, rated and high velocity. The complete turbine curves are provided in Appendix B | 44 |
| 4.2 | Convergence of the degrees of freedom of the discretised ABFM for a uniform inflow at $10.5 \frac{m}{s}$ | 45 |

Nomenclature

Abbreviations

| Abbreviation | Definition |
|--------------|--|
| ABFM | Analytical Body Force Model |
| ABFM-1W | One-way Coupled Analytical Body Force Model |
| ABFM-2W | Two-way Coupled Analytical Body Force Model |
| ABFM-H | Homogeneous Analytical Body Force Model |
| ABL | Atmospheric Boundary Layer |
| AD | Actuator Disk |
| AEP | Annual Energy Production |
| AI | Artificial Intelligence |
| AL | Actuator Line |
| AS | Actuator Sector |
| ASF | Actuator Surface |
| ASPIRE | Atmospheric Simulation Platform for Innovation, Research and Education |
| BE | Blade-Element |
| BEM | Blade-Element-Momentum (theory) |
| CBS | Centraal Bureau voor Statistiek |
| CFD | Computation Fluid Dynamics |
| CFL | Courant-Friedrichs-Lewy |
| CPU | Central Processing Unit |
| DALES | Dutch Atmospheric Large-Eddy Simulation |
| DDES | Delayed Detached-Eddy Simulation |
| DES | Detached-Eddy Simulation |
| DNS | Direct Numerical Simulation |
| DTU | Danmarkse Tekniske Universitet |
| EAL | Elastic Actuator Line |
| ECMWF | European Centre for Medium-Range Weather Forecasts |
| ERA5 | ECMWF Reanalysis 5th Generation |
| GPU | Graphical Processing Unit |
| IEA | International Energy Agency |
| IRENA | International Renewable Energy Agency |
| ISA | International Standard Atmosphere |
| KNMI | Koninklijk Nederlands Meteorologisch Instituut |
| LES | Large-Eddy-Simulations |
| NREL | National Renewable Energy Laboratory |
| NWP | Numerical Weather Prediction |
| RANS | Reynolds Averaged Navier-Stokes |
| RPM | Rotations per Minute |
| TSR | Tip-speed ratio |
| URANS | Unsteady Reynolds Averaged Navier-Stokes |
| VLM | Vortex Lattice Method |

Symbols

| Symbol | Definition | Unit |
|---------------------------|---|----------------------|
| \bar{a} | Average axial induction factor | [-] |
| $\langle Q \rangle_\tau$ | Time average of quantity Q over time scale τ | [-] |
| A | Area | [m ²] |
| a_c | First empirical coefficient of the root correction | [-] |
| b_c | Second empirical coefficient of the root correction | [-] |
| C_{ax} | Axial force coefficient | [-] |
| C_{az} | Azimuthal force coefficient | [-] |
| C_P | Power coefficient | [-] |
| C_{P_r} | Rated power coefficient | [-] |
| C_T | Thrust coefficient | [-] |
| C_{T_r} | Rated thrust coefficient | [-] |
| d | Distance | [m] |
| D | Rotor diameter | [m] |
| f_{ax} | Axial force per unit rotor area | [$\frac{N}{m^2}$] |
| f_{az}/f_θ | Azimuthal force per unit rotor area | [$\frac{N}{m^2}$] |
| F | Tip correction function | [-] |
| g | Root correction function | [-] |
| \dot{m} | Mass flow | [$\frac{kg}{s}$] |
| N_b | Number of blades | [-] |
| P | Power | [W] |
| P_G | Generator power | [W] |
| P_r | Rated power | W |
| q_0 | Non-dimensionalised rotor circulation | [-] |
| Q_d | A quantity at the disk | [-] |
| $\overline{Q_d}$ | Disk average of quantity Q_d | [-] |
| R | Rotor radius | [m] |
| S_0 | Solid-body wake rotation term | [-] |
| T | Thrust | [N] |
| u_d | Distribution of axial velocity at the rotor disk | [$\frac{m}{s}$] |
| $u_{d_{ABFM}}$ | Distribution of axial disk velocity as predicted by the ABFM | [$\frac{m}{s}$] |
| $\overline{u_{d_{ABFM}}}$ | Disk averaged axial velocity at the rotor disk as predicted by the ABFM | [$\frac{m}{s}$] |
| u_θ | Distribution of azimuthal velocity | [$\frac{m}{s}$] |
| U_0 | Freestream velocity | [$\frac{m}{s}$] |
| U_{in} | Cut-in velocity | [$\frac{m}{s}$] |
| U_{out} | Cut-out velocity | [$\frac{m}{s}$] |
| U_r | Rated velocity | [$\frac{m}{s}$] |
| U_{ref} | Reference velocity | [$\frac{m}{s}$] |
| V_{rel} | Relative local velocity | [$\frac{m}{s}$] |
| α_s | Freestream shear coefficient | [-] |
| α_w | Exponential rolling average weight | [-] |
| γ | Turbine yaw angle | [°] |
| $\bar{\delta}$ | Viscous core size | [m] |
| ϵ | Smearing length | [m] |
| η | Force projection kernel | [-] |
| λ | Tip-speed ratio | [-] |
| λ_r | Rated tip-speed ratio | [-] |
| μ | Statistical mean | [-] |
| ρ | Air density | [$\frac{kg}{m^3}$] |
| ρ_{ref} | Reference density | [$\frac{kg}{m^3}$] |
| σ | Statistical standard deviation | [-] |

| Symbol | Definition | Unit |
|----------|--------------------------|-------|
| τ | Time scale | [s] |
| Ω | Turbine rotational speed | [RPM] |

Coordinate directions, angles, indices and discretisations

| Symbol | Definition | Unit |
|----------------|--|------|
| \hat{e} | Unit vector along the direction of the subscript | [-] |
| i | Index along the radial direction | [-] |
| j | Index along the azimuthal direction | [-] |
| l | Index along the x_{LES} -direction | [-] |
| m | Index along the y_{LES} -direction | [-] |
| n | Index along the z_{LES} -direction | [-] |
| N | Number of points along direction of the subscript | [-] |
| r | Radial position | [m] |
| x | Non-dimensional radial coordinate | [-] |
| x' | Horizontal direction of the turbine, offset with an angle χ with respect to x_{LES} | [m] |
| x_{ax} | Turbine axial direction | [m] |
| x_{LES} | x-direction of the LES | [m] |
| y_{LES} | y-direction of the LES | [m] |
| y_{turb} | Aligned with the $\theta = 0$ direction of the rotor disk | [m] |
| z_{LES} | z-direction of the LES | [m] |
| z_{turb} | z-direction of the turbine, rotated with an angle of α with respect to the vertical | [m] |
| α | Rotor tilt angle | [°] |
| Δ_{LES} | Grid size of the LES | [m] |
| θ | Azimuthal position on the rotor disk | [°] |
| χ | Yaw angle of the turbine with respect to LES grid | [°] |

1

Introduction

In an effort to reduce carbon dioxide emissions, the world is slowly replacing fossil fuel-based electricity generation with its renewable counterparts. As such, the capacity for both onshore and offshore wind power is also rapidly rising. According to the Center for Statistiek Statistics (CBS), the wind energy capacity in the Netherlands increased by more than 280% in the period 2015-2023[11]. In 2023 alone, this growth was an impressive 35%, adding up to a total of 29TWh being generated by wind resources. Compared to the total electricity production of 120TWh, it can be concluded that almost 25% of Dutch electricity in 2023 was generated by wind power.

On a global scale, this development is moving slightly slower, yet the share of wind energy contributed a not insignificant 7.8% to the total electricity production in 2023, as opposed to a mere 3.5% in 2015[19]. Coupled with this increased interest in wind energy, the industry has benefited significantly from economy of scales, dropping its costs per kWh to below those of fossil fuels and to levels similar to those of other renewables, as seen in Figure 1.1[30].

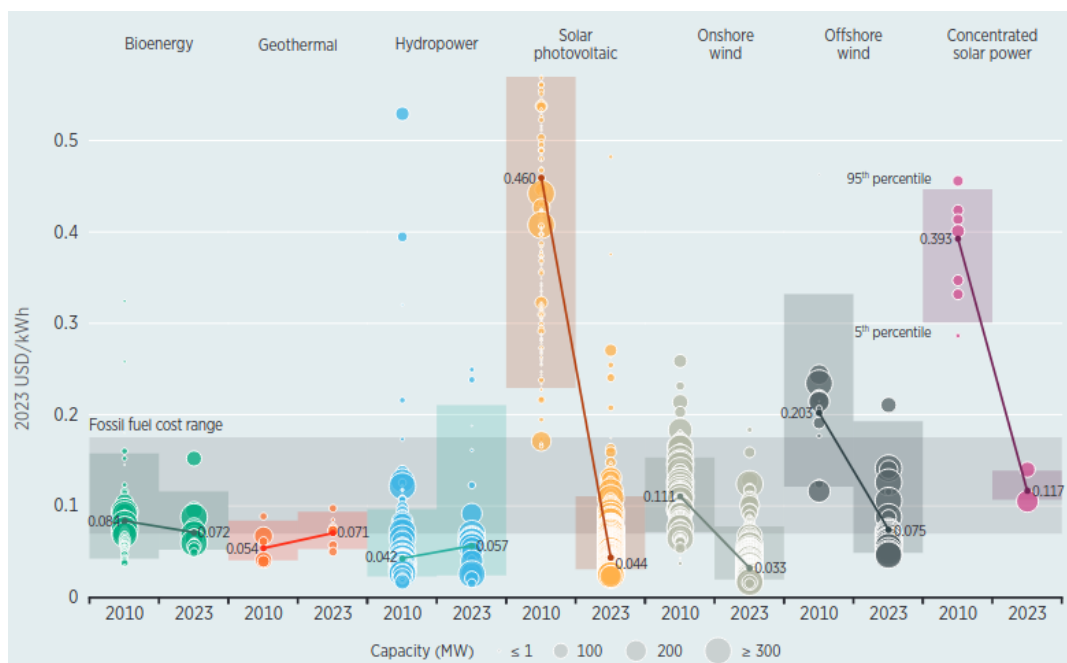


Figure 1.1: Costs per kWh of different renewables, compared to fossil fuels. Graphic obtained from IRENA[30]

This growth is also partially stimulated by significant advances in turbine design, allowing installment of turbines of ever-increasing size and capacity, as demonstrated in Figure 1.2[89]. The first installment

of the largest turbine to date, the MySE18.X-20MW by Mingyang Smart Energy, was just finished in China in August 2024[21]. With a rotor diameter of 260-292m and a sweeping area of almost 67 000m², the turbine has a revolutionary rated power of 20MW.

In addition to isolated turbine performance, advances in the fields of Computational Fluid Dynamics (CFD) allow for a more elaborate investigation of the airflow interaction between wind turbines and their environment. Current state of the art Large-Eddy Simulations (LES) have advanced the understanding of intricate flow behaviour regarding wake interference between turbines in a farm, as well as the effects of complex terrain. This in turn has inspired many different new research branches centered around wind farm dynamics and wind resource assessment. Unfortunately, LES' high computational costs have limited these studies to mostly simplified academic cases, which are not directly applicable in industry[3].

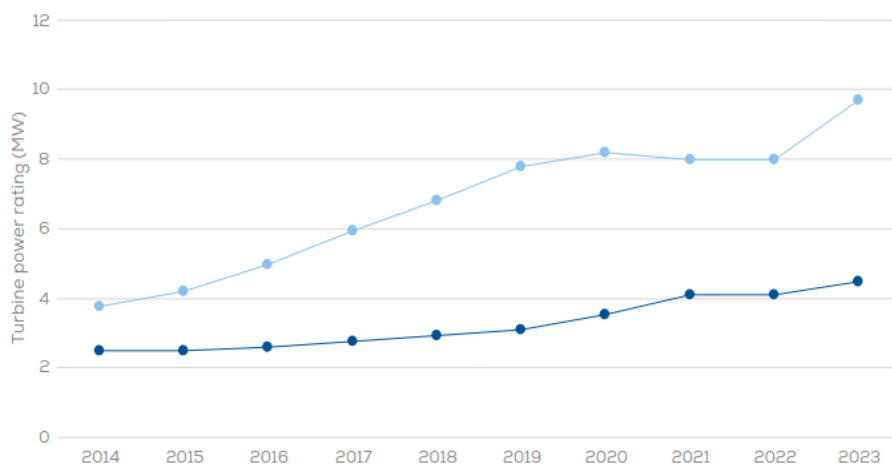


Figure 1.2: Average capacity of on-shore and off-shore wind turbines in the period 2014-2023. Graphic obtained from Wind Europe[89]

However, the potential for computational complexity is ever increasing. For decades, processor architecture has adhered to Moore's law, leading to a doubling of transistors in densely integrated circuits roughly every two years[12]. In more recent years, this growth seems to slow as physical limits are approached. Instead, a greater emphasis is placed on the parallelization of tasks on GPUs, which is further accelerated by the increasing interest in AI applications, which benefit greatly from this archetype[40].

All these increases in computational speed, combined with the adaptations of CFD codes for use on the GPU have allowed significant speedups of LES simulations[60]. As a result, these developments are gradually being introduced in industry by some companies. One such company is Whiffle, the company with which this thesis is carried out in collaboration. Whiffle has developed a GPU-based atmospheric flow LES solver called ASPIRE[28]. Using ASPIRE, they aim to enable the simulation of complete wind farms. This in turn enables more realistic wind resource assessment and power forecasting.

In this thesis, it will be investigated how current industry LES methods can be improved to calculate the blade loads of wind turbines. This will be done by extending the integrated wind turbine framework in ASPIRE. Specifically, the research aims to develop an efficient approach to model the force distribution along wind turbine blades without extensive geometric details, which are often confidential. The chosen approach should be viable for application on an industry scale.

The thesis is structured as follows. First, chapter 2 will present an overview of relevant literature. Then, the methodology and modeling techniques will be discussed in chapter 3. As some of these models are relatively new, they will be extensively verified in chapter 4. Afterwards, chapter 5 will discuss the results in a more realistic setup. The thesis will end with a conclusion in chapter 6 and recommendations for future work in chapter 7.

2

Literature Review

Wind turbine dynamics have been studied for over a hundred years. Many different approaches have been tried, with varying degrees of success. To implement a new modeling technique, it is essential to know what has been done before and build on existing ideas. To do this effectively, it is required to study the current literature.

In this chapter, it will be reviewed how the aerodynamics of wind turbines have been modeled in the past and in the current times. First, section 2.1 will discuss how the performance of a single turbine is assessed. Then section 2.2 will extend this framework to the assessment of entire wind farms. Afterwards, section 2.3 will analyse how these techniques are combined in state-of-the-art research, but also what limitations are encountered. Based on these limitations it will be seen that there are several possibilities to apply new LES techniques to industry. This will be further explored in section 2.4, which discusses the research questions and hypothesis for this work.

2.1. Individual Turbine Analysis

During rotor design, one has to consider many different load cases. Meanwhile, the rotor geometry can be optimized using a large set of design variables, which all have to be investigated. As such, the emphasis during this phase is placed on investigating many different scenarios. Simulation tools should therefore be predominantly fast, while maintaining a reasonable level of accuracy. This generally requires the use of some assumptions, making these models most suitable for isolated turbine analysis of relatively simple flow cases. Throughout the years many different techniques have been developed. The simplest and arguably the most important one is the Blade Element Momentum (BEM) theory, which is explained in subsection 2.1.1. The next level of complexity consists of vortex models, which are briefly covered in subsection 2.1.2. Then, subsection 2.1.3 will cover blade-resolved computational fluid dynamics simulations, which constitute a much more state-of-the-art numerical technique. The section will end with a discussion on Actuator Methods in subsection 2.1.4, which are used to represent turbines within a CFD simulation in a simplified manner.

2.1.1. Blade Element Momentum Theory

BEM theory was developed by Glauert already in 1935[22]. Although the theory was originally intended for propeller design, it is applicable to turbines as well. Despite its simplicity, BEM has proven to be accurate for a wide variety of commonly occurring use cases, causing it to still be a common tool in turbine analysis. Sørensen [73] even claims that it is the only approach used by turbine manufacturers in rotor design. Moriarty and Hansen[46] indeed confirm that this exact formulation forms the backbone of the "AeroDyn" module of FAST, a software package often used in academia for the evaluation of rotor performance.

As the name suggests, BEM theory forms a combination between blade-element and momentum theory. The former refers to a technique in which the aerodynamic characteristics of a 3-dimensional turbine blade are determined by investigating the 2-dimensional airfoil geometry, considering the local value

of perceived velocity. According to this definition, the radial thrust and torque distribution is given by Equation 2.1 and Equation 2.2 respectively[73]. Here T refers to the thrust force, N_b to the number of blades, F_n to the normal force of a single blade per unit of span, ρ to the air density, V_{rel} to the local velocity, C_n to the non-dimensional normal coefficient of the airfoil, Q to the torque, F_t to the tangential force per blade per unit span, r to the radial coordinate and C_t to the tangential force coefficient.

$$\frac{dT}{dr} = N_b F_n = \frac{1}{2} \rho c N_b V_{rel}^2 C_n \quad (2.1) \quad \frac{dQ}{dr} = N_b F_t r = \frac{1}{2} \rho c N_b r V_{rel}^2 C_t \quad (2.2)$$

The force coefficients are given by a rotation over the local inflow angle ϕ of the aerodynamic coefficients of lift and drag to the turbine coordinate system. Following Figure 2.1, it is found that the normal and tangential coefficients are found from the lift and drag coefficients as in Equation 2.3 and Equation 2.4. These aerodynamic coefficients, in turn, can be found from tabulated airfoil data at the relevant Reynolds number. Note that these 2D airfoil data are generally obtained from experiments and need to be corrected for 3D effects. The angle of attack is found from Equation 2.5, where γ includes the effect of both the twist of the blade and the pitch.

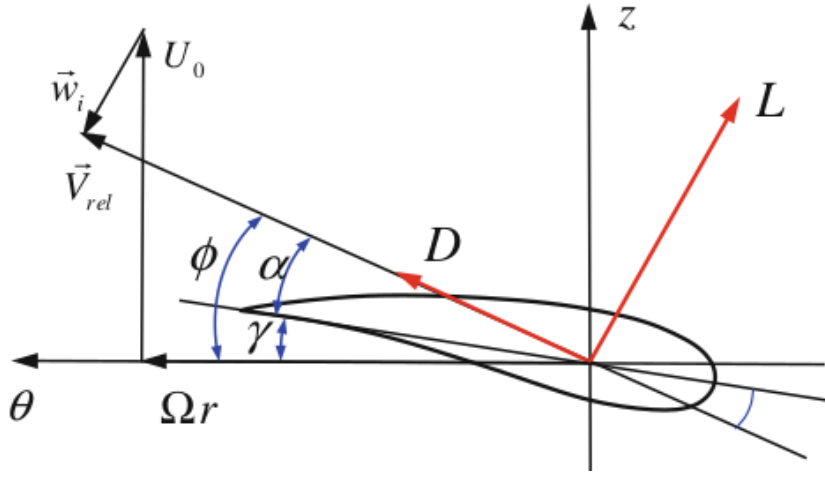


Figure 2.1: A Blade Element with its corresponding force and angle definitions. Graphic obtained from [73]

$$C_n = C_l(\alpha) \cos \phi + C_d(\alpha) \sin \phi \quad (2.3) \quad C_t = C_l(\alpha) \sin \phi - C_d(\alpha) \cos \phi \quad (2.4) \quad \phi = \alpha + \gamma \quad (2.5)$$

If the local conditions are known, the forces can be calculated. Generally, these conditions will be described as a function of the axial induction factor a and the azimuthal induction factor a' , as in Equation 2.6 and Equation 2.7. The relation between the induction factor and the loading is in turn determined from momentum theory, as in Equation 2.8 and Equation 2.9, where $F(r)$ is the tip correction factor.

$$\tan \phi = \frac{U_0(1-a)}{\Omega r(1+a')} \quad (2.6) \quad V_{rel} = \sqrt{(U_0(1-a))^2 + (\Omega r(1+a'))^2} \quad (2.7)$$

$$\frac{dT}{dr} = F(r) 4\pi \rho r U_0^2 a(1-a) \quad (2.8) \quad \frac{dQ}{dr} = F(r) 4\pi r^3 \Omega U_0 a'(1-a) \quad (2.9)$$

If the correction factor $F(r)$ is known, Equation 2.1-2.9 form a complete, but implicit, nonlinear system. Because of that, an iterative approach is generally used to determine its solution. An initial guess for a and a' is chosen and used to calculate the loading using Equation 2.1 and Equation 2.2. These results are then fed back into Equation 2.8 and Equation 2.9, and this cycle repeats until convergence.

It is mentioned by Sørensen [73], Burton et. al[10] and Wilson and Lissaman[88] that when using the loading to update Equation 2.8 and Equation 2.9, it could be justified to only include the load generated by the airfoil lift, as the drag forces have a viscous origin and its induction is therefore only of importance within the narrow boundary layer. However, there does not seem to be a clear consensus on this topic and as such some BEM solvers, such as FAST, provide both options[46].

For the tip correction factor $F(r)$, there are many formulations. The original was developed by Prandtl as an extension of the work of Betz[5]. In this work, Prandtl defined an approximate solution for the distribution of circulation along an ideal rotor, corresponding to a helical vortex sheet that moves at a constant induced velocity in the axial direction with a constant helical pitch. By approximating this as an infinite set of planar wings, a correction of the form of Equation 2.10 was defined. Here, λ is the tip speed ratio, r the radial coordinate, and R the radius of the rotor disc.

By considering the effect of local inflow from the perspective of induced velocities, Glauert later proposed his famous correction, as defined in Equation 2.11[22]. Although different formulations exist, Glauert's correction is the most commonly used[73].

$$F(r) = \frac{2}{\pi} \arccos \left[\exp \left(-\frac{N_b}{2} \sqrt{1 + \lambda^2 \left(1 - \frac{r}{R}\right)} \right) \right] \quad F(r) = \frac{2}{\pi} \arccos \left[\exp \left(-\frac{N_b \left(1 - \frac{r}{R}\right)}{2 \frac{r}{R} \sin \phi} \right) \right] \quad (2.11)$$

In the case of a heavily loaded rotor, corresponding to $a \geq 0.5$, momentum theory predicts a flow reversal in the wake. In reality however, a turbulent wake state occurs, where flow from outside the streamtube is entrained into the wake. Based on helicopter measurements, Glauert suggested using $C_T = C_{T1} - 4(\sqrt{C_{T1}} - 1(1 - a))$, with $C_{T1} = 1.816$ for $a \geq 0.5$ [10], instead of the usual $C_T = 4a(1 - a)$ that would follow from momentum theory. Wilson and Lissaman[88] instead propose to use $C_{T1} = 1.6$.

For many simple cases, BEM is applicable using the format described above. For more complicated flow systems, additional models are often provided. Due to their complexity and quantity, these will not be described in detail, but the most important ones will shortly be mentioned. Dynamic, often semi-empiric, stall models are used to take into account the effect of angle of attack history, circumventing the quasi-steady assumption of BEM. A common choice is the model of Leishman and Beddoes[34], but many alternatives exist. In case a more general description of dynamic inflow or wake is required, large parts of BEM theory have to be supplemented by methods like the "acceleration potential method" by Peters and He[52].

The effects of yaw on a turbine, although common, can be hard to describe. This is because a strong unsteady effect is combined with a potentially large span-wise flow component, breaking the assumption of locally 2D flow[46]. In yaw, the wake axis is not aligned with the free-stream direction, leading to a skew angle ξ [73]. Most wake models rely on defining a correction on the induced velocity as a function of this skew angle and azimuthal position, such as the model of Glauert[22] or Snel[69].

2.1.2. Vortex Models

BEM has proven to be a very useful method for predicting rotor performance. Still, the method heavily relies on assumptions, experimental data, and correction models. Because of that, it is often desired to make use of models that more explicitly capture the physics of the problem.

Vorticity based models make use of the potential flow equations to approximate the flow physics of lifting bodies. The first vorticity-based model for 3d geometries was the Lifting Line Theory of Prandtl[55], developed for the calculation of aircraft performance. The method is covered in many books such as the work of Anderson[2]. The basis of the method is to replace the presence of the wing by a "lifting line", represented by a bound vortex filament with a trailing vorticity sheet, see Figure 2.2[2]. In the discrete case, the lifting line is made up from a collection of horseshoe vortices.

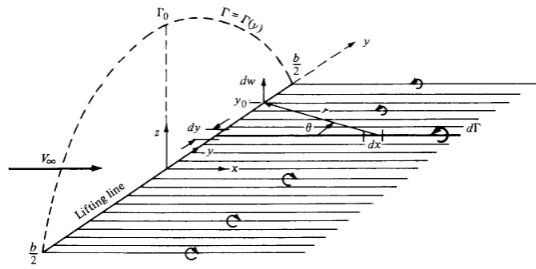


Figure 2.2: Lifting Line representation of a wing. Figure obtained from Anderson[2]

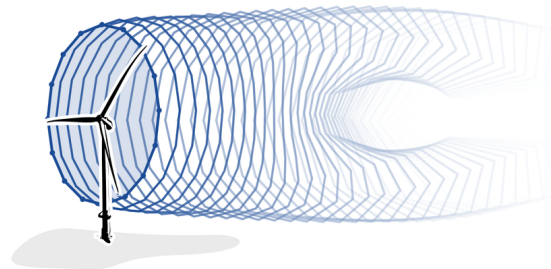


Figure 2.3: Free wake representation of vortex filaments. Figure obtained from Van den Broek et al.[8]

The Lifting Line theories have later been extended to slightly more elaborate methods, like the Vortex Lattice Method (VLM) and general panel methods. Where the Lifting line method only takes into account a span-wise variation of circulation, these methods account for stream-wise changes as well. Panel methods also take into account the effect of thickness and non-lifting geometries, albeit at a significantly higher cost than the VLM. Therefore, VLM is often used in practice.

Since a turbine is essentially a rotating wing, the vortex methods can also be applied to wind turbines. A good review is given by Huang et al.[26]. When applying a vortex model to a turbine, one has to account for the structure of the wake, as the blade rotation will cause a helical wake structure. The simplest approach is to use a frozen wake model, sometimes called a prescribed wake. Here, a wake shape is assumed for all trailing vortex filaments, which can significantly simplify the analysis. In a more realistic model, all vortex filaments will be convected along the flow at the local flow velocity. Every vortex filament therefore influences the position of every other filament, requiring a time-resolved evaluation of the flow field. This approach is shown in Figure 2.3. However, evaluating the convection of the vortex filaments can be computationally intensive. Instead, the wake is sometimes described by convecting point vortices. This particle wake model is an excellent trade-off between cost and accuracy.

Since vortex models are built from potential theory, they can be extended to use for even more situations. The transient behaviour can easily be represented by shedding vorticity from the bound vortex, every time the turbine loading changes. Additionally, since the model is linear, multiple turbines and their interaction can easily be included by adding more lifting lines and trailing vortices to the model. Note that in the case of wake interaction this will require a free wake model.

Especially for lifting line theory, some simple cases can even be solved analytically. These solutions can then be used for the validation and calibration of other calculations. In fact, many BEM corrections originate from vortex models, such as the tip correction and several wake models[73].

Still, the methods are not perfect. Being based on potential flow theory, the method is entirely based on incompressible, inviscid, irrotational flow. Especially the inviscid assumption can be limiting, since many practical cases rely on viscous phenomena. A few examples are the stall of the blades at a high angle of attack or the turbulent breakdown of the far wake. As such, the vortex model performs best under design conditions, when flow separation is not present. Its representation of the near-wake structures is excellent, but ultimately for correct far-wake representations, viscosity has to be considered.

2.1.3. Blade Resolved CFD

While BEM has proven to be an effective approach to analyze rotors under simple conditions, in reality wind turbines operate in a very challenging and unsteady environment. Combined with the fact that new rotor models have larger blades, aero-elastic effects are becoming more important. This breaks the assumption of BEM, which considers the momentum sink of the blades to be within the rotor disc plane[46]. As such, more advanced analysis techniques are required.

Numerical solutions to the Navier-Stokes equations allow for a very detailed analysis of complex flow in the presence of a turbine. Since these equations govern fluid flow itself, far fewer assumptions have to be made, leading to an increased fidelity in the model. To account for the presence of the turbine, the geometry should be a part of the mesh, as demonstrated in Figure 2.4[68]. Alternatively, the rotor presence can be modeled, which will be discussed in subsection 2.1.4.

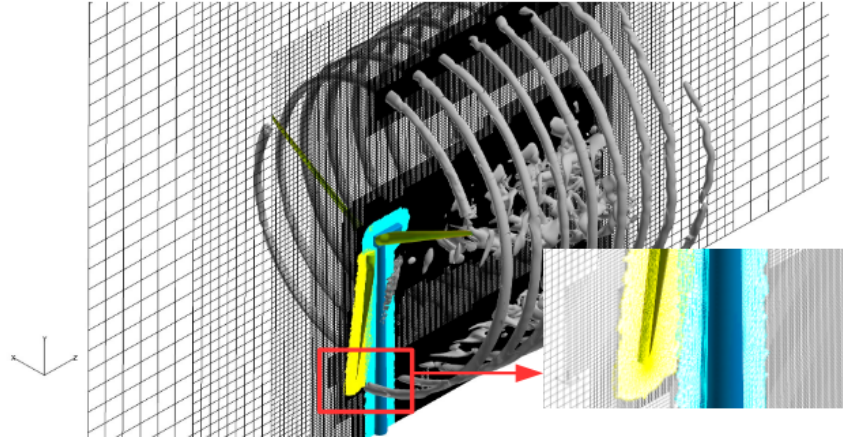


Figure 2.4: Incorporating the rotor geometry into the mesh. Figure obtained from Sitaraman[68]

The first CFD computation on wind turbine rotors was conducted by Sørensen and Hansen in 1998. Since computational power was much lower back then, this simulation was not feasible to integrate into general design cycles. They mention: "Instead, they can be used to obtain sufficient knowledge, allowing the engineers to synthesize the necessary airfoil data for the BEM method"[75]. Today, CFD is slowly finding its way into the design process, such as the work of Congedo and De Giorgi[14], who did a small optimization of winglets for wind turbine design. Madsen et al.[35] then took this idea and extended it by coupling their solver to a gradient-based shape optimizer, leading to an automatic optimization process.

For simulation of the Navier-Stokes equations, an incompressible approach is generally justified. Considering that Class 1 turbines experience an average wind speed of only $10 \frac{m}{s}$ [96], with design tip speed ratios of approximately 8[4], the maximal Mach number is approximately 0.23, while below 0.3 the incompressible assumption is typically justified. Although it is a common approach, Yan and Archer[93] addressed that already under rated conditions, the effects of compressibility can cause a reduction in power of up to 8%. More research on this topic is expected in the following years, but for now wind turbine analysis is generally done using the incompressible flow equations.

Using the assumption of incompressible flow, the velocity and pressure field are governed by Equation 2.12 and Equation 2.13[51]. Here \mathbf{U} is the velocity field, p the pressure field, ν the kinematic viscosity, and \mathbf{f} some general body force. However, special attention has to be paid to the treatment of turbulent properties. Many books have been written on this topic, such as the work of Wilcox[87], but it is still an active topic of research today. If Equation 2.12 and Equation 2.13 were to be solved as is, this technique would be called Direct Numerical Simulation (DNS). In a DNS, all turbulent influences must be resolved explicitly, meaning that the grid and time step should be fine enough to capture the Kolmogorov scale, with a domain large enough to resolve the integral scale[87]. This is generally not feasible for wind turbine analysis[51].

$$\nabla \cdot \mathbf{U} = 0 \quad (2.12) \quad \frac{\partial \mathbf{U}}{\partial t} + \nabla \cdot (\mathbf{U}\mathbf{U}) = -\nabla p + \nabla \cdot (\nu \nabla \mathbf{U}) + \mathbf{f} \quad (2.13)$$

Instead, some type of turbulence treatment is necessary. Within engineering, the most common approach is Reynolds Averaged Navier-Stokes (RANS), as it captures the relevant turbulent flow phenomena for most cases of engineering interest, while introducing minimal complexity and cost[87]. Within RANS, one solves for the mean component of the flow field. In many cases the statistical mean flow is steady, so that the time derivative can be neglected. However, in some cases, the mean flow can show significant deviations over time and must be resolved. This subset of RANS simulation is often called Unsteady Reynolds Averaged Navier Stokes (URANS).

Due to the non-linearity of the momentum equation, an additional term involving velocity fluctuations will occur in the averaged momentum equation. Solving for this term, commonly called the Reynolds stress tensor, introduces new unknowns, which results in the well-known turbulence closure problem. Many different turbulence models exist, making estimations and assumptions to complete the closure. There

is no clear best turbulence model for a general case. Instead, several models provide advantages and disadvantages, dependent on the flow physics considered. For a more extensive overview of the different types of turbulence models, applications, and validity, the reader is referred to the work of Wilcox[87].

As an alternative to RANS, where all turbulence is modeled, and DNS, where all turbulence is resolved, Large-Eddy Simulations (LES) provides a solution that is in between both RANS and DNS in terms of both accuracy and cost. Many references cover the details of LES, such as the book by Sagaut[58]. In LES, a filter operation is applied to Equation 2.12 and Equation 2.13 and the equations are solved for the filtered quantity. All turbulent scales above the filter width are explicitly resolved, whereas all smaller scales have to be modeled. This effect of the modeled scales is seen in the momentum equation as a sub-grid stress tensor which, just as for RANS, appears due to the non-linearity in the convective term when applying the filter operation.

Although LES can be much more accurate than RANS, it still proves to be rather computationally expensive, especially when boundary layer flow is concerned. As such a variety of hybrid LES-RANS methods have been developed, as Mocket[43] describes in his thesis. The most common approaches are Detached-Eddy Simulation (DES) and its subcategory Delayed Detached-Eddy Simulation (DDES). The idea of DES is to simulate only the largest, energetic turbulent scales using LES, while using the much cheaper RANS for the remaining part of the spectrum. As such, DES is a promising way to reduce LES costs while maintaining most of its accuracy.

Many of these CFD techniques have been applied to wind turbines. Rocha et al.[57] and de Oliveira et al.[51] both investigated turbine effects using URANS and found satisfactory results. Rocha, however, did mention that experimental data were required to calibrate the turbulence model but is unknown to what extent this calibration is different between models. Additionally, both mention that cases with high chance of stall are avoided. Zhang et al.[98, 97] on the other hand performed comparisons between URANS and DDES in low TSR and parked operation. Both of these conditions are expected to show large regions of separated flow and in both scenarios it was found that the DDES model was able to resolve this separated region significantly better.

2.1.4. CFD with Actuator Models

For many investigations, the details of the boundary layer of the turbine blade are of no further interest, but instead the general characteristics of the wake should be captured. As such, large computational expenses can be saved if not the complete blades have to be resolved by the CFD, but instead their influence is captured in a more simplistic way. Since the main goal of a wind turbine is to extract energy from the flow, its influence can be directly modeled by using body forces that act as momentum sinks in the Navier-Stokes equations. This approach can be used in RANS, LES and other turbulence modeling techniques and is generally referred to as "actuator methods". Several implementations exist, a concise overview is provided in the work of Sanderse et al.[59]. The most important models will be briefly discussed.

2.1.4.1. Types of Actuator Models

Actuator Disk The Actuator Disk (AD) method is a simple method that is used to define a loading to be projected onto the domain as body forces. The disk itself is seen as a permeable surface that acts as a momentum sink. In the simplest form of the model, only uniform thrust forcing is considered, which follows from Equation 2.14[91]. In this equation T is the thrust, C_T the thrust coefficient, ρ the air density, V the free-stream velocity, and A_r the disk area. For a given wind turbine, the thrust coefficient is known for a given free-stream velocity from the thrust curve of the turbine.

$$T = C_T \frac{1}{2} \rho V^2 A_r \quad (2.14)$$

Considering the case of a single turbine, the free-stream velocity is generally clearly defined. In this case Equation 2.14 is used to calculate the total rotor force at a given instant of the LES, which can be evenly spread over the rotor area. This force then has to be coupled back into the simulation, for which it has to be projected onto the LES grid as a body force. Since the disk is infinitely thin, directly applying the force to the grid can lead to numerical instabilities. Instead, a convolution with a 3D Gaussian kernel

can be used to smear the loading on the grid[70, 42], using Equation 2.15 and Equation 2.16. Here, \mathbf{f} is the body force, \mathbf{F} the actuator force, ΔV the volume of a cell, ϵ the smearing width and d the distance between the applied force and the smeared projection.

$$\mathbf{f} = \frac{1}{\Delta V}(\mathbf{F} \otimes \eta) \quad (2.15) \quad \eta = \frac{1}{\epsilon^3 \pi^{\frac{3}{2}}} e^{-\frac{d^2}{\epsilon^2}} \quad (2.16)$$

Special attention should be paid to this smearing width. Mikkelsen recommends a value in the order of 1-4 axial cell lengths[42]. Meanwhile, Sørensen and Shen[70] state that the force should be smeared across at least 2 cells. This requirement makes sense, as it essentially gives the actuator disk a finite thickness, removing any singularities from the system. A larger smearing width, will lead to a smoother force distribution and hence give more numerical stability. On the other hand, it should be desired to keep ϵ as low as possible, since the physical forcing applied by the turbine takes place over a small axial distance, roughly corresponding to the chord length of the blades. Choosing ϵ such that the force is smeared on 2 cells therefore seems to make the most physical sense.

At the same time, one could wonder about the validity of using a 3-dimensional Gaussian in the first place. After all, the instability is linked to the infinitesimal thickness of the disk, which is only present in a single direction. By smearing the forces in all three directions, part of the load on the outer edges of the actuator disk is smeared outside the radius of the disk itself. Since the convolution conserves the total force, the projected force distribution will no longer be uniform. The simulated result will therefore no longer correctly represent the intended actuator disk formulation. In fact, Mikkelsen[42] realizes this limitation and instead suggests an alternative smearing approach, using a 1d Gaussian kernel in the axial direction. In some of his newer work, Sørensen [72] also adopts this strategy. The body forces in this case are given by Equation 2.17 and Equation 2.18.

$$\mathbf{f} = \frac{1}{\Delta V}(\mathbf{F} \otimes \eta_{1d}) \quad (2.17) \quad \eta_{1d} = \frac{1}{\epsilon \sqrt{\pi}} e^{-\frac{d^2}{\epsilon^2}} \quad (2.18)$$

The method described above only introduces an axial force that is uniformly spread over the entire disk. This completely neglects the tangential forces, which cause a rotation of the wake. Including these tangential forces therefore better describe the mixing processes in the wake, leading to better wake characteristics[91, 54]. Additionally, the real turbine forces are not evenly distributed in the disk area. Here, especially the radial distribution should be of importance, since the azimuthal distribution would be constant with respect to the average of a revolution under steady conditions with homogeneous inflow. Still, for highly heterogeneous inflow, the azimuthal dependence could be significant.

Some efforts have been made to refine the actuator disk loading distribution model. If the simulated conditions are constant and predictable, a pre-defined loading distribution can be specified. This method was used in the work of Van der Laan et al.[31]. Alternatively, the distribution can be calculated on the fly by coupling the LES to some Blade Element (BE) computation. This method is very similar to BEM, where the loading is calculated from Equation 2.1-2.5. In a typical BEM approach, momentum theory would then be used to find the local velocity and inflow conditions of the induction factors. In this coupled approach, however, this information can directly be obtained by sampling the velocity field from the LES. This is done by discretising the actuator disk onto a polar mesh and then calculating the load on each of those cells.

This approach takes into account both the tangential load and the radial load distribution and is often used in literature[54, 91, 75]. If the inflow field is heterogeneous, azimuthal differences in load can even be included to some extent. However, a major disadvantage is that the BE computation requires many geometric details, such as airfoil geometry and twist distributions. This information may not always be available, especially in an industry setting. To couple the forces with the LES, they should be projected onto the grid, which can again be done by either Equation 2.15-2.16 or Equation 2.17-2.18.

Actuator Line The AD method has been proven in the literature to be a very effective method for efficient simulation of wind turbines. However, due to the azimuthal spreading of force, the model fails to resolve tip vortices[99]. These tip vortices characterize near-wake behaviour and are therefore essential for correctly modeling the flow just behind the turbine.

As a solution Sørensen and Shen[76] created the Actuator Line (AL) model. This model again uses

a BE approach to calculate the rotor loading. First, all turbine blades are discretized into a set of segments. For each segment, the velocity is sampled along the quarter-chord line, which represents the aerodynamic center for a basic airfoil[2], by interpolating between the grid points of the LES. Using the local blade geometry and the sampled velocity, the loading of the blade segment can then be evaluated using BE theory. The actuator line locations are updated each time step, so that loading can be resolved at the exact blade locations. The resulting velocity and vorticity distributions for a given time instant are shown in Figure 2.5[99], where the effect of the tip and root vortex can be clearly distinguished. Also note that the tip vortex forms a spiral, whereas this would be a continuous sheet for an AD.

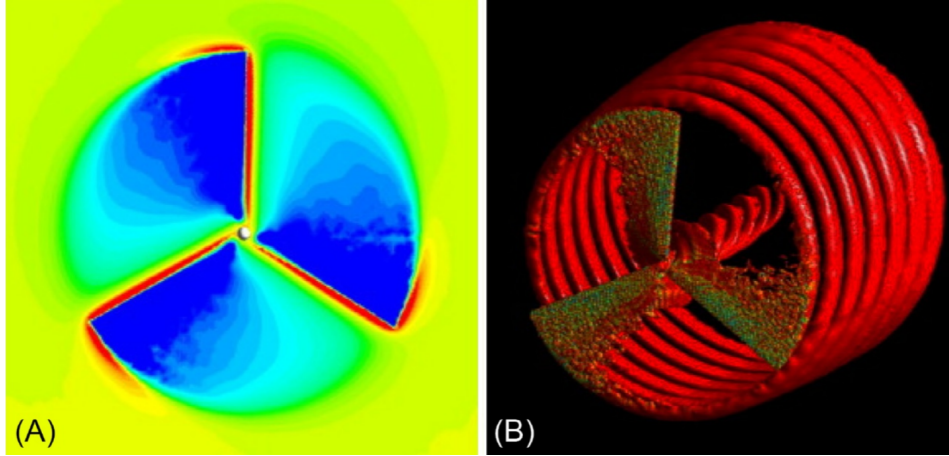


Figure 2.5: The distribution of axial velocity in the rotor disc (A) and iso surfaces of vorticity of the tip and root vortex (B) for an AL method. Figure obtained from Zhao et al.[99]

To couple the forces back to the LES, they are smeared along the lines using a kernel. In the simplest approach, the same 3D Gaussian kernel approach from the AD method was used, as shown in Equation 2.15 and Equation 2.16. Since the AL method specifically aims to resolve the tip vortices, the choice of force smearing becomes very important. Martínez-Tossas et al.[36] indeed found a large dependence on the smearing length for the power output, probably related to the influence of the tip vortex. They also recommend $\epsilon \geq 2\Delta x$ for stability, as also found by Troldborg[82]. Churchfield et al.[13] on the other hand found a guideline of $\epsilon \approx 0.035D$, where D is the diameter of the rotor.

To make the AL method more robust, more research is done on how the force smearing can be optimized. Similarly as for the AD, Mikkelsen[42] argues that using a 3D kernel, forces are spread over a larger radial distance than the span of the blades. Instead, he proposes an alternative 2D Gaussian kernel, according to Equation 2.19 and Equation 2.20. Shives and Crawford[66] build on this approach by considering that the forces should be spread over "physically meaningful length scales". They concluded from this that the smearing length should scale with the local chord length, finding good results for $0.125 < \frac{\epsilon}{c} < 0.25$ using RANS. Similar results were found with an analytical solution from Martínez-Tossas et al.[37], although confirmation of their validity in LES is not yet provided.

$$\mathbf{f} = \frac{1}{\Delta V} (\mathbf{F} \otimes \eta_{2d}) \quad (2.19) \quad \eta_{2d} = \frac{1}{\epsilon^2 \pi} e^{-\frac{d^2}{\epsilon^2}} \quad (2.20)$$

Instead of just considering the chord length as relevant scale, some research has focused on shaping the complete smearing in such a way that the resulting load matches an airfoil loading more closely. Churchfield et al.[13] used an anisotropic three-dimensional Gaussian kernel, effectively specifying a radial length scale, a chord length scale, and a thickness length scale, according to Equation 2.21. Schollenberger et al.[62] expand on this even further by introducing a Gumbel distribution, mimicking the shape of an airfoil load distribution, as done in Equation 2.22.

$$\eta = \frac{1}{\epsilon_r \epsilon_c \epsilon_t \pi^{\frac{3}{2}}} e^{-\frac{d_r^2}{\epsilon_r^2}} \cdot e^{-\frac{d_c^2}{\epsilon_c^2}} \cdot e^{-\frac{d_t^2}{\epsilon_t^2}} \quad (2.21)$$

$$\eta = \frac{1}{\epsilon_r \epsilon_c} e^{-\frac{d_r^2}{\epsilon_r^2}} e^{-\frac{d_r}{\epsilon_r}} e^{-e^{-\frac{d_c}{\epsilon_c}}} \quad (2.22)$$

However, introducing anisotropy in the smearing could cause some issues when evaluating the local velocities required for BE analysis. This is because when evaluating the relative velocity of the blade element, the local blade freestream has to consider the effects of blade rotation and gross deceleration of the rotor, while the self-induced velocities caused by the blade bound circulation should be ignored[13]. For radially symmetric kernels, this self-induced velocity will be zero in the midpoint of the kernel, but for anisotropic kernels this is no longer necessarily the case. Churchfield et al.[13] acknowledged this effect and avoided it by using a spatially weighted sampling method. Although mathematically sound, this method significantly complicates the evaluation of the freestream velocity.

Result-wise, Churchfield notes that blade loading near the tip better matches experimental results, which he attributed to a better representation of the tip vortices. However, other investigations, such as those by Melani et al.[38], conclude that anisotropic kernels do not improve the loading characteristics near the tip, but instead increase the uncertainty in angle of attack. It should be noted that Melani did not use the same spatial velocity sampling as Churchfield. Melani continues by mentioning that the tip vortex resolved by AL is more diffusive than the one obtained from geometry-resolved CFD.

A possible explanation for this is given by Meyer Forsting et al.[41], who derive that the effect of the convolution with the smearing kernel is mathematically equivalent to introducing a viscous core to both the bound and the trailing vortex. According to Lifting Line theory[2] the tip vortex effect is accurately represented by a potential vortex. As such, it is expected that smearing the forces underestimates the induction in the (near) wake. Meyer Forsting goes on to derive an equation for this missing induction and uses it to define a tip-correction for AL methods. The correction seems to hold for general cases, including yaw, turbulence, and pitch changes.

Actuator Surface In Equation 2.1.4.1 it was seen that some attempts were made to shape the load distribution of AL methods to better describe the load distribution of an airfoil. The Actuator Surface (ASF) model, originally developed by Shen et al.[64], addresses this issue by using more elaborate airfoil data.

In their approach, the airfoil load is spread over a plane in such a way that it resembles the pressure and shear distribution of the turbine blade. Where for AL only the lift and drag polars are required, ASF requires a more elaborate understanding of airfoil dynamics, which can be obtained from viscous airfoil solvers like XFOil. Since XFOil performs steady calculations, a dynamic stall model can be included to increase the accuracy of the polar[66].

As a big advantage, an accurate representation of the airfoil loading can be projected onto the LES grid. This also removes the ambiguity in the smearing width encountered for other methods, since it is now explicitly used to fit the distribution into the correct shape. It was hence also found that the tip loading of the blade was more realistic[65], causing the resulting fidelity to be between AL and blade-resolved CFD.

On the other hand, the method is even more complicated than AL and requires a significantly larger amount of aerodynamic insights of the airfoil, as well as a finer mesh density. Meanwhile, due to its high computational cost, its application is limited to single wake wind turbines[66]. But for single rotor analysis, it is also possible to fully resolve the blade geometry, as described in subsection 2.1.3. As such, the ASF method is currently often not seen as worthwhile, adding to much complexity and costs for only small increases in accuracy. However, as the results do seem promising, it might be an excellent method for future use when computational capabilities have been further increased.

Actuator Sector Currently the majority of wind farm simulations are carried out using AD models, simply due to computational constraints[66]. Still, AD models fail to capture azimuthal trends, such as tip and root vortices, and therefore fail to correctly resolve near-wake phenomena. As such, there is a demand for models that can properly model tip loading, while staying at acceptable costs. Based on this idea, Storey et al.[79] defined the Actuator Sector (AS) model.

Sometimes also referred to as the Sweepled Actuator Line model[48], the AS model works by smearing the blade forces over a sector of the rotor disk, representing a time integral of the blade movement during a time step of the LES. More specifically, the sector is divided into many lines, where each line is subdivided into different segments, just as for a normal AL approach. Then the forces for each line segment are calculated using a BE technique and divided by the number of lines, assuming the contribution of each line to be equal. The actuator forces obtained can then be projected onto the LES using a convolution kernel, as described in subsection 2.1.4.1 and Equation 2.1.4.1. An illustration of the obtained force distribution compared to AD and AL is provided in Figure 2.6[44]

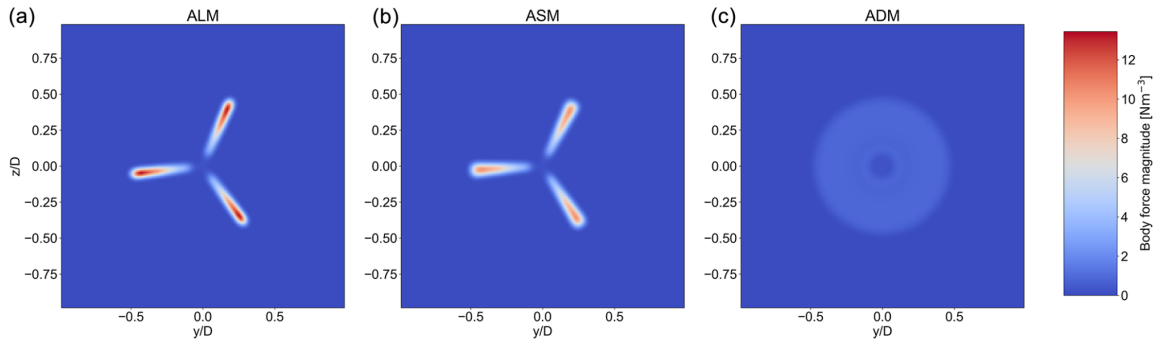


Figure 2.6: Comparison of the body force distribution obtained from AL (a), AS (b) and AD(c). Figure obtained from Mohammadi et al.[44]

Although the AS method might seem like adding unnecessary complexity to the AL method, it is completely justified by the resulting decrease in time-stepping requirements. Storey et al.[78] found that the AS model greatly increased accuracy as compared to the AD, since now radial and azimuthal gradients in the flow field could be resolved. The results also compared well to AL, while the computational effort was significantly reduced. In some test cases, the AS was even faster than the AD method, probably attributed to a faster convergence of the pressure solver.

A more thorough validation has been performed by Mohammadi et al.[45]. In this study, tests have been done to remove some of the ambiguity around the method, the largest problem being the velocity sampling procedure. In an initial approach, the sampling might be done for each line separately to extract as much local information as possible. However, as explained in Equation 2.1.4.1, the sampling should be done in such a way that the induction by the bound circulation of the blade is neglected. This can be difficult, since the total force projection of the sector is not necessarily axisymmetric. Mohammadi found that sampling at 70% of the sector gives results that are within 1.5% of the results of AL. A more exact sampling location could possibly be derived using the method of Churchfield[13], which was also discussed in Equation 2.1.4.1.

2.1.4.2. Analytical Body Forces

In subsection 2.1.4.1, several different types of Actuator Models were distinguished, based on the projection strategy of the forces onto the main grid. However, to project a force onto the LES, its distribution must first be known. In the majority of literature this is done using either of the following methods.

The first and easiest method is to assume the force distribution to be uniform. This greatly simplifies the force calculation, but also neglects a significant part of the wake dynamics. This method is therefore rarely used in recent literature. A second option is to use a scaled reference load distribution as illustrated by Van der Laan et al.[31]. This works fine for simple cases, but might be hard to generalise if the inflow conditions vary a lot over time. By far the most popular method nowadays is to use a coupling to BEM to calculate the forces[54, 91, 75]. The BEM solver is very cheap with respect to the LES and can thus be used to calculate the loads during the simulation without further computational problems.

However, BEM requires detailed knowledge about the turbine geometry, including blade geometry and airfoil aerodynamic properties. In academia, reference turbines are often used for this purpose, but in industry the values for the actual turbines are generally unknown. As such, industry LES simulations

are largely based on the simplified uniform AD model. This not only limits the fidelity of the simulations, but it also makes it impossible to perform any kind of load assessment, since no information about the load distribution is known.

Recently, some efforts have been made to resolve this issue. In their work, Sørensen et al.[75] defined an analytical body force model which can predict the normal and tangential force distributions, if the total thrust, power, and tip-speed ratio of the turbine are known. These values in turn are obtained from the characteristic turbine curves, which are one of the few pieces of specific info that a manufacturer usually provides. The analytical model has been verified by Sørensen and Andersen[71]. Here, it was found that the model works well at the turbine design point, but performs significantly worse for off-rated conditions. A follow-up paper by Sørensen[72] fixes this issue by introducing an additional solid-body wake-rotation term.

In the original paper, it was also shown that it is possible to couple the model to a LES[75], however it was not directly clear how the freestream condition required for the model should be defined. This issue was addressed by Navarro Diaz et al.[49], who made a distinction between the apparent freestream, which differs for each point of the disk, and the reference velocity, which is constant for the entire turbine. To achieve the coupling, they note that the disk velocity is resolved in the CFD and can be used to estimate the freestream velocity using Equation 2.23. Here U_0 is the distribution of freestream velocity, u_d the distribution of disk velocity and \bar{a} the average induction factor, which is found from the 1D approximation $C_T = 4\bar{a}(1 - \bar{a})$.

One consequence of this coupling is that the disk velocity, which originally was a degree of freedom of the model, is now determined by the LES. As such, the power constrained has to be dropped to ensure the system is not over-constrained. The resulting power obtained by the turbine will then match with the imposed induction. This is generally a disadvantage, since the power coefficient was a useful input to match the tangential force distribution with the observed turbine power, which is easily obtained by a turbine curve. The exact effect, however, has not yet been investigated.

$$U_0 = \frac{u_d}{1 - \bar{a}} \quad (2.23)$$

The analytical model is very generalised and, as such, barely requires any information of the turbine geometry. It is therefore an excellent candidate for increasing the fidelity of industry simulations. Although designed for use in AD simulations, Navarro Diaz et al.[49] showed that the model can also be used in an AL framework with only very slight modifications.

It should also be noted that the model is still very new and not widely used. For as far as known, the model has not yet been applied in simulations with more than a couple of turbines. Even more so, the papers mentioned above cover, to the best of the author's knowledge, all literature that is available for this topic at the current moment.

2.2. Wind Farm Analysis

While section 2.1 provided several great options for quantifying the performance of a single rotor, wind turbines can often not be seen as an isolated system. There is a strong interaction with both their environment and other nearby turbines within the farm and a realistic analysis should take those effects into account. In subsection 2.2.1 it will be briefly explained how environmental and farm side specific conditions are taken into account. On the other hand, subsection 2.2.2 will explain how turbine behaviour is modeled in an efficient way for these large simulations. The section will end with a description of the ASPIRE solver that is used within Whiffle in subsection 2.2.3.

2.2.1. Atmospheric Modeling

Although the preliminary analysis of turbines often considers simple flow cases, such as homogeneous laminar inflow, the reality is significantly different. Inflow conditions are governed by both large-scale and more local weather phenomena, giving rise to an Atmospheric Boundary Layer (ABL)[3]. Within meteorology, great emphasis is placed on understanding this ABL, as covered in the work of Stull[81].

Since the atmosphere still adheres to the Navier-Stokes equations, techniques similar to those in subsection 2.1.3 can be used to investigate the ABL. However, where for rotor dynamics LES is infeasibly expensive, the large atmospheric scales allow up to 90% of all turbulent kinetic energy to be resolved for typical ABL grid sizes[25]. As such, atmospheric modeling using LES is much more realistic and has even become one of the dominant tools for investigating the ABL[77]. An additional advantage is that transient phenomena are automatically included in such an analysis, which gives a far more complete description than can be obtained by alternative dynamic wake models[3].

Throughout the last half century, LES has been applied to an increasing number of complex phenomena. Brown[9] for instance, used LES to successfully simulate the diurnal cycle of cumulus convection. Diurnal patterns are often characterized by maximum wind speeds that occur at the same time of day, possibly from similar directions[18]. As such, the correct prediction of these cycles is critical, not just for wind resource assessment, but also for power forecasting. Similarly, complex terrain, such as hills, can significantly alter local wind conditions, as treated in the work of Uchida and Ohya[84].

With all these advances, academia is slowly working towards an almost universal weather model. In their work Schalkwijk et al.[60] showed that it was indeed possible to perform a stable simulation for a period of a year using LES. Today, many different solvers are available, where at Whiffle the ASPIRE (Atmospheric Simulation Platform for Innovation, Research and Education) solver is used. This solver is based on the older formulation of DALES (Dutch Atmospheric Large-Eddy Simulation), which is an all-round model that is validated for many different cases, as described in the work of Heus et al.[25].

LES seems like a natural fit for modeling the atmosphere, since many complicated phenomena, such as turbulence and transient behaviour, are inherently included in the method, which leads to a lower need for parametrization compared to other large-scale weather models[25]. Additionally, Whiffle has proven their ability to create effective ABL solutions for a wide variety of conditions, making use of their ASPIRE solver, which will be discussed in more detail in subsection 2.2.3. These solutions are now also being ported to industry, where they are used for advancements in meteorological forecasting, power forecasting, and wind resource assessment[86].

2.2.2. Turbine Interactions on Farm Level

In subsection 2.2.1 it was seen that LES provides a powerful framework to calculate the ambient conditions in a wind farm. However, the wind turbines themselves also cause a large interference with their wakes, so for good predictions within the farm itself, the turbine influences should be included in the simulation. For optimal accuracy, it would be ideal to completely resolve the turbine blade geometry, as discussed in subsection 2.1.3. However, accurately resolving far wake characteristics using this method is already a challenge for a single rotor[99], let alone simulating an entire wind farm. As such, the actuator methods of subsection 2.1.4 are almost always used in practice. Still, simulation of complete farms remains a challenging topic and several problems should be considered when choosing a model.

The first problem that has to be addressed is the calibration of the actuator methods to produce the correct power and thrust. When Equation 2.14 is used, the thrust and power coefficients are found using the turbine curves provided by the manufacturer. The thrust and power are then determined as a function of wind speed. Similarly, when local velocity data are required, independently of the actuator method chosen, the rotational velocity of the turbine is a model input such that knowledge about the TSR is required.

This data is readily available when the turbine inflow is relatively constant. However, for turbine arrays operating in each other's wakes, the apparent freestream velocity is no longer trivially defined. As such, the turbine curves can not directly be used. The correct values for thrust coefficient, power coefficient, and rotational velocity can then be obtained from a calibration procedure, as investigated by Van der Laan et al.[33]. By running a set of single wind turbine simulations at a constant inflow using the inexpensive BEM method, a transformation can be defined such that C_T , C_P , and λ are given as a function of the average disc velocity, rather than the freestream velocity. This approach has been successfully adopted by Allearts and Meyers[1]. For the BE approach, Van der Laan et al. define an alternative calibration based on the torque-rotational speed relationship of a turbine, based on the work of Wu and Porté-agel[92].

Another factor to consider is the computational cost to ensure stability, which must consider the time-stepping of the transient LES. To ensure stability, the Courant-Friedrichs-Lewy (CFL) number, given in Equation 2.24, should be less than one. For an AD simulation, the general speed in a computational cell is in the order of the free stream velocity, or even lower in the wake. However, in an AL simulation, the blades sweep through the rotor disk, where the tip has a lateral velocity of $U = \lambda U_\infty$. As such, to meet the CFL requirements, the time step must be reduced by a factor λ . Additionally, the AL mesh is generally more refined than an AD mesh, leading to higher computational costs and even lower time steps.

$$CFL = \frac{U\Delta t}{\Delta x} \quad (2.24)$$

Another way to interpret Equation 2.24 for the AL is that the tip of the blade can not travel more than a single mesh cell per time step. For the AS, on the other hand, a time integral of the force is considered over the entire LES time step. Therefore, the sector can overlap multiple mesh cells without causing discontinuities in the applied force[78]. As a result, the CFL criterion for AS is similar to that of the cheap AD method. In practice, the method can be slightly more expensive, due to the increased mesh resolution required to capture the radial and azimuthal force distribution of the blades in sufficient detail.

2.2.3. The ASPIRE solver

The ASPIRE solver is a home-made, all-scale, LES-based weather model that is used within Whiffle for a variety of power forecasting, weather forecasting, and renewable yield modeling purposes[86]. The model is based on the older DALES model, which is used by the KNMI, the Dutch meteorological institute, as well as many Dutch universities[25].

Where many academic studies have focused on the simulation of a specific weather condition, the DALES platform has continually been extended to include more and more functionalities. As such, it is today considered to be "one of the most all-round tested available LES models for studies of the ABL"[24]. With excellent validation results, DALES has proven to be accurate for many ABL flows, such as convective, stable, and cloud-topped boundary layers. In addition to that, it has proven useful in the study of sheared flows, dispersion studies, turbulent reaching flows, and heterogeneous terrain. The last one also refers to the ability to model sloped terrains such as hills.

ASPIRE's capabilities even slightly surpass DALES by coupling the simulation to a large-scale weather model[85]. This possibility allows for a better description of the boundary conditions of the LES, which enhances its capabilities for forecasting purposes. On top of that, a microphysics module is present in ASPIRE, which better describes the evolution of different water phases in a cloud. In combination with the inelastic approximation, ASPIRE gives superior results for cases of deep convective clouds[85].

But the main thing that separates ASPIRE from other solvers is that it is GPU-Resident. This means that all data are processed on the graphical card, with minimal to no interaction with the CPU. Since the CPU-GPU data bus provides significant overhead, a GPU-resident system provides significant speedup compared to a CPU or coupled CPU-GPU system.

The solver is based on a formulation of the Navier-Stokes equations in the context of atmospheric flows. This results in four equations, which are continuity, conservation of momentum, heat transport and moisture transport, given in Equation 2.25–Equation 2.28. Here ρ_b is the reference density, u_j the LES-filtered velocity in a given direction, b the buoyancy parameter, δ_{i3} the Kronecker delta f_c the Coriolis parameter, u_j^g the component of the geostrophic wind, τ_{ij} the subgrid stress tensor, F_j^θ and F_j^q the subgrid fluxes of θ_i and q_t and S_{θ_i} and S_{q_t} a source term. Note that the formulation of momentum differs from DALES, since an anelastic approximation is used instead of the more standard Boussinesq approximation.

$$\frac{\partial \rho_b(z) u_j}{\partial x_j} = 0 \quad (2.25)$$

$$\rho_b \frac{\partial u_i}{\partial t} = -\frac{\partial \rho_b u_i u_j}{\partial x_j} - \frac{\partial p}{\partial x_i} + \rho_b b \delta_{i3} + f_i - \frac{\partial \tau_{ij}}{\partial x_j} + \epsilon_{ij3} f_c (u_j - u_j^g) \quad (2.26)$$

$$\rho_b \frac{\partial \theta_l}{\partial t} = -\frac{\partial \rho_b u_j \theta_l}{\partial x_j} - \frac{\partial F_j^\theta}{\partial x_j} + S_{\theta_l} \quad (2.27)$$

$$\rho_b \frac{\partial q_t}{\partial t} = -\frac{\partial \rho_b u_j q_t}{\partial x_j} - \frac{F_j^q}{\partial x_j} + S_{q_t} \quad (2.28)$$

Further equations for governing thermodynamics and microphysics are available. These equations can be turned on depending on the problem at hand and can be very important for different problems involving cloud formation. The equations are all discretized on an Arakawa C-grid, see Figure 2.7[85]. Here, all variables are located in the cell centers, except for the velocities. The velocity values are located at the center of each face for the corresponding direction, thereby effectively decoupling the pressure and velocity discretisation. The Arakawa grid is per definition a rectilinear grid, which allows for low discretisation errors and optimal implementation on a GPU.

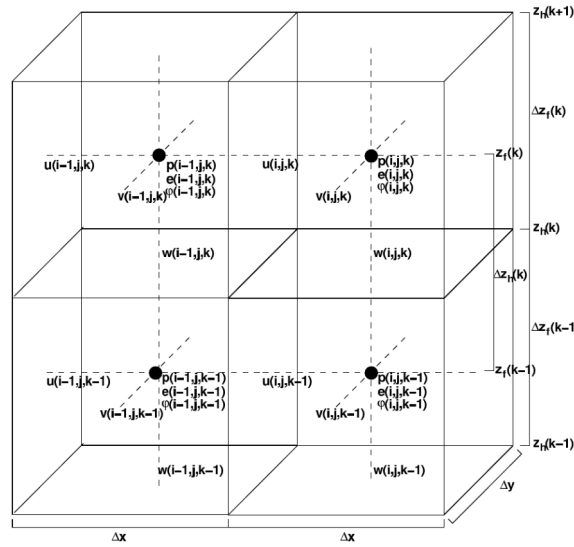


Figure 2.7: The numerical grid for discretisation of the equations. Figure obtained from the ASPIRE documentation[85]

Since the LES equations govern the filtered quantities, sub-grid contributions have to be accounted for explicitly in the equations. For this, a multitude of sub-grid models are available. Apart from that, a Meso-scale model can be used too, which does not explicitly resolve turbulence. This method therefore resembles a kind of URANS simulation, which can be perfect to capture weather phenomena of the largest scales. The Meso model is therefore often used as an intermediate coupling inside a nested simulation, to increase the fidelity between the domain boundaries given by large weather reanalysis data sets such as ERA5 and the boundaries of the LES itself.

Boundary conditions can be supplied in different ways. The domain is generally defined as a large box. The upper face is constrained by Neumann conditions for all variables, except the vertical velocity, which is set to zero using a Dirichlet condition. In the stream-wise and span-wise direction, the inflow can be specified, while the outflow can then be chosen as periodic or prescribed. The latter is often used in the context of numerical weather prediction. The bottom boundary condition governs the interaction with the ground itself, for which many different models are available. These models govern how the roughness interacts with the ABL using a variety of wall models. Since ASPIRE is built as an atmospheric flow model, it is very easy to setup simulations for a given region on earth during a specific time frame. The solver then automatically assembles the boundary conditions, gathering initial weather conditions from the ERA5 reanalysis data set[23]. Satellite imagery and other data sets are also used to determine the appropriate roughnesses at every grid box of the lower boundary.

The solver is highly customizable by the use of plugins. These plugins can be used to add source terms to the transport of any quantity at any time step, thereby influencing its evolution. Because of this flexibility,

plugins can be used for rapid development and testing of new models, which makes the solver easily extendable.

The wind turbines are integrated as a plugin and are modeled using an actuator model. For this, the Actuator Disk and Actuator Line models are available. The AD model is ASPTurbine and discretises the turbine using a uniform normal and tangential force distribution, based on the integral thrust and power obtained from the turbine curve. The AL implementation, on the other hand, is called ASPFast. As the name suggests, this model uses a coupling to OpenFAST to calculate the turbine forces. Both models use the 3D Gaussian kernel to project the forces onto the LES grid. Although functional, ASPFast is generally too expensive and in an operational setting and therefore Whiffle uses ASPTurbines for the majority of their projects.

2.3. State-of-the-art

The techniques used to evaluate the performance of wind turbines at both the individual and farm level have been discussed in great detail in section 2.3. As this thesis will make use of ASPIRE, an advanced, industry-oriented solver particularly suitable for complex ABL flows, the focus on isolated turbines will now be dropped. Instead, state-of-the-art techniques for evaluating the dynamic interaction between turbine-turbine and turbine-environment will be investigated in this chapter. The main subject of the thesis is the determination of individual blade loadings using LES techniques. However, as this is heavily dependent on accurate simulation of wind farms in the first place, some literature regarding this will also be analyzed.

In subsection 2.3.1 an overview will be given of several different branches within recent wind farm research, unraveling new approaches to understand wind farm dynamics and improve future power gains. Then subsection 2.3.2 will identify the knowledge gap in the current literature, based on the studies of subsection 2.3.1.

2.3.1. Applications of LES to Wind Farms

Currently, much research is being done to better understand wind farm dynamics. Although the huge amount of research output makes it impossible to give a complete overview, this section will present a selection of promising studies performed in literature, spanning a range of different topics. These topics have been selected because they clearly illustrate state-of-the-art computational techniques, while also highlighting several issues that are encountered when extending the framework to industry.

First, subsection 2.3.1.1 will discuss some of the developments in understanding wake interactions and how to control them. Then subsection 2.3.1.2 will discuss the global blockage phenomenon, which was only recently discovered to be impactful. Next, subsection 2.3.1.3 will follow with an investigation of wind turbines in complex terrain. The section will end with an analysis of turbine blade load assessment in subsection 2.3.1.4.

2.3.1.1. Wake Interaction studies

One of the reasons that LES is so suitable for wind farm simulations, is that it directly simulates many of the phenomena of interest, without further modeling requirements. As a transient method, the wake development behind a turbine is given in a physically accurate, time-resolved way. As such, LES simulations are performed for many interaction studies.

Wu and Porté-Agal[91] investigated the interaction between a single turbine wake and the ABL using AD methods both with and without tangential forcing. The results were compared to wind tunnel measurements, and both methods were found to give good results for the far wake, with the rotational method significantly outperforming in the near wake. Martín-Tossas et al.[36] found similar conclusions and extended the analysis to AL. Here the AL was able to resolve flow structures near the blade tips that the AD could not.

These studies formed a good basis for validation, which allowed the simulation of more complex cases. In their studies Allaerts and Meyers[1] simulated an array of 48 wind turbines, using AD without wake rotation in a neutral ABL. Here, periodic boundaries were used, effectively simulating the effect of an infinitely wide wind farm. Based on LES, they found that the wind farm power production is directly related to meteorological parameters, the most important ones being the height and strength of the

inversion layer. Wu and Porté-Agal[92] on the other hand performed simulations on the Horns Rev off-shore farm in the Danish North sea, a popular site in literature with available data on power production. For their simulation, they used an LES method where the turbines were represented using AD methods with and without rotation, where it was found that power prediction accuracy increased when the rotational effects were taken into account, while the simple AD consistently underestimated the power. The same negative bias was found for WindSim and WAsP, two common wind farm design tools.

In addition, their findings suggested that power production showed a significant dependence on wind direction. This was also addressed in one of their other studies in collaboration with Chen[53]. In this study, it was found that wake losses could constitute a power loss of up to 40% for specific wind directions. This in turn was caused by a full waked condition between neighboring turbines, with a decrease in the distance in the stream direction with respect to atmospheric flow. Interestingly enough, changes in the wind direction of only $\pm 10^\circ$ around this power minimum showed a relative increase in power of up to 43%. As they state, this effect "has important implications for the design of wind farms and the management of the temporal variability of wind farm power output and its integration to the electrical grid".

With a better understanding of these wake effects, recent efforts have focused on defining strategies to reduce these losses. Although largely dependent on the wind farm design itself, there is an increasing interest in control strategies to optimize power production. Current turbines are operated using a "greedy control" approach, maximizing the power production of each individual turbine[3]. However, due to the strong wake influence between the turbines, recent research has shown that large energy gains can be made by instead optimizing the power production of the farm as a whole.

Munters and Meyers[47] investigate this possibility using a so-called power de-rating, or dynamic induction control approach. In this approach, upstream turbines deliberately operate at lower than optimal thrust coefficients, in order to reduce their wake influence on downstream turbines. They show that when done on full farm level, this can result in a theoretical increase of 8-21% in farm yield.

An alternative approach considers wake steering by letting some turbines deliberately operate under yawed conditions. Here, Storey et al.[80] investigated the effect of adding dynamic yaw control to the simulation. As a result, the turbines could adjust to local flow effects, even if the upstream wind direction did not change. They noted that indeed yaw actuation was triggered by the transient wake effects of upstream turbines and that this should be included for correct simulation of a turbine array.

2.3.1.2. Farm Blockage

For the longest time only wake effects have been considered when evaluating the turbine-turbine interaction. The turbines were known to have an induction zone upstream, which in theory could influence other turbines, but this zone was found to be small and was generally neglected[6]. Only recently was it discovered that this assumption does not hold for complete wind farms that interact with the ABL. Here, the effective induction zone of the wind farm is significantly larger than expected from the sum of the induction zones of all individual turbines[61]. This phenomenon is now often referred to as global blockage or farm blockage.

Even today this topic has only been investigated sparsely and its influence is generally not included in engineering models. The global blockage effect was first observed in measurements by Bleeg et al.[6], only in 2018. By comparing the measurements of meteorological masts upstream and laterally of a wind farm, before and during operation of the wind farm, they found a significant reduction in free stream velocity just upstream of the farm after the wind turbines came into use. Similar results were obtained when simulating the site using RANS.

Schneemann et al.[61] continued this work by investigating global blockage effects using lidar data. They also found a decrease of about 4% in the upstream free-stream velocity, attributed to the presence of the wind farm itself. The first rows of turbines can similarly be influenced by this effect, leading to a reduction in the expected farm energy production. An in-depth understanding of this topic is largely based on LES investigations of larger wind farms.

One of such investigations was performed by Wu and Porté-Agal[90], where they simulated the effect of a 36 by 5 wind turbine grid with a spacing of 7 turbine diameters. They repeated the simulation for aligned and staggered setups and also with periodic boundaries to simulate an infinite wind farm.

Indeed, a turbine induced global blockage effect of about 1% reduction in the upstream free flow was found for free-atmosphere stratification. For higher levels of atmospheric stratification, this effect could be significantly increased, due to gravity wave induced blockage effects causing a high pressure at the leading edge of the farm.

2.3.1.3. Complex Terrain

In subsection 2.2.1 it was already discussed how advances in atmospheric sciences allow for the simulation of the ABL in a wide variety of landscapes. Over time, the wind energy community has adopted these techniques and applied them to investigate the potential of wind energy in complex terrains. In their work, Elgendi et al.[17] give a great overview of a variety of terrain types that are of particular interest for onshore wind energy applications. For each type, they also present a range of studies investigating the wind characteristics of such landscapes.

These studies show that many types of terrain can be beneficial for the development of onshore wind turbines. Especially hilly or mountainous terrain can generate large local accelerations of the mean flow field, leading to a higher possible energy extraction if a turbine is placed correctly. However, to properly understand this behaviour, only evaluating the wind characteristics on their own is not enough. Instead, the interaction of turbine-environment and turbine-turbine should be explicitly considered.

The first proper investigation of an operational wind farm in complex terrain using LES appears to have been carried out by Yang et al.[94]. In this study, they simulated the InvEnergy Vantage wind farm in Washington, USA. This farm consists of 60 1.5MW turbines, spread over an area of roughly 9x4 km, with terrain height varying by roughly 300m. Even for this challenging terrain, the values obtained for mean power and power fluctuations closely matched observations, validating the approach for LES even for such complicated cases.

Sing and Alam[67] extend this approach to a case study of a 12 times 5 turbine array on a variety of hypothetical terrains. Using this approach, they can investigate the effect of local flow accelerations versus the increased drag interactions that are also often encountered in these circumstances. Their conclusion is that power production could theoretically be increased by up to 68% with respect to a wind farm in a flat region. As such, the benefits of local flow gradients far outweigh the effects of drag increases.

In addition to wind farm applications, recent research has also focused on the turbine-environment interaction for a single turbine. Troldborg et al.[83] investigate the effects of complex terrain on the power curve of the DTU 10MW reference turbine. This is done by simulating the turbine in both a flat environment and a complex environment, for which the Perdigão site in Portugal was selected. The resulting power curves for the two sites were found to be significantly different. This discrepancy was attributed to the heterogeneity of the complex terrain flow, which significantly interfered with the turbine wake.

Now that the techniques of simulating complex terrain are becoming more mature, the possibilities of including them into a simulation procedure are also growing. In their work, Rai et al.[56] define a generic framework for the use of AL methods in a LES, capable of resolving complex terrain. Working with such a framework allows for simulations that are easier to set up, more robust, and easier to optimize.

The ASPIRE solver can also be seen as such a framework. Plugins can be added to the solver in a modular way, enabling easy extensions of the base capabilities of the solver. Apart from that, complex terrain can readily be solved by the solver using immersed boundary methods[85].

2.3.1.4. Load Assessment of Individual Turbines in a Wind Farm

Apart from wake losses, the study of wake interaction is also relevant for the structural design of turbines. The wake area is categorized by large velocity deficits and increased levels of turbulence, which can cause a large time-wise variation of blade loading. As such, turbines placed in the wake of another turbine suffer significantly higher fatigue loads than in an isolated environment. Similar turbulent effects can be observed when a turbine is placed in complex terrain, such as the flow-separated region behind a hill.

Some research has focused on quantifying these fatigue effects. The study of Storey et al.[80] was already mentioned for its implementation of yaw control into the LES simulation using actuator sections.

In addition, this study also focuses on the variability of load of a four-turbine array at different ambient wind speeds. They found that at below-rated conditions, the front turbines experienced higher loads due to the reduction of wind speeds in the wake for the downstream turbines. However, at higher wind speeds, the rated speed could still be reached in the wake. As a result, the average force on the downwind turbines was greater due to the large power fluctuations caused by the turbine speed control. Similarly, they found that at lower wind speeds, the coefficient of variation of blade loading was higher for downstream turbines, due to the influence of turbulent wakes. However, at speeds above rated, the front turbine suffered from significant force variability due to the need of pitch control on the blades.

Some researchers have also extended the AL model to incorporate aero-elastic effects by coupling the model to a structural solver. Especially for larger turbines this might be important, as large blade deflections could influence the flow field. As such, Meng et al.[39] propose an Elastic Actuator Line model (EAL). In this model, structural effects are incorporated in a similar manner as often done for BEM methods, such as FAST.

In the EAL the calculation of the blade forces is again performed using a BE approach. However, when determining the local velocity and angle of attack, the EAL will now also consider bending and vibrational movements of the blades, thereby enhancing the physical accuracy of the representation. Using these techniques, Meng et al. showed that the impact of aero-elastic effects can not be neglected when calculating the time series of root bending moments. They also investigated the case of a turbine that is partially in the wake of another turbine and concluded a significant increase in fatigue loading.

One limitation of the study is that the model was adopted using RANS, which can only calculate the mean turbulence quantities. Yu et al.[95] therefore employed a similar EAL model, but now in a LES framework. On top of that they include the effect of tower shadow in the analysis as well. The tower was found to significantly affect the fatigue characteristics of the turbine, especially when the tip moved closer to the tower under high loads. These effects were further strengthened when turbines were considered in the wake of upstream turbines.

2.3.2. Challenges in Industry

In subsection 2.3.1 it was shown that great developments have been made in understanding the dynamics of wind farms. However, this does not mean that all challenges have been solved. Within academia, many different case studies exist and new insights are obtained almost daily. Still, not all of these advancements are transferable to industry. This section will focus on some of the issues that industry-scale LES simulation encounter and which advancements are required to allow LES to thrive as a business case.

The largest issue holding LES back for use in the industry is its computational cost. Looking back at subsection 2.3.1, it can be seen that AL computations are relatively rare, even though they are widely accepted to be better than AD. This is due to the computational requirements, where AL not only requires a finer mesh to resolve the force gradients, but is also extremely limited by the CFL requirement, as was explained in subsection 2.2.2. As such, simulations of large wind farms are predominantly being performed using AD, even in academia. However, academia usually focuses on well defined case studies, simulating usually a single given day. To sell a service however, it is not uncommon in the wind industry to have a reference data set of 20 years. As a result, industry is limited to AD computations on coarse resolutions to be able to keep up with the computational demand.

Another problem is the secrecy of data. Turbine manufacturers generally only provide the characteristic turbine curves, along with very general numbers, such as size and rated power. Unless the turbine is very old, the chances of obtaining an accurate BEM model are very small. As seen in subsection 2.1.4.1, BEM is a very common method to provide a load distribution to the LES in academia. Although perfect from an algorithmic point of view, the lack of data makes it impossible to implement for real-world wind farms.

Luckily, there are possibilities for future development. The analytical models discussed in subsection 2.1.4.2 seem very promising. Implementing such a model into industry LES is expected to greatly enhance performance with respect to the uniform AD models that are currently used by lack of a better alternative. In the best case, these models could match BEM-coupled AD models, allowing industry LES to operate on the same fidelity as state-of-the-art wind farm simulations in academia.

More specifically, the analytical body force model (ABFM) provides opportunities in two ways. In the latest paper on development of the model[72], it is clearly presented as an algorithm that takes in the thrust coefficient, power coefficient, and tip-speed ratio, and returns the expected force distributions based on some simple physical considerations. In a first approach, it is thus not even required to create a two-way coupling to the LES. Existing LES data using a simplified, uniform AD can be used to generate the required inputs for the ABFM, which is in turn used to estimate the force distributions. This way, companies can provide estimated turbine loads as an extra service, without changing their computational setups.

The methodology could then be expanded, if desired, to include the full two-way coupling. This will require a significant change in the LES workflow, but it enables the LES to use the higher fidelity load distributions in the force projections. This will likely result in a higher accuracy of the results in the wake. The use of this two-way coupling has already been demonstrated in literature[75, 49]. The one-way approach, however, could also be very valuable, but has not been investigated as of yet.

Apart from that, it should be mentioned that the Actuator Sector approach could also be very interesting for industry purposes. For all practical intents, it blends the AD and AL methods and can thus be used for cases where higher fidelity than AD is preferred. The blending factor is directly related to the maximum time step. If the same timestep as AL is used, the method will converge to the AL result. However, if the timestep is very large, the sectors will span the entire disk and the simulation will behave as an AD. Still, current Actuator Sector models rely on a coupling to BEM and are thus not applicable for industry. However, if the force distribution can be resolved in other ways, such as the ABFM, the actuator sector approach could be applied to real-world cases as well.

2.4. Goals of the thesis

The previous sections have discussed the history and current state-of-the-art approaches for turbine analysis. LES has become a staple in academic research for this purpose, as it can capture both the dynamics of the ABL and the turbine wake. Although less common, LES is slowly being applied in industry settings as well. However, due to confidentiality, application of LES in this field often has to be performed with a lack of turbine parameters. As such, they are limited to simplified, uniform Actuator Disk models. This thesis will focus on how analytical body force models can be used to enable the calculation of blade force distributions in industry-scale LES of wind farms. It is aimed to develop a model that can be used in a general context for a wide variety of cases. The exact research questions are defined in subsection 2.4.1 and the hypothesis in subsection 2.4.2.

2.4.1. Research Questions

Currently, the fidelity of LES applied by industry to wind turbines is limited by the fact that the blade load distributions are generally unknown. The quality of the simulations can greatly be improved if the blade loads can be calculated. The main research question is thus formulated as follows:

- How to develop an efficient model for wind turbine blade loads in a wind farm integrated in an industry-scale operational LES model, without knowledge of the blade geometries?

As mentioned in subsection 2.3.2, an analytical body force model is a promising solution to this question. The model of Sørensen[72] is thus taken as a starting point, this thesis will then investigate how this model can be adapted for industry use. This leads to the following three supporting research questions:

1. How can existing analytical body force models be coupled to a LES in such a way that they match both the input thrust and power coefficient?
2. With what accuracy can the analytical body force model be used to calculate force distributions using a one-way coupling approach?
3. How much can the accuracy of the wake in the LES be improved by using the analytical body force model with respect to a uniform actuator disk model?

The first question refers to the problem that was explained in subsection 2.1.4.2. The current model takes both the thrust and power coefficient as an input. However, when the model is coupled to a LES, one of the degrees of freedom drops and the power coefficient can no longer be constrained. This is

not desirable, as in an industry setting, the total turbine power is generally known with decent accuracy from the turbine curve and the resulting load model should match with this value.

The second question relates to the discussion in subsection 2.3.2. It was already shown that the model can be used without any coupling for specifically homogeneous inflow conditions[72]. This suggests that if the inflow is known, the force distributions can be determined. In current literature, the inflow conditions are determined by providing a two-way coupling between the ABFM and the LES[49]. However, the inflow might just as well be estimated from a LES using a uniform AD model. This way, the LES framework does not need to be altered and the ABFM can be run as a cheap post-processing step after the LES is complete to obtain the force distributions. More importantly, the ABFM does not influence the LES results. This is important in a business case, since the ABFM can then be used as an add-on to an already existing product.

Still, if the force distributions are known, they can be used as an input for the LES force projection. This alters how momentum is extracted from the flow at the rotor and will therefore influence the complete simulation. The third sub question is then used to investigate the effect this has on the wake characteristics and if it is possible to significantly increase the accuracy of the resolved wake in this way.

2.4.2. Hypothesis

To aid in answering the research question, the following hypotheses are defined:

1. It is possible to keep the power coefficient as a model input when coupling the ABFM to the LES by letting go of the 1D approximation for the induction.
2. Force distributions can be reconstructed with reasonable accuracy by using one-way coupling, even if the projected forces in the LES use a different distribution.
3. Wake characteristics of the two-way coupled approach will differ significantly from those of a uniform actuator disk model in the near-wake. In the far-wake, the wakes of both models will converge to each other.

These hypotheses will now be explained in a bit more detail. For the first hypothesis, the coupling mechanism of the ABFM to the LES is questioned. As explained in subsection 2.1.4.2, the current literature couples the model to the LES by making use of a 1D approximation. This approximation constrains the induction factor and as a result the power output of the turbine. However, 1D momentum theory often does not hold in general, especially the 1D relation between power and induction, $C_P = 4\bar{a}(1 - \bar{a})^2$, does not take into account rotational losses in the wake. It is thus not optimal to constrain the induction this way. Instead, it is hypothesised that the constraint can be reversed, fixing the power of the turbine and finding the resulting induction factor that complies with this.

The second hypothesis regards the potential for a one-way coupling approach. Since the ABFM only requires the distribution of axial velocity from the disk, there is no reason that the exact force distributions have to be projected to the LES. The only requirement here is that the rotor induction is correctly accounted for by another model, which in an industry setting will likely be a uniform AD. The total thrust that is applied using the uniform AD should be the same, and as such, the induction should be captured correctly, on average. It is true that the distribution of induction depends slightly on the force distribution. However, this influence is likely only significant near the tip and root, where the loading drops to zero anyway. Self induction, however, is not the only mechanism that influences the axial disk velocity. Instead, it is also largely dependent on the turbulent eddies in the inflow. Since the self induction is still largely captured by the uniform AD, it is not unreasonable to think that the distribution of disk velocity is dominated by turbulent effects. If this is the case, then it should be possible to obtain accurate force distributions in a one-way coupling configuration.

Still, there might be a considerable added value in performing the full two-way coupling. By doing this, a significantly more realistic force distribution is provided to the LES in a feedback loop. As a result, the extraction of momentum at the rotor is better captured. It is then only logical to reason that this will increase the accuracy of the resolved wake, as stated by hypothesis three. Similar findings to this hypothesis were made by Porté-Agel et al.[54], showing that the wakes of different actuator models converge for downstream distances of 10 rotor diameter.

3

Methodology

In this thesis, the forces on a wind turbine will be determined using a coupling between an analytical model and a LES simulation. Obtaining accurate results requires careful integration of a combination of different models. All models and their coupling methods are discussed in this chapter.

First, section 3.1 will discuss the analytical body force model. This model can calculate the force distributions over the rotor for a given thrust coefficient, power coefficient, tip-speed ratio, and freestream velocity. The section will cover the derivation of the model, how it is adjusted with respect to current literature and its discretisation. Then, section 3.2 will show how the turbine operating conditions can be determined during the LES simulation. It will be shown how the characteristic turbine curves can be used for this, though additional calibration techniques are required to apply them to the LES. The chapter will end with a discussion on how the analytical model can be coupled to the LES in section 3.3. Two different coupling strategies are proposed, depending on whether a one-way or a two-way coupling is desired.

3.1. The Analytical Body Force Model

In this work, the turbine force distributions are calculated using the Analytical Body Force Model (ABFM) developed by Sørensen et al.[75]. This model has been verified for wind turbines operating at rated conditions by Sørensen and Anderson[71] and was later extended to include non-rated conditions[72]. The ABFM uses the thrust coefficient, power coefficient, tip-speed ratio, and freestream velocity to estimate the rotor induction, circulation, and the distribution of normal and tangential force, as shown in Figure 3.1.

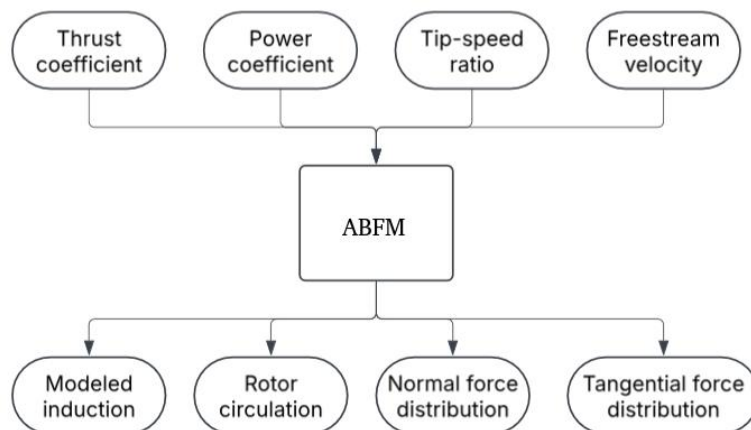


Figure 3.1: Inputs and outputs of the ABFM

The formulation of the model is provided in subsection 3.1.1. Then subsection 3.1.2 shows how the model can be solved analytically if the inflow is uniform. Next, subsection 3.1.3 discusses how azimuthal dependencies can be included. The section ends with subsection 3.1.4, which discusses how the model can be discretised, a step that is essential for coupling it to the LES later.

3.1.1. Load Model Formulation

The ABFM models the axial and tangential force at all points on the rotor disk, while radial forces are neglected. Note that this limits the use of the ABFM for cases of large rotor yaw or tilt, since these conditions are associated with large radial flows.

The axial force is obtained by finding the pressure drop over the rotor. Applying Bernoulli's principle in a cylindrical coordinate frame rotating with the rotor yields Equation 3.1. Here, U_{ax} , U_r , and Ωr represent the axial, radial, and azimuthal components of the velocity. Furthermore, u_θ is the induced swirl of the rotor, p the pressure, and ρ the density. The subscripts 1 and 2 refer to a location infinitesimally upstream and downstream of the rotor, respectively. This is also shown in an isometric view in Figure 3.2 and as a side view in Figure 3.3. In the absence of radial forces, $U_{r_1} = U_{r_2}$, so mass conservation requires $U_{ax_1} = U_{ax_2}$. Equation 3.1 then reduces to Equation 3.2, where the axial force f_{ax} is given as a force per unit area of the rotor.

$$p_1 + \frac{1}{2}\rho(U_{ax_1}^2 + U_{r_1}^2 + (\Omega r)^2) = p_2 + \frac{1}{2}\rho(U_{ax_2}^2 + U_{r_2}^2 + (\Omega r + u_\theta)^2) \quad (3.1)$$

$$f_{ax} = p_2 - p_1 = \rho u_\theta (\Omega r + \frac{1}{2}u_\theta) \quad (3.2)$$

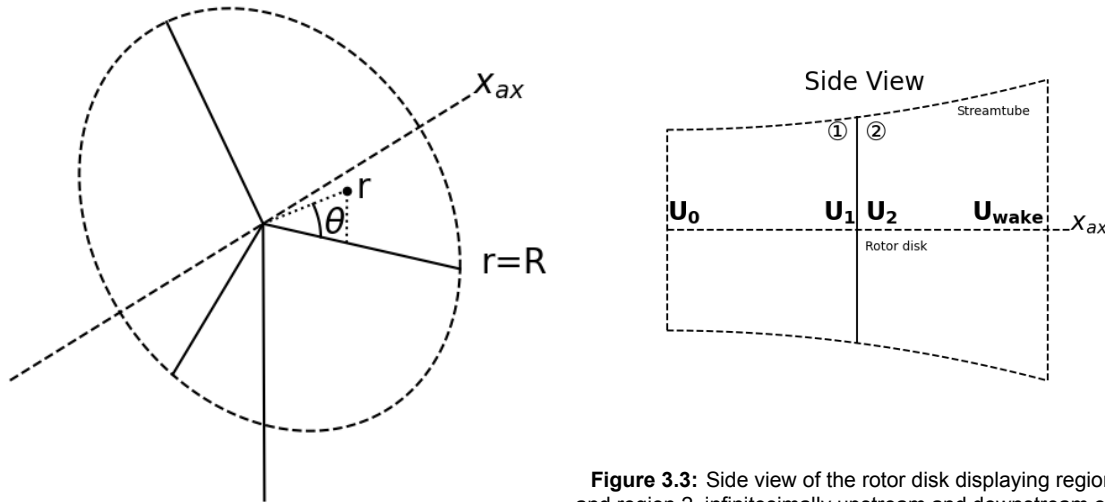


Figure 3.2: The cylindrical axis system of the ABFM

Figure 3.3: Side view of the rotor disk displaying region 1 and region 2, infinitesimally upstream and downstream of the rotor, respectively

Next, the azimuthal force is found by imposing conservation of angular momentum, as expressed by Euler's Turbine Equation in Equation 3.3[73]. After simplifying the dot product, Equation 3.3 reduces to Equation 3.4, where u_d is the axial velocity component in the rotor plane. In general, the velocity are is constant on the disk, meaning that $u_\theta = f(r, \theta)$ and $u_d = f(r, \theta)$.

$$\int_{rotor} r u_\theta \rho \mathbf{V} \cdot d\mathbf{A} = Q = \int_{rotor} r f_\theta dA \quad (3.3)$$

$$f_\theta = \rho u_\theta u_d \quad (3.4)$$

The forces are then determined by modeling the distribution of azimuthal velocity on the disk as in Equation 3.5[72]. In this equation, q_0 represents the nondimensional circulation of an optimal rotor and x is the normalized radial coordinate, such that $x = \frac{r}{R}$, where R is the rotor radius. Furthermore, S_0 is a constant, representing the solid-body rotation component of the wake. Based on an empirical fit, this parameter can be calculated from Equation 3.6[72]. $F(x, \theta)$ and $g(x)$ then refer to the tip and root correction, respectively. Several correction functions exist, which will be covered in more detail in subsection 3.1.1.1.

$$\frac{u_\theta}{U_0} = \left(\frac{q_0}{x} - S_0 x\right) F(x, \theta) g(x) \quad (3.5)$$

$$S_0 = \begin{cases} 0.08 \cdot \left(\frac{C_{T,r} - C_T}{C_{T,r}}\right)^3, & C_T < C_{T,r} \\ 0.05 \cdot \left(\frac{C_{T,r} - C_T}{C_{T,r}}\right), & C_T \geq C_{T,r} \end{cases} \quad (3.6)$$

For $S_0 = 0$, Equation 3.5 represents the induced velocity of a Joukowsky rotor, corrected for tip and root effects. The Joukowsky rotor was found to be a valid model for turbines operating at rated conditions[71]. For non-rated conditions, however, S_0 is required to correctly model the effect of turbine blade pitch on the load distribution[72].

3.1.1.1. Tip and Root Corrections

In Equation 3.5 it was shown that a tip correction $F(x, \theta)$ and a root correction $g(x)$ were added. These are necessary since the Joukowsky model assumes a constant circulation along the blade length, whereas in reality the circulation drops to zero at the root and the tip.

This need for tip and root corrections is identical to that in BEM, and known corrections can thus be adopted from literature. For the tip correction, it is suggested to use either the Prandtl correction, Equation 3.7, or the Glauert correction, Equation 3.8. Here N_b denotes the number of turbine blades. In the latter equation Φ refers to the inflow angle of the blade, which can be approximated using Equation 3.9. This approximation neglects the effect of azimuthal induction at the rotor plane on the tip correction factor. This assumption is generally safe to make, as will be demonstrated in subsection 4.1.1. Note that in general $\phi = f(x, \theta)$.

$$F_{Prandtl}(x) = \frac{2}{\pi} \arccos \left[\exp \left(-\frac{N_b}{2} \sqrt{1 + \lambda^2} \cdot (1 - x) \right) \right] \quad (3.7)$$

$$F_{Glauert}(x, \theta) = \frac{2}{\pi} \arccos \left[\exp \left(-\frac{N_b(1 - x)}{2x \sin \Phi} \right) \right] \quad (3.8)$$

$$\sin(\phi) = \frac{u_d}{V_{rel}} \approx \frac{u_d}{\sqrt{u_d^2 + (\Omega r)^2}} = \frac{1}{\sqrt{1 + \lambda^2 x^2 \left(\frac{U_0}{u_d}\right)^2}} \quad (3.9)$$

A key advantage of the Prandtl correction is that it is dependent only on the tip-speed ratio, number of blades, and radial position. As such, this correction has no azimuthal dependencies, which simplifies the model. The Glauert correction, on the other hand, is considered more accurate because it explicitly accounts for the effect of the inflow angle. Consequently, it is also the most commonly used correction for BEM[73]. Therefore, the Glauert correction will be chosen as the default for this work, unless further specified.

Different tip corrections have been proposed, as discussed by Shen et al.[63]. However, many of these formulations are not widely used or require more geometric details of the rotor. For these reasons, these corrections are not used in this work.

At the root of the blades, a correction is required for similar reasons to the tip. However, the near-hub region of the blade is generally non-lifting, which changes the physical behaviour. As recommended by Sørensen et al.[75], the root effects are therefore better described by the viscous core model of

Delery[16]. This correction is given in Equation 3.10. In this equation, a_c and b_c are model parameters, where $(a_c b_c + 1)e^{-a_c} = 1$. The values $a_c = 2.335$ and $b_c = 4$ have been selected to provide an accurate empirical fit for the induced azimuthal velocity of a turbine blade[75]. The value $\bar{\delta}$ represents the viscous core of the root vortex, which should be approximately equal to the length of the non-lifting part of the blade.

$$g(x) = 1 - \exp\left(-a_c \left(\frac{x}{\bar{\delta}}\right)^{b_c}\right) \quad (3.10)$$

3.1.2. ABFM Solution for Homogeneous Flows

For homogeneous cases, which require $u_d = \text{constant}$, $u_\theta = f(x)$, $U_0 = \text{constant}$, $\rho = \text{constant}$ and $F = f(x)$, it is found that there exists an axisymmetric solution for the forces, such that $f_{ax} = f(x)$ and $f_\theta = f(x)$. For the remainder of this work, this solution will be referred to as the ABFM-H. If the thrust coefficient (C_T), the power coefficient (C_P) and the tip-speed-ratio (λ) are known, these distributions can be found as follows.

By definition, C_T , C_P , and λ are given by Equation 3.11, Equation 3.12, and Equation 3.13. Here T is the total rotor thrust, P the total power, and Ω the rotational velocity of the blades. Alternatively, the thrust and power coefficient can also be found by integrating Equation 3.2 and Equation 3.4 over the disk, resulting in Equation 3.14 and Equation 3.15.

$$C_T = \frac{T}{\frac{1}{2}\rho_0 U_0^2 \pi R^2} \quad (3.11) \quad C_P = \frac{P}{\frac{1}{2}\rho_0 U_0^3 \pi R^2} \quad (3.12) \quad \lambda = \frac{\Omega R}{U_0} \quad (3.13)$$

$$C_T = \frac{T}{\frac{1}{2}\rho_0 U_0^2 \pi R^2} = \frac{\int_0^R \int_0^{2\pi} f_{ax} r d\theta dr}{\frac{1}{2}\rho_0 U_0^2 \pi R^2} = \frac{2\pi \rho \int_0^R r u_\theta (\Omega r + \frac{1}{2}u_\theta) dr}{\frac{1}{2}\rho_0 U_0^2 \pi R^2} = 4\lambda \int_0^1 \frac{u_\theta}{U_0} x^2 + 2 \left(\frac{u_\theta}{U_0}\right)^2 x dx \quad (3.14)$$

$$C_P = \frac{P}{\frac{1}{2}\rho_0 U_0^3 \pi R^2} = \frac{\Omega \int_0^R \int_0^{2\pi} r f_\theta r d\theta dr}{\frac{1}{2}\rho_0 U_0^3 \pi R^2} = \frac{2\pi \rho \Omega \int_0^R u_d u_\theta r^2 dr}{\frac{1}{2}\rho_0 U_0^3 \pi R^2} = 4\lambda \int_0^1 \frac{u_d}{U_0} \frac{u_\theta}{U_0} x^2 dx \quad (3.15)$$

As u_θ is known from Equation 3.5, Equation 3.14, and Equation 3.15 result in a two-equation system for the two unknowns, q_0 and u_d . These degrees of freedom can be solved for using Equation 3.16 and Equation 3.17, with the integration constants a_1 to a_5 given by Equation 3.18.

$$q_{0\text{homogeneous}} = \frac{\sqrt{(a_2 \lambda - a_3 S_0)^2 + a_1 \left(\frac{C_T}{2} + 2a_4 \lambda S_0 - a_5 S_0^2\right)} - (a_2 \lambda - a_3 S_0)}{a_1} \quad (3.16)$$

$$u_{d\text{homogeneous}} = \frac{C_P U_0}{4\lambda(a_2 q_0 - a_4 S_0)} \quad (3.17)$$

$$a_1 = \int_0^1 \frac{g^2 F^2}{x} dx, \quad a_2 = \int_0^1 g F x dx, \quad a_3 = \int_0^1 g^2 F^2 x dx, \quad a_4 = \int_0^1 g F x^3 dx, \quad a_5 = \int_0^1 g^2 f^2 x^3 dx \quad (3.18)$$

The resulting system of equations appears straightforward. In practice, however, the tip correction is often dependent on the disk velocity ($F = f(x, u_d)$). As a result, the system can become non-linear, and an iterative solver is needed to find the solution. Once q_0 and u_d are known, they can be used to calculate the resulting force distributions on the disk using Equation 3.2 and Equation 3.4. The blade loads can then be calculated from these distributions using the techniques described in subsection 3.1.5.

3.1.3. Accounting for Non-homogeneous Conditions

The solution of subsection 3.1.2 provides a valuable baseline for the model. However, the required homogeneous inflow conditions do not occur in reality due to effects such as turbulence and wind shear. As such, it is desirable for these effects to be included in the ABFM. This section will explain how several heterogeneous effects can be included in the model.

3.1.3.1. Freestream Velocity and Reference Velocity

The freestream velocity, U_0 , is often assumed to be a single value. However, wind turbines operate in the atmospheric boundary layer, which exhibits many complex flow patterns. This generates spatial variations, such as wind shear due to surface friction or turbulence which emerges from the chaotic nature of the ABL. All these turbulent effects can result in a significant variation in velocity over the rotor.

As a result, the definition of a single "freestream velocity" can become ambiguous, since each point on the rotor disk experiences slightly different conditions. This suggests that U_0 should be treated as a distribution, i.e. $U_0 = U_0(x, \theta)$. This freestream velocity can be related to the axial disk velocity using the disk-averaged axial induction factor, \bar{a} , as in Equation 3.19. Note that induction is dependent on the thrust of the rotor. For a given turbine the relation between the thrust coefficient and induction factor is generally known

$$U_0(x, \theta) = \frac{u_d(x, \theta)}{1 - \bar{a}} \quad (3.19)$$

However, the definitions of C_T , C_P , and λ require non-dimensionalisation by a single reference velocity. Following the work of Navarro Diaz et al.[49], a separate reference velocity can be defined using the induction factor and the disk-averaged axial velocity, according to Equation 3.20. This reference velocity can then be used in the definition of C_T , C_P , and λ , as done in Equation 3.21, Equation 3.22, and Equation 3.23. It should be noted that the value of \bar{a} is left as an unknown for now, in contrast to the work of Navarro Diaz et al.[49] who constrained the induction using $C_T = 4\bar{a}(1 - \bar{a})$.

$$U_{ref} = \frac{\bar{u}_d}{1 - \bar{a}} \quad (3.20)$$

$$C_T = \frac{T}{\frac{1}{2}\rho_{ref}U_{ref}^2\pi R^2} \quad (3.21) \quad C_P = \frac{P}{\frac{1}{2}\rho_{ref}U_{ref}^3\pi R^2} \quad (3.22) \quad \lambda = \frac{\Omega R}{U_{ref}} \quad (3.23)$$

Using Equation 3.20, the reference velocity can be defined in a clear and unambiguous manner, even for highly heterogeneous inflows, such as a turbine operating in the near wake of another. It can also be seen that this definition converges to the observed freestream velocity of homogeneous inflow conditions. In addition, it turns out that this reference velocity is readily available from a required calibration procedure for the LES, which is covered in more detail in subsection 3.2.2. As such, the value of U_{ref} is assumed to be known for the remainder of the section.

3.1.3.2. Density Distribution and Reference Density

Just as the freestream velocity should be treated as a distribution, a similar argument holds for air density. The density varies with altitude, and for a large turbine this difference can constitute up to 2% between the bottom and top of the rotor disk. However, if the density distribution is known, it can be accounted for in a simple manner. This is achieved by keeping the density within the integral in Equation 3.14 and Equation 3.15. Note that including these density changes is a modification introduced for this work and is not included in the original literature[72, 49].

To compute the non-dimensional coefficients, a reference density is required, which is chosen as the disk-averaged density. From a physical perspective it could be argued that this average should be weighted by the force distribution. However, this greatly increases the complexity of the calculation, while yielding minimal differences in the outcome.

3.1.3.3. LES and ABFM Disk Velocity

As established earlier, the disk velocity can be computed from Equation 3.19, provided that the freestream velocity is known. However, in the context of CFD, this process is effectively reversed, since the freestream velocity is often ambiguous, whereas the disk velocity can be directly sampled. This sampled velocity distribution is denoted by $u_{dLES}(x, \theta)$. Assuming that the reference velocity can be obtained through calibration, which will be shown in subsection 3.2.2, the induction factor is given by Equation 3.20. Consequently, the complete distribution of apparent freestream in turn follows from Equation 3.19.

If the approach presented in literature[75, 49] were followed, then the next step would involve substituting $u_{dLES}(x, \theta)$ into Equation 3.4. Since u_{dLES} is known, only one degree of freedom would remain and Equation 3.15 would have to be removed from the system of equations to ensure the model is not overconstrained.

As an alternative approach, this work distinguishes between the distributions $u_{dLES}(x, \theta)$ and $u_{dABFM}(x, \theta)$. Here, $u_{dLES}(x, \theta)$ is the disk velocity as sampled from the LES. This distribution will be used to determine the freestream velocity using Equation 3.19 and Equation 3.20. In contrast, $u_{dABFM}(x, \theta)$ represents the modeled disk velocity from the ABFM. This velocity acts as a degree of freedom of the system of equations and is used to compute the azimuthal force of Equation 3.4. Therefore, $u_{dLES}(x, \theta)$ should be interpreted as the physical disk velocity. On the other hand, $u_{dABFM}(x, \theta)$ serves as a tuning parameter to adjust the ABFM such that it matches a specified power coefficient.

This distinction is justified by the observation that, under many realistic turbine operating conditions, the ABFM fails to accurately represent the average induction. Consequently, the value of $u_{dABFM}(x, \theta)$ cannot be used to reconstruct the freestream velocity and, by extension, $u_{dLES}(x, \theta)$ cannot be used to determine the azimuthal forces. This will be further demonstrated in Appendix A.

It should be noted that if the ABFM predicts a realistic induction, $u_{dABFM} = u_{dLES}$ is a valid solution of the system of equations. Under these conditions, this new formulation will converge to the results found in literature. As will be shown in Appendix A, this is approximately the case if the turbine power adheres to 1D-momentum theory, $C_P = 4\bar{a}(1-\bar{a})^2$. However, because the power coefficient is significantly lower in practice due to wake losses, this new formulation is necessary to properly account for this.

To model the effect of heterogeneity on the tangential force distribution, it is assumed that the distribution of $u_{dLES}(x, \theta)$ and $u_{dABFM}(x, \theta)$ share the same shape. This assumption results in Equation 3.24, which allows the full distribution u_{dABFM} to be reconstructed from just the unknown mean velocity $\overline{u_{dABFM}}$, which can be represented as a single scalar.

$$u_{dABFM}(x, \theta) = \frac{u_d(x, \theta)}{\overline{u_d}} \overline{u_{dABFM}} \quad (3.24)$$

3.1.3.4. Heterogeneous system of equations

Building on the considerations of the previous sections, Equation 3.14 and Equation 3.15 can be rewritten for nonhomogeneous cases as Equation 3.25 and Equation 3.26. For a given operating condition, the parameters U_{ref} , ρ_{ref} , C_T , C_P , λ , and \bar{a} are known, as will be shown in section 3.2. Subsequently, $\frac{u_\theta}{U_0}$ is defined by Equation 3.5 and U_0 by Equation 3.19. Then, q_0 and $\overline{u_{dABFM}}$ are the two remaining unknowns of the two equations. Equation 3.25 and Equation 3.26 thus form a system of equations that can be solved for q_0 and $\overline{u_{dABFM}}$, after which the forces follow from Equation 3.2 and Equation 3.4.

$$C_{T_{heterogeneous}} = \frac{2}{\rho_{ref} U_{ref}^2 \pi R^2} \int \int_{rotor} \rho(x, \theta) \frac{u_\theta}{U_0} U_0(x, \theta) \left(\lambda U_{ref} x + \frac{1}{2} \frac{u_\theta}{U_0} U_0(x, \theta) \right) dA \quad (3.25)$$

$$C_{P_{heterogeneous}} = \frac{2\lambda}{\rho_{ref} U_{ref}^2 \pi R^2} \int \int_{rotor} x \rho(x_i, \theta_j) \frac{u_\theta}{U_0} U_0(x, \theta) \frac{u_d(x, \theta)}{\overline{u_d}} \overline{u_{dABFM}} dA \quad (3.26)$$

For the homogeneous equations, Equation 3.14 and Equation 3.15, the system was coupled, since the tip correction was generally a function of one of the degrees of freedom, i.e. $F = f(x, u_d)$. In the heterogeneous case, u_{dLES} is no longer unknown, so Equation 3.25 can be solved independently of

Equation 3.26. However, in practice, evaluation of the integrals will require numerical solutions, which will be elaborated on in the following section.

3.1.4. Load Model Discretisation

Numerical techniques will be employed to solve the system of equations of Equation 3.25 and Equation 3.26. First, the rotor disk is discretised onto a polar grid, as illustrated in Figure 3.4. The grid is constructed using an equal spacing in the azimuthal direction, since velocity gradients are on average independent on the azimuth position. Along the radial direction the points are spaced using a cosine distribution to better capture the expected sharp gradients near the tip and root. The cells are numbered using the index i along the radial direction and j along the azimuthal one. Within each cell, all quantities are assumed constant, equal to the value at the midpoint, indicated by the red dots in Figure 3.4.

When a disk-averaged quantity is required, it can be computed using the weighted average of Equation 3.27, for any quantity Q that is well defined on the disk. The subscript d indicates that the quantity is defined on the disk and the overhead bar indicates the averaging operation.

$$\overline{Q_d} = \frac{\sum_{i=1}^{N_r} \sum_{j=1}^{N_\theta} Q_{d,i,j} A_{i,j}}{\sum_{i=1}^{N_r} \sum_{j=1}^{N_\theta} A_{i,j}} \quad (3.27)$$

The integrals of Equation 3.25 and Equation 3.26 can now be approximated using discrete summations, as shown in Equation 3.28 and Equation 3.29. Here N_r and N_θ are the total amount of cells along the radial and azimuthal direction, x_i and θ_j the polar coordinates of the midpoint of cell (i, j) and A_{ij} the area of cell (i, j) .

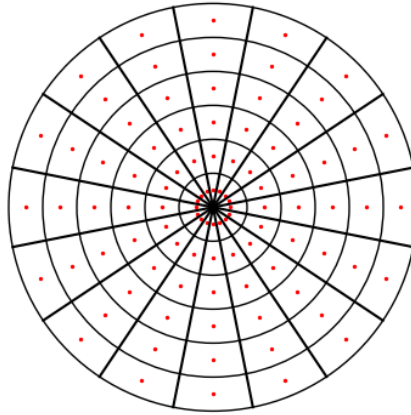


Figure 3.4: Discretisation of the rotor disk onto a polar grid. Each cell is specified using its inner and outer radius, angular span and cell midpoint

$$C_T \approx \frac{2}{\rho_{ref} U_{ref}^2 \pi R^2} \sum_{i=0}^{N_r-1} \sum_{j=0}^{N_\theta-1} \rho(x_i, \theta_j) \frac{u_\theta(x_i, \theta_j)}{U_0} U_0(x_i, \theta_j) \left(\lambda U_{ref} x_i + \frac{1}{2} \frac{u_\theta(x_i, \theta_j)}{U_0} U_0(x_i, \theta_j) \right) A_{ij} \quad (3.28)$$

$$C_P \approx \frac{2\lambda}{\rho_{ref} U_{ref}^2 \pi R^2} \sum_{i=0}^{N_r-1} \sum_{j=0}^{N_\theta-1} x_i \rho(x_i, \theta_j) \frac{u_\theta(x_i, \theta_j)}{U_0} U_0(x_i, \theta_j) \frac{u_d(x_i, \theta_j)}{u_d} \overline{u_{dABFM}} A_{ij} \quad (3.29)$$

Using Equation 3.5, it can be seen that the equation is quadratic in q_0 , such that the solution is given by Equation 3.30, with the quadratic coefficients given by Equation 3.32, Equation 3.33, and Equation 3.34. In these equations, $\dot{m}(x_i, \theta_j)$ is a mass flow term, given by Equation 3.31.

$$q_0 = \frac{-b_q + \sqrt{b_q^2 - 4a_q c_q}}{2a_q} \quad (3.30) \quad \dot{m}(x_i, \theta_j) = \rho(x_i, \theta_j) U_0(x_i, \theta_j) F(x_i, \theta_j) g(x_i) A_{ij} \quad (3.31)$$

$$a_q = \sum_{i=0}^{N_r-1} \sum_{j=0}^{N_\theta-1} \frac{\dot{m}(x_i, \theta_j) U_0(x_i, \theta_j) F(x_i, \theta_j) g(x_i)}{2x_i^2} \quad (3.32)$$

$$b_q = \sum_{i=0}^{N_r-1} \sum_{j=0}^{N_\theta-1} \dot{m}(x_i, \theta_j) (\lambda U_{ref} - U_0(x_i, \theta_j) S_0 F(x_i, \theta_j) g(x_i)) \quad (3.33)$$

$$c_q = -C_T \frac{1}{2} \rho_{ref} U_{ref}^2 \pi R^2 + \sum_{i=0}^{N_r-1} \sum_{j=0}^{N_\theta-1} \dot{m}(x_i, \theta_j) x_i^2 S_0 \left(\frac{1}{2} U_0(x_i, \theta_j) F(x_i, \theta_j) g(x_i) S_0 - \lambda U_{ref} \right) \quad (3.34)$$

Once q_0 known, Equation 3.29 can be solved directly for $\overline{u_{dABFM}}$ by observing that the equation is linear. The corresponding solution is provided in Equation 3.35. Once the system is solved, $f_{ax}(x_i, \theta_j)$ and $f_\theta(x_i, \theta_j)$ can be calculated using Equation 3.2 and Equation 3.4, remembering that in Equation 3.4, u_d refers specifically to u_{dABFM} .

$$\overline{u_{dABFM}} = \frac{C_P \frac{1}{2} \rho_{ref} U_{ref}^3 \pi R^2}{\sum_{i=0}^{N_r-1} \sum_{j=0}^{N_\theta-1} \lambda U_{ref} x_i \rho(x_i, \theta_j) \frac{u_\theta}{U_0}(x_i, \theta_j) U_0(x_i, \theta_j) \frac{u_d(x_i, \theta_j)}{u_d} A_{ij}} \quad (3.35)$$

3.1.5. Determination of Blade Loads

The load model yields the force distributions, f_{ax} and f_θ , per unit area of the rotor. However, in many cases, the quantity of interest is the force distribution along the blade. For blade loading, the force is located at N_b discrete blades, instead of spread around the rotor perimeter. A straightforward conversion is thus given by Equation 3.36 and Equation 3.37, where the factor $\frac{2\pi x R}{N_b}$ is used to calculate the contribution per blade, and $\rho_{ref} U_{ref}^2 R$ is a non-dimensionalisation factor that is commonly used for blade loads.

$$C_{ax}(x, \theta) = \frac{f_{ax}(x, \theta)}{\rho_{ref} U_{ref}^2} \frac{2\pi x}{N_b} \quad (3.36) \quad C_{az}(x, \theta) = \frac{f_\theta(x, \theta)}{\rho_{ref} U_{ref}^2} \frac{2\pi x}{N_b} \quad (3.37)$$

3.2. Turbine Operating Conditions

In section 3.1 it was seen that the ABFM can be used to determine the force distributions of the turbine blades, provided the turbine operating conditions are known. These operating conditions depend not only on the local wind conditions, but are also largely influenced by the turbine control logic. These characteristics are typically presented using the turbine thrust, power, and TSR curves.

Unfortunately, these characteristic curves are often not readily available in practice. subsection 3.2.1 will therefore discuss a simple parametrisation to approximate them. Afterwards, subsection 3.2.2 will discuss a calibration procedure to use in cases where the free-stream velocity is unknown. The section concludes with discussion of the relevant time scales and their effects in subsection 3.2.3.

3.2.1. Turbine Curve Parametrization

All wind turbines are equipped with a controller that maximises the power extraction, while preventing damage to the turbine. For each inflow velocity, the turbine controller determines its operating conditions, which are then represented by the turbine performance curves. However, for many practical applications these turbine curves are not available, in which case they can be approximated by assuming a certain control strategy.

The model adopted is described by Van der Laan et al.[32]. The turbine curve is divided into four distinct regions, as illustrated in Figure 3.5. The meaning of the different regions is summarised in Table 3.1. Virtually all turbine curves show these distinct regions, although in practice the transition between regions will not be as sudden. Instead, they might contain a blend of control strategies, which

will be neglected in this work. The resulting parametrisation is provided in Equation 3.38–Equation 3.43, where the subscript r refers to rated conditions and P_G is the generator power. The approximation for the tip-speed ratio can be further enhanced by imposing a minimum and maximum turbine RPM, if these values are available[32].

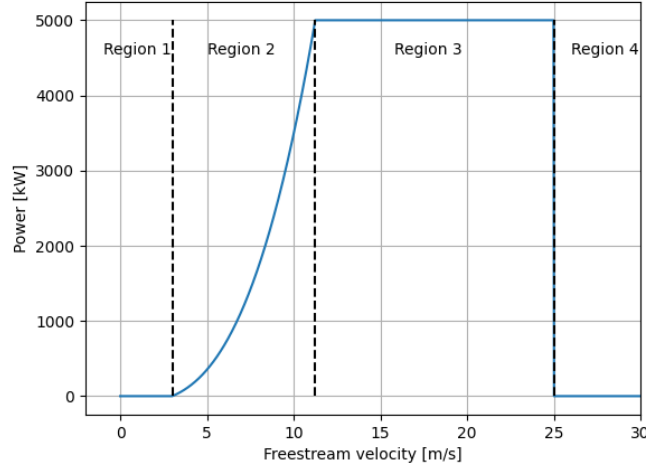


Figure 3.5: Division of a turbine power curve into four simple regions

Table 3.1: The four different control regions used for turbine curve parametrisation

| Region | Name | Description | Start Velocity | End Velocity | Thrust | Power | TSR |
|--------|---------------|---------------------------------|----------------|--------------|-----------------|-----------------|-----------------------|
| 1 | No control | No energy extraction | 0 | U_{in} | $T \approx 0$ | $P \approx 0$ | $\Omega \approx 0$ |
| 2 | TSR control | Optimise aerodynamic efficiency | U_{in} | U_r | $C_T = C_{T_r}$ | $P \propto V^3$ | $\lambda = \lambda_r$ |
| 3 | Pitch control | Maintain rated power | U_r | U_{out} | $C_T < C_{T_r}$ | $P = P_r$ | $\lambda < \lambda_r$ |
| 4 | Survival | Mitigate risk of damage | U_{out} | - | - | - | - |

$$C_T(U_0) = \begin{cases} 0 & 0 \leq U_0 < U_{in} & (\text{Region 1}) \\ C_{T_r} & U_{in} \leq U_0 < U_r & (\text{Region 2}) \\ C_{T_r} \cdot (U_0/U_r)^{-3.2} & U_r \leq U_0 \leq U_{out} & (\text{Region 3}) \end{cases} \quad (3.38)$$

$$C_P(U_0) = \begin{cases} 0 & 0 \leq U_0 < U_{in} & (\text{Region 1}) \\ \frac{2\alpha_P}{\rho\pi R^2} - \frac{2\beta_P}{\rho\pi R^2 U_0^3} & U_{in} \leq U_0 < U_r & (\text{Region 2}) \\ \frac{2P_G}{\rho\pi R^2 U_0^3} & U_r \leq U_0 \leq U_{out} & (\text{Region 3}) \end{cases} \quad (3.39)$$

$$\lambda(U_0) = \begin{cases} 0 & 0 \leq U_0 < U_{in} & (\text{Region 1}) \\ \lambda_r & U_{in} \leq U_0 < U_r & (\text{Region 2}) \\ \lambda_r \cdot (U_0/U_r)^{-1} & U_r \leq U_0 \leq U_{out} & (\text{Region 3}) \end{cases} \quad (3.40)$$

$$\alpha_P = \frac{P_G}{U_r^3 - U_{in}^3} \quad (3.41)$$

$$\beta_P = \frac{-P_G U_{in}^3}{U_r^3 - U_{in}^3} \quad (3.42)$$

$$U_r = \sqrt[3]{\frac{2P_G}{\rho\pi R^2 C_{P_r}}} \quad (3.43)$$

These equations show that the complete behaviour of the turbine is characterized only by P_G , R , U_{in} , U_r , U_{out} , C_{T_r} , C_{P_r} , and λ_r . For certain turbines, some of these parameters might still be unknown. In such cases the estimations $U_{in} \approx 3 \frac{m}{s}$, $U_{out} \approx 25 \frac{m}{s}$, $0.75 < C_{T_r} < 0.8$ and $C_{P_r} \approx 0.48$ can be used [32, 74]. In addition, the rated velocity follows from Equation 3.43. It should be noted that the parametrisation does not include region four. This is due to the large influence of the implementation of the turbine controller on the forces in this operating regime. Consequently, simulation of this regime is outside the scope of the present study.

3.2.2. Calibration of Freestream Velocity

The turbine curves are a useful tool for obtaining the turbine operating conditions, solely based on the current wind speed. However, as discussed in subsection 3.1.3, the freestream velocity can be difficult to extract from CFD data.

Instead, it is desirable to express the turbine curves in terms of a quantity that can be directly sampled within the simulation. Van der Laan et al. [33] demonstrated that the turbine curves can be reformulated in terms of the disk-averaged axial velocity. However, this method may fail in cases with a highly non-uniform inflow, since the available power scales with $\overline{\rho_d u_d^3}$, which is not equal to $\overline{\rho_d} \overline{u_d^3}$ for heterogeneous flows. Therefore, the turbine curves will be directly parametrised as a function of $\overline{\rho_d u_d^3}$. This is the same approach as is used in the ASPTurbine module of ASPIRE [85]. In practice, a time filter is often applied as well. The inclusion of this filter ensures stable numerical behaviour and physical consistency, as will be explained in more detail in subsection 3.2.3.

To express the turbine curves in terms of the average available wind power, it is assumed that they can be rewritten as Equation 3.44 and Equation 3.45. These equations are then referred to as the prime curves, where C'_T and C'_P are obtained through a calibration simulation.

$$T(\overline{\rho_d u_d^3}) = C'_T \frac{1}{2} \pi R^2 \overline{\rho_d u_d^3} \quad (3.44) \quad P(\overline{\rho_d u_d^3}) = C'_P \frac{1}{2} \pi R^2 \overline{\rho_d u_d^3} \quad (3.45)$$

This calibration is performed using a cursor-precursor setup. The cursor and precursor simulations are identical, except that the cursor includes a wind turbine implemented using an actuator model of choice. The precursor, on the other hand, does not include the turbine and therefore represent the ambient flow. The precursor simulation uses periodic boundaries along the edge of the domain. Meanwhile, the inflow of the cursor is coupled to the inflow of the precursor. As a result, the precursor represents the exact freestream that the cursor would experience.

At each time step of the simulation, the velocity at the hub height can then be extracted from the precursor simulation. As this velocity represents the freestream condition, the thrust, power, and TSR can then be retrieved from the turbine curves, which can be passed to the actuator model of the cursor to simulate the turbine.

The simulation starts at wind still and gradually increases the wind speed, allowing the turbine to experience the full range of operating conditions across its turbine curves. At each time step, the freestream velocity from the precursor, as well as the turbine thrust, turbine power, average disk velocity, and available wind power $\overline{\rho_d u_d^3}$ from the cursor are recorded.

When the simulation is finished, the resulting data points can be used to construct a lookup table, containing $\overline{\rho_d u_d^3}$, $T(\overline{\rho_d u_d^3})$, and $P(\overline{\rho_d u_d^3})$. The resulting mapping is not exactly one-to-one, due to effects of turbulence, slight temporal offsets between the cursor-precursor, and other sources of numerical noise. Instead, a regression fit is used to relate the turbine conditions to $\overline{\rho_d u_d^3}$. If desired, the look-up table can be extended to include additional variables, such as turbulence intensity, wind shear coefficient, or turbine yaw angle. However, in order to correlate these variables to the turbine operating conditions, the cursor-precursor simulation should incorporate a control sweep of these variables, which increases the computational cost significantly.

Once this lookup table has been generated, it can be used to determine the operating condition of the turbine, without the need of the precursor, by sampling $\overline{\rho_d u_d^3}$. However, it should be noted that this lookup table can be sensitive to changes in the simulation configuration. Therefore, if modifications are made to the grid spacing, numerical schemes, or turbine model, the prime curve fitting procedure

should be repeated.

3.2.3. Time Scales

The previous sections have illustrated how the turbine curves can be used to determine the turbine operating conditions during a simulation. However, there is a limitation to this method. The turbine curves inherently represent a quasi-steady state. In reality, when conditions change, both the turbine controller and the flow itself require time to adapt to the new situation and to dampen the transient responses.

As such, manufacturers often present the turbine curve as a function of the time-averaged velocity at hub height, $\langle U_{0_{hub}} \rangle_{\tau}$, where $\langle \rangle$ indicates the time-averaging operator and τ is the time scale. Accordingly, the freestream calibration of subsection 3.2.2 will thus output the turbine condition as $\langle T \rangle_{\tau}$, $\langle P \rangle_{\tau}$, $\langle \lambda \rangle_{\tau}$, and $\langle U_{ref} \rangle_{\tau}$. Similarly, the available power used to generate the look-up table should be provided as $\langle \rho_d u_d^3 \rangle_{\tau}$.

To obtain meaningful results, all velocities and forces should therefore be evaluated on the same time scale. Some quantities, such as the axial disk velocity, are explicitly available at every time step. For such cases, the time-filtered value of an arbitrary quantity Q can be determined using the exponential rolling average of Equation 3.46. This formulation remains valid for non-uniform time steps and when τ is not an exact multiple of the time step. In Equation 3.46, the averaging weight α_w is given by Equation 3.47. For clarity, the notation $\langle \rangle_{\tau}$ will not explicitly be written throughout the remainder of this work. However, it applies to all velocities and other quantities that are derived from the turbine curves.

$$\langle Q \rangle_{n+1} = \alpha_w \langle Q \rangle_n + (1 - \alpha_w) Q_{n+1} \quad (3.46) \quad \alpha_w = e^{-\frac{\Delta t}{\tau}} \quad (3.47)$$

A typical turbine curve is defined for $\tau = 600s$ [85]. Manufacturers intentionally use large time scales to average out the effects of turbulence. However, the current framework aims to specifically resolve the effect of turbulence on the force distribution over time. Therefore, the chosen time scale should be smaller than the time scale of the most influential turbulent modes of the atmosphere. For the IEA-22MW reference turbine, this corresponds to frequencies below $0.06Hz$ [15]. For this work, the IEA-15MW is concerned, which has a smaller diameter. As a result, frequencies up to $0.1Hz$ will be deemed significant, corresponding to $\tau = 10s$.

3.3. Coupling Strategies

Combining the methods of section 3.1 and section 3.2, it can be seen that the force distribution of an arbitrary turbine operating condition can be found, provided that the velocity profile over the rotor disk is known. This velocity distribution, in turn, can be found from CFD simulations, where in this work LES will be used.

The ABFM can then be coupled to the LES to calculate the load distributions at each time step. This requires a mapping from the ABFM grid onto the LES, for which the required coordinate transforms will be discussed in subsection 3.3.1. Next, subsection 3.3.2 will discuss how a one-way coupling can be implemented, in which the ABFM is run as a post-processing step on top of the LES. For increased accuracy, the ABFM results can be incorporated in a feedback loop with the LES, resulting in a two-way coupling. This is elaborated in subsection 3.3.3. The section ends with subsection 3.3.4, which describes how the LES results required for the coupling procedure can be obtained.

3.3.1. Coordinate Transformations

All LES quantities are defined in a Cartesian coordinate system $(x_{LES}, y_{LES}, z_{LES})$, with the origin located in the lower left corner of the domain. In contrast, the ABFM quantities are defined on a cylindrical grid, (x, θ, x_{ax}) , representing the non-dimensionalised radial, dimensional azimuthal, and dimensional axial direction, respectively. The origin is located at $(x, \theta, x_{ax}) = (0, \theta, 0)$. To map quantities from one frame to the other the pitch and yaw mis-alignment of the rotor with respect to the numerical grid have to be considered.

The complete coordinate transformation is described through three intermediate steps. First, the cylin-

drical coordinates will be transformed into the local Cartesian system $(x_{ax}, y_{turb}, z_{turb})$, where y_{turb} coincides with the radial direction at $\theta = 0$. The systems can be aligned by a rotation of θ along x_{ax} , as given by Equation 3.48 and Equation 3.49. In these equations, \hat{e} refers to a unit vector oriented in the direction indicated by the subscript.

$$\hat{e}_r = \cos(\theta)\hat{e}_{y_{turb}} + \sin(\theta)\hat{e}_{z_{turb}} \quad (3.48) \quad \hat{e}_\theta = -\sin(\theta)\hat{e}_{y_{turb}} + \cos(\theta)\hat{e}_{z_{turb}} \quad (3.49)$$

Next, this local Cartesian frame is rotated along the y_{turb} -axis by an angle α , the rotor tilt angle, aligning the vertical direction with the LES. This gives the new Cartesian, pitch-aligned system (x', y_{turb}, z_{LES}) , as shown in Figure 3.6. Note that for most turbines α is negative to increase tower clearance. This transformation is described by an additional rotation operation, as given in Equation 3.50 and Equation 3.51.

$$\hat{e}_{x_{ax}} = \cos(\alpha)\hat{e}_{x'} + \sin(\alpha)\hat{e}_{z_{LES}} \quad (3.50) \quad \hat{e}_{z_{turb}} = -\sin(\alpha)\hat{e}_{x'} + \cos(\alpha)\hat{e}_{z_{LES}} \quad (3.51)$$

Finally, the pitch-aligned system is transformed into the LES Cartesian system by rotating along the Z_{LES} -axis over an angle χ , as shown in Figure 3.7. Here, χ is the grid yaw angle, which is related to γ , the yaw angle with respect to the flow, via Equation 3.52. In this context, χ_{wind} is the angle between the horizontal flow direction and the LES grid. If information about the yaw controller is available, it can be used to simulate yaw misalignment effects using Equation 3.52. However, in this work it will be assumed that the controller instantly corrects for yaw, such that $\gamma = 0$. The grid yaw angle is then used to define the final coordinate transformation, as done in Equation 3.53 and Equation 3.54.

$$\chi = \chi_{wind} + \gamma = \arctan\left(\frac{v_{LES}}{u_{LES}}\right) + \gamma \quad (3.52)$$

$$\hat{e}_{x'} = \cos(\chi)\hat{e}_{x_{LES}} + \sin(\chi)\hat{e}_{y_{LES}} \quad (3.53) \quad \hat{e}_{y_{turb}} = -\sin(\chi)\hat{e}_{x_{LES}} + \cos(\chi)\hat{e}_{y_{LES}} \quad (3.54)$$

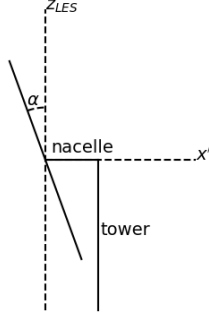


Figure 3.6: Definition of the tilt angle α of the rotor, with respect to the z-axis of the LES and the local horizontal

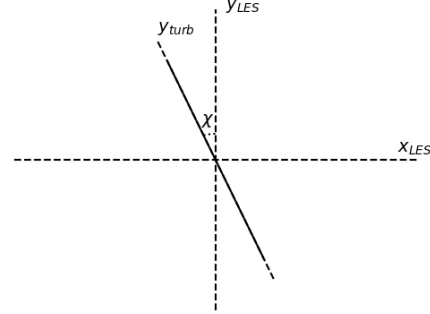


Figure 3.7: Definition of the rotor yaw misalignment angle, χ , with respect to the LES grid

Combining all transformations, the cylindrical system can be converted to the LES Cartesian system using Equation 3.55, Equation 3.56 and Equation 3.57.

$$\hat{e}_r = -(\cos(\theta)\sin(\chi) + \sin(\theta)\sin(\alpha)\cos(\chi))\hat{e}_{x_{LES}} + (\cos(\theta)\cos(\chi) - \sin(\theta)\sin(\alpha)\sin(\chi))\hat{e}_{y_{LES}} + \sin(\theta)\cos(\alpha)\hat{e}_{z_{LES}} \quad (3.55)$$

$$\hat{e}_\theta = (\sin(\theta)\sin(\chi) - \cos(\theta)\sin(\alpha)\cos(\chi))\hat{e}_{x_{LES}} - (\cos(\theta)\sin(\alpha)\sin(\chi) + \sin(\theta)\cos(\chi))\hat{e}_{y_{LES}} + \cos(\theta)\cos(\alpha)\hat{e}_{z_{LES}} \quad (3.56)$$

$$\hat{e}_{x_{ax}} = \cos(\alpha)\cos(\chi)\hat{e}_{x_{LES}} + \cos(\alpha)\sin(\chi)\hat{e}_{y_{LES}} + \sin(\alpha)\hat{e}_{z_{LES}} \quad (3.57)$$

3.3.2. One-way Coupling

The ABFM requires the LES velocity field to account for heterogeneous conditions. Similarly, the LES needs a turbine model to capture the loss of momentum at the rotor, typically represented as a set of body forces. Although these two models can be the same, this is not a strict requirement.

An advantage of using two distinct models is that a pre-existing turbine LES model can be used. The ABFM can then be used as a diagnostic or post-processing technique, to obtain the load distributions without altering the workflow of the LES. The simulation logic for this One-way Coupled Analytical Body Force Model (ABFM-1W) is visualised in Figure 3.8, where ASPTurbine is the actuator disk model built into ASPIRE. It uses a uniform Actuator Disk approach and the model obtains the turbine operating conditions in an automated manner, following a similar approach to section 3.2.

It should be noted that coupling the ABFM to a uniform Actuator Disk introduces a slight inconsistency. Specifically, the ABFM calculates the force distribution based on the rotor plane velocity distribution. However, this velocity is dependent on the self-induction of the turbine, which is governed by the shape of the force distributions. Therefore, an entirely consistent result can only be obtained if the projected forces of the LES turbine model match the distribution of the ABFM.

Nevertheless, as long as the total thrust is correct, the average induction at the rotor will be captured correctly. For Actuator Disk approaches, variations of self-induced velocity at the rotor disk might be small with respect to changes in inflow due to turbulence. For these cases, one-way coupling provides an elegant approach to investigate the impact of turbulence on the force distributions.

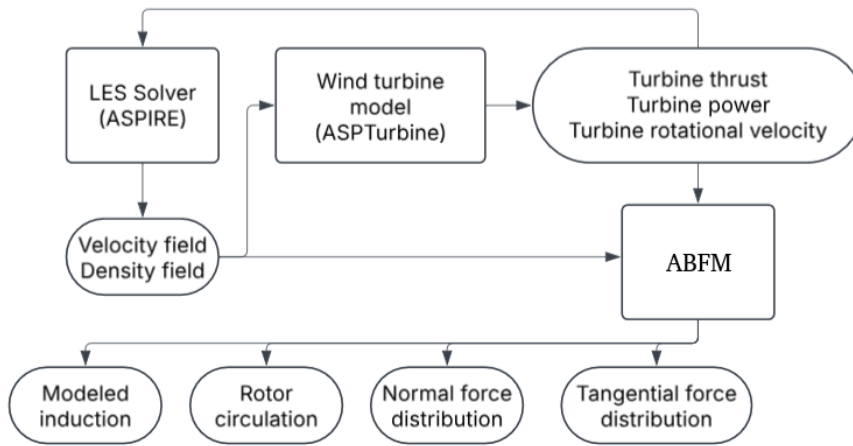


Figure 3.8: Flowchart of the ABFM-1W model used to obtain force distributions from the LES as a post-processing procedure

To implement the ABFM-1W, the distribution of axial velocity and air density over the disk must be sampled from the LES at every time step. This is done by locating the two nearest LES cell centers along each Cartesian direction, for each cell of the discretised ABFM grid. This is illustrated in Figure 3.9, where the cell centers of the ABFM grid and the LES grid are shown in red and gray, respectively. For a given cell, (i, j) , on the ABFM grid, indicated in blue, the indices (l, m, n) of the nearest cell on the LES grid along each negative Cartesian direction are identified. This cell is indicated by the green dot in Figure 3.9. The indices i and j refer to the radial and azimuthal direction of the ABFM, while l, m and n refer to the x, y and z direction of the LES, respectively. Note that, for clarity, Figure 3.9 only shows the yz -plane, the x -axis is perpendicular to the page. The value of any quantity at cell (i, j) can then be found by repeated linear interpolation along each Cartesian direction, as illustrated in Figure 3.10.

The axial velocity at the rotor disk can then be obtained by projecting the velocity vector onto the x_{ax} -axis using the dot product, as done in Equation 3.58.

$$u_{d_{ij}} = \hat{e}_{x_{ax}} \cdot \mathbf{U}_{ij} = \cos(\alpha)\cos(\chi)u_{LES_{ij}} + \cos(\alpha)\sin(\chi)v_{LES_{ij}} + \sin(\alpha)w_{LES_{ij}} \quad (3.58)$$

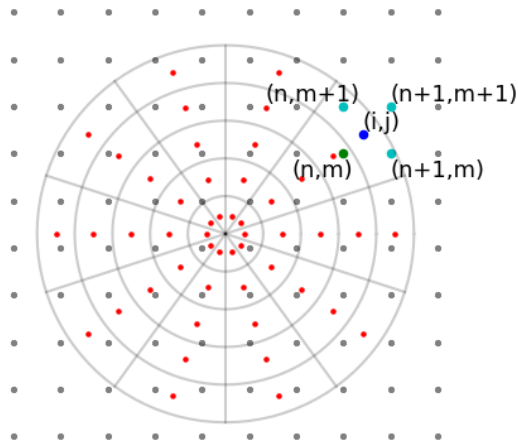


Figure 3.9: Interpolating LES results onto the ABFM grid. Gray dots represent the LES grid, red dots the ABFM grid. The blue dot is the ABFM point of interest and the green point indicates the nearest neighbour along each negative Cartesian direction. Other neighbors are indicated in cyan.

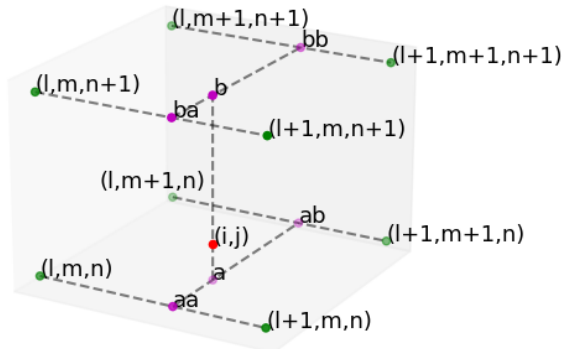


Figure 3.10: Interpolation to the (i, j) node of the ABFM grid by its 8 nearest neighbours on the LES grid. First interpolation along x gives points aa, ab, ba and bb . Then interpolation along y results in a and b . The value at (i, j) is then found by interpolating along z

3.3.3. Two-way Coupling

To fully leverage the benefits of an ABFM, the resulting force distributions should be provided to the LES in a feedback loop at every time step. This ensures that the near-wake behaviour of the LES is consistent with the rotor loading, thereby increasing the accuracy of the simulation. As a result, the LES does no longer requires a separate turbine module, since the ABFM forces are directly projected onto the grid. This results in a Two-way Coupled Analytical Body Force Model (ABFM-2W), as shown in Figure 3.11.

Comparison of Figure 3.11 and Figure 3.8 shows that removing the ASPTurbine module necessitates the implementation of two additional algorithms to maintain all functionality. Where ASPTurbine automatically derives the thrust, power and tip-speed ratio from the LES, these values instead need to be extracted from the velocity and density field. This can be done using the methodology of section 3.2. Since changing the turbine model can change the near-wake characteristics, the ABFM-1W and ABFM-2W will have a different lookup table and, as a result, the calibration simulation has to be repeated.

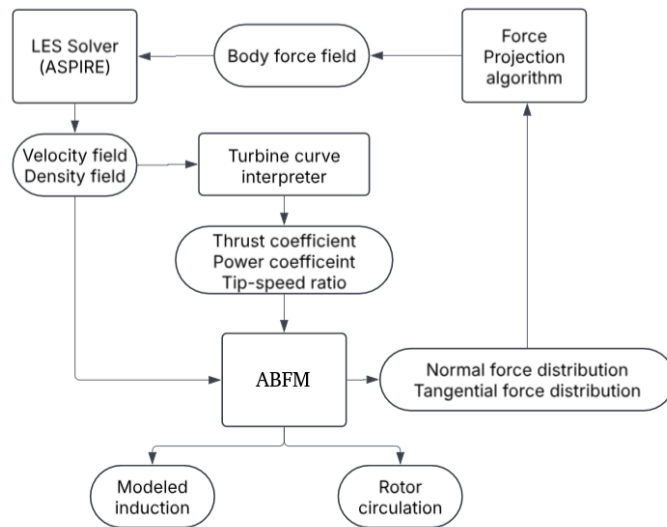


Figure 3.11: Flowchart of the ABFM-2W model to obtain turbine force distributions from the LES and project them onto the grid

The other adaptation required involves the definition of the force projection algorithm. The ABFM outputs the distribution of forces, defined at the cell centers of the polar ABFM grid. However, the turbine influence in the LES is represented as a collection of body forces for each cell in the Cartesian grid. The forces thus need to be projected from one grid onto the other.

This projection must be performed such that the forces are smeared over at least 2 LES cells[70]. This requirement is easily met in the radial and azimuthal direction, but not along the axial direction. Therefore, the 1D convolution of Equation 3.59 can be used to smear the forces away from the disk[42]. In this equation $x = \frac{r}{R}$ is the non-dimensionalised radial direction, θ the azimuthal direction, and x_{ax} the direction normal to the rotor disk. Furthermore, Δx_{ax} is the axial smearing distance and ϵ the smearing intensity. Note that the convolution simplifies to a multiplication since the force distribution is not a function of x_{ax} . A key advantage of this smearing approach is that the force is only smeared in the axial direction, preventing any force from being placed outside the rotor disk radially. This, in turn, ensures that the wake radius near the rotor plane is captured correctly.

$$f(x, \theta, x_{ax}) = f(x, \theta) \otimes \eta(x_{ax}, \epsilon) = f(x, \theta) \cdot \eta(x_{ax}, \epsilon), \quad \eta(x_{ax}, \epsilon) = \frac{1}{\epsilon\sqrt{\pi}} e^{-\frac{\Delta x_{ax}^2}{\epsilon^2}} \quad (3.59)$$

If the force distributions, $f_{ax}(x, \theta)$ and $f_{\theta}(x, \theta)$, are interpreted as a collection of point forces applied at the cell centers of the ABFM, then applying Equation 3.59 will convert them into a collection of line forces. Similarly, Equation 3.60 can be used to evaluate the smearing discretely. The denominator is required to normalise the smearing kernel, since the discrete kernel will typically no longer integrate to exact unity. The action of this discrete convolution can then be understood as transforming a single point force into a collection of point forces along a line normal to the rotor disk. If done for each cell of the ABFM grid, the result will be a collection of point forces in the cylindrical grid, as illustrated by Figure 3.12. Although the kernel of Equation 3.60 extends to $\pm\infty$, it is sufficient to clip the cylinder after a distance $\pm \frac{L_{ax}}{2}$, as shown in Figure 3.12. The normalisation in the denominator then enforces that all truncated force is proportionally redistributed over the remaining cells.

$$f(x, \theta, x_{ax}) = \frac{f(x, \theta) \cdot \eta(x_{ax}, \epsilon)}{\sum_{k=1}^{N_{x_{ax}}} \eta(x_{ax}, \epsilon)} \quad (3.60)$$

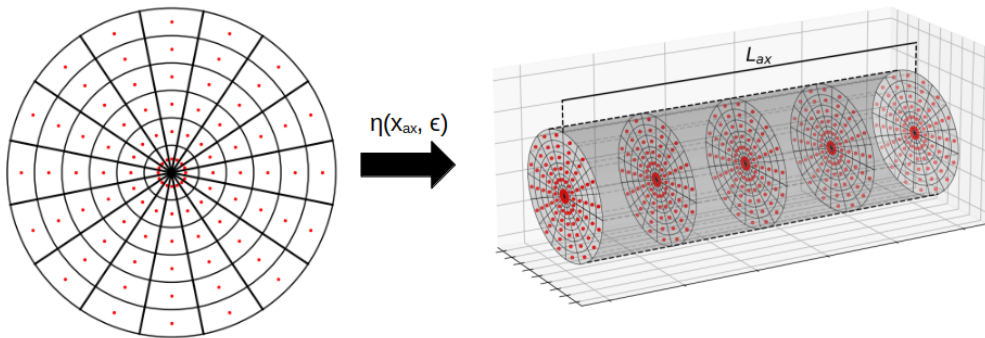


Figure 3.12: Smearing the rotor forces onto a cylinder by applying the convolution kernel $\eta(x_{ax}, \epsilon)$

The total force on each cell of the cylinder is then given by Equation 3.61. Here, k is the index of the cells along the x_{ax} direction. The minus signs are needed since the force on the air is opposite to the force on the turbine. Using the coordinate transformations of Equation 3.57 and Equation 3.56, the force can be written in Cartesian components, according to Equation 3.62. Here, the subscript i, j, k denotes evaluation at the cylindrical grid point defined by radial index i , azimuthal index j , and axial index k .

$$\mathbf{F}(x_i, \theta_j, x_{ax_k}) = -f_{ax}(x_i, \theta_j, x_{ax_k})\hat{e}_{x_{ax}}A_{ij} - f_{\theta}(x_i, \theta_j, x_{ax_k})A_{ij}\hat{e}_{\theta} \quad (3.61)$$

$$\mathbf{F}_{i,j,k} = -A_{ij} \left(f_{ax_{i,j,k}} \begin{bmatrix} \cos(\alpha)\cos(\chi) \\ \cos(\alpha)\sin(\chi) \\ \sin(\alpha) \end{bmatrix} + f_{\theta_{i,j,k}} \begin{bmatrix} \sin(\theta_j)\sin(\chi) - \cos(\theta_j)\sin(\alpha)\cos(\chi) \\ -\cos(\theta_j)\sin(\alpha)\sin(\chi) - \sin(\theta_j)\cos(\chi) \\ \cos(\theta_j)\cos(\alpha) \end{bmatrix} \right) \quad (3.62)$$

The forces are then given in Cartesian coordinates for each cell of the cylindrical grid. These cell centers, however, do not align with the cell centers of the LES itself. Therefore, to complete the projection, the forces have to be interpolated from one grid to the other, which can be done using trilinear distribution[79]. This method spreads the force of each cylindrical cell over its eight nearest neighbours in the LES grid, essentially performing the trilinear interpolation of Figure 3.9 and Figure 3.10 in reverse.

The fraction of the force distributed to each cell is calculated from Equation 3.63-Equation 3.70, where l , m and n are the indices of the closest neighbour in the negative x_{LES} , negative y_{LES} , and negative z_{LES} direction, respectively, as was demonstrated in Figure 3.9. The notation $\mathbf{F}_{i,j,k \rightarrow l,m,n}$ indicates the force which is spread from the cylindrical grid cell $(x_i, \theta_j, x_{ax_k})$ to the LES cell $(x_{LES_l}, y_{LES_m}, z_{LES_n})$. The scaling coefficients, α and β , refer to the 1-dimensional interpolation weights, which are calculated according to Equation 3.71-Equation 3.76. Since the method is linear in each direction, both the total force and the total moment are conserved after the load is distributed over the eight points.

$$\mathbf{F}_{i,j,k \rightarrow l,m,n} = \mathbf{F}_{i,j,k}\alpha_l\alpha_m\alpha_n \quad (3.63) \quad \mathbf{F}_{i,j,k \rightarrow l,m,n+1} = \mathbf{F}_{ijk}\alpha_l\alpha_m\beta_n \quad (3.67)$$

$$\mathbf{F}_{i,j,k \rightarrow l+1,m,n} = \mathbf{F}_{ijk}\beta_l\alpha_m\alpha_n \quad (3.64) \quad \mathbf{F}_{i,j,k \rightarrow l+1,m,n+1} = \mathbf{F}_{ijk}\beta_l\alpha_m\beta_n \quad (3.68)$$

$$\mathbf{F}_{i,j,k \rightarrow l,m+1,n} = \mathbf{F}_{ijk}\alpha_l\beta_m\alpha_n \quad (3.65) \quad \mathbf{F}_{i,j,k \rightarrow l,m+1,n+1} = \mathbf{F}_{ijk}\alpha_l\beta_m\beta_n \quad (3.69)$$

$$\mathbf{F}_{i,j,k \rightarrow l+1,m+1,n} = \mathbf{F}_{ijk}\beta_l\beta_m\alpha_n \quad (3.66) \quad \mathbf{F}_{i,j,k \rightarrow l+1,m+1,n+1} = \mathbf{F}_{ijk}\beta_l\beta_m\beta_n \quad (3.70)$$

$$\alpha_l = \frac{x_{LES_{l+1}} - x_{LES_{ijk}}}{x_{LES_{l+1}} - x_{LES_l}} \quad (3.71)$$

$$\alpha_m = \frac{y_{LES_{m+1}} - y_{LES_{ijk}}}{y_{LES_{m+1}} - y_{LES_m}} \quad (3.72)$$

$$\alpha_n = \frac{z_{LES_{n+1}} - z_{LES_{ijk}}}{z_{LES_{n+1}} - z_{LES_n}} \quad (3.73)$$

$$\beta_l = 1 - \alpha_l \quad (3.74)$$

$$\beta_m = 1 - \alpha_m \quad (3.75)$$

$$\beta_n = 1 - \alpha_n \quad (3.76)$$

To use the force spreading algorithm, the parameters ϵ , N_{ax_k} and L_{ax} should be determined. The smearing width should be kept as small as possible to preserve the physical meaning of the forces. However, for numerical stability $\Delta_{LES} < \epsilon < 4\Delta_{LES}$ is often required[42]. L_{ax} should be chosen in such a way that the force smearing is well captured close to the rotor. The effects at the tails of the kernel will not significantly alter the results, since the majority of the force is smeared to within a couple of standard deviations from the rotor. Furthermore, N_{ax_k} should be chosen such that $\frac{L_{ax}}{N_{ax_k}} \leq \Delta$, which ensures that the cylindrical grid is sufficiently refined to interpolate on the LES grid without skipping cells. A similar requirement is true for N_r and N_{θ} , but these are generally satisfied by the ABFM grid since it is significantly denser than the LES grid to accurately capture the force distributions.

For computational efficiency, it is clear that N_{ax_k} should stay as low as possible. As a result, it is also beneficial to choose ϵ and L_{ax} small, provided this does not compromise the numerical stability of the LES. For this work, the values $\epsilon = \Delta_{LES}$, $L_{ax} = 4\Delta_{LES}$ and $N_{ax_k} = 5$ are selected.

3.3.4. Numerical Setup of the LES

The ABFM-1W and ABFM-2W both require a coupling to a CFD model. The ASPIRE solver, introduced in subsection 2.2.3, will be used for the present work. To allow a fair comparison between results, as many settings as possible are kept constant between simulations. Therefore, a standard simulation setup is defined, which is outlined below.

The computational domain consists of a rectangular box with dimensions $32D \times 8D \times 8D$, see Figure 3.13. For this domain size, no interaction was observed between the domain boundary and the

remainder of the simulation, while the computational requirements were kept within an acceptable range.

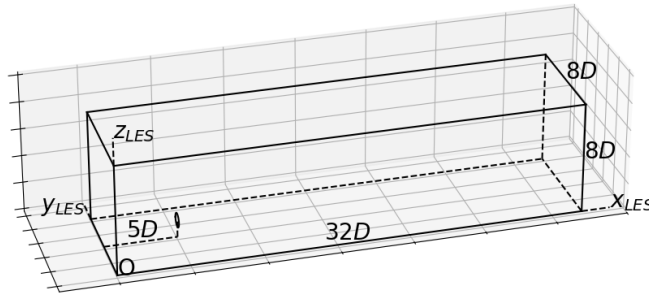


Figure 3.13: Visualisation of the computational domain for all simulations. Dimensions are given in term of the Rotor diameter

The mesh consists of a rectilinear grid with constant spacing along the x , y , and z directions. As the ABFM-1W and ABFM-2W are designed for use on industry scale, the computational requirements should be minimised, resulting in a relatively coarse grid. As such, $\Delta_{LES} = \frac{D}{8}$ is selected, since this is the minimum resolution required to accurately capture the wake behind the turbine[91]. This resolution is used throughout the whole domain, as ASPIRE's GPU-based architecture currently does not support local mesh refinements.

The boundary conditions are applied using the Numerical Weather Prediction (NWP) module of ASPIRE[85]. Although this module is typically obtains its conditions from a larger mesoscale simulation, it can also be used to directly apply a Dirichlet condition to each of the lateral boundaries of the domain. The bottom boundary is modeled as a wall, where Monin-Obukhov similarity theory is used to relate the surface fluxes to the first grid level. Additionally, a Neumann condition is imposed at the top boundary for all variables, except the w -component of the velocity. This variable is set to zero using a Dirichlet condition instead.

The large-scale boundary conditions for the sides of the domain are provided as a time series. Here, ISA sea-level conditions[29] are selected for pressure and temperature. The simulation is performed at a statistically steady wind speed, aligned with the x -axis of the LES. The wind profile along the vertical direction is free to choose and is chosen according to the goals of the specific simulation. The effect of turbulence does not have to be included in the boundary conditions, but is generated dynamically by a set of modulators. These modulators run a periodic LES around the domain boundary to generate turbulence which is consistent with local atmospheric behaviour. They then gradually nudge the simulation towards the applied boundary condition over the last few cells of the domain[85].

All turbines are modelled as a IEA-15MW Reference Turbine and are placed $5D$ downstream of the inlet and halfway through the domain laterally, as shown in Figure 3.13. Within the LES, each turbine is represented using a set of projected body forces. For the ABFM-1W these forces are automatically calculated by the ASPTurbine module, which employs a uniform AD model with a 3D-Gaussian projection kernel. The smearing length for this kernel can be chosen for each direction separately and the standard values $\epsilon_x = 2.4\Delta_{LES}$, $\epsilon_y = 2.4\Delta_{LES}$, and $\epsilon_z = \Delta_{LES}$ are used. For the ABFM-2W the force distributions obtained by the model are projected directly onto the LES grid using the methodology of subsection 3.3.3. Both models make use of the same polar grid. This grid uses $N_R = 30$ and $N_\theta = 45$, with a cosine spacing along the radial direction. A more detailed analysis on how these parameters are obtained will be given in subsection 4.3.1.

The turbine operating conditions at each simulation time step are computed using the methodology of section 3.2. The required calibration procedure is performed independently for the ABFM-1W and ABFM-2W, but can be reused across different simulations if the grid size and smearing parameters remain unchanged. The calibration also requires the turbine curves as input, for which the thrust, power, and TSR curve of Appendix B are used.

Six distinct simulation cases are defined to study the behaviour of the ABFM-1W and the ABFM-2W,

which are summarised in Table 3.2. Here, each simulation will be repeated for the ABFM-1W and ABFM-2W separately. The cases are defined by three different velocities and two different types of inflow profiles. The selected velocities are chosen to represent three distinct turbine operating conditions: below rated, near rated, and above rated velocity. The values are chosen such that the majority of the turbine curves are covered, from near to cut-in speed to close to cut-out speed.

Table 3.2: Simulation settings for the different cases

| Simulation Id | Velocity Profile | Velocity Magnitude [$\frac{m}{s}$] | Shear Coefficient [-] |
|---------------|------------------|--------------------------------------|-----------------------|
| U5 | Uniform | 5 | 0 |
| U105 | Uniform | 10.5 | 0 |
| U20 | Uniform | 20 | 0 |
| S5 | Sheared | 5 | $\frac{1}{7}$ |
| S105 | Sheared | 10.5 | $\frac{1}{7}$ |
| S20 | Sheared | 20 | $\frac{1}{7}$ |

To better understand how the ABFM-1W and ABFM-2W can resolve nonuniform inflow conditions, two different types of inflows are specified. The uniform profile is used as the base case, allowing a direct comparison with the results of the ABFM-H. The second case then represents a shear profile, where the velocity changes with height according to Equation 3.77. The velocity magnitude in this case refers to the velocity at hub height. The value of $\alpha_s = \frac{1}{7}$ is chosen, corresponding to a turbulent flow over a flat plate. Although the exact shape may be different for a realistic ABL, the 1/7 profile is a good approximation for simple terrain[7].

$$U(z) = U_{hub} \left(\frac{z}{z_{hub}} \right)^{\alpha_s} \quad (3.77)$$

The provided profiles are only specified at the inlet, but can change throughout the domain due to friction with the ground. The freestream velocity profiles at the turbine location, averaged in time, have been obtained from a separate simulation without turbines active. The resulting profiles are shown in Figure 3.14.

The sheared profile behaves as expected, while the uniform profile shows a slight deformation, resulting in a marginally smaller velocity for the lower half of the turbine. The no-slip condition can clearly be distinguished at the bottom cell of the domain, introducing a steep velocity gradient near the ground. However, the grid cells located within the rotor disk are only slightly affected. For these cells, the velocity fluctuates between 98% and 100.5% of the inlet value, resulting in an almost uniform inflow for the turbines. For both profiles, the turbulence intensity at hub height is approximately 2%.

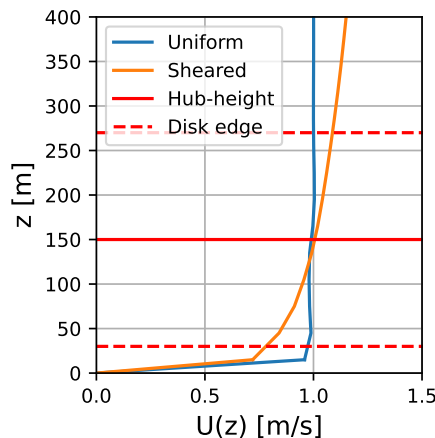


Figure 3.14: Achieved time-averaged freestream velocity profiles at the turbine location

4

Verification

In chapter 3 it was explained how the ABFM is derived and how it can be coupled to the LES simulations of wind farms using both a one-way and two-way coupling procedure. To ensure a proper implementation and to assess the validity of the models, this chapter will present a detailed verification procedure. This will include evaluating key assumptions and analysing how the model performs for simple cases.

The chapter is structured as follows. First, section 4.1 will demonstrate that the implementation of ABFM-H can reproduce results presented in literature. The ABFM-H then serves as a baseline, which will be compared with the ABFM-1W in section 4.2 and the ABFM-2W in section 4.3.

4.1. Implementation of the ABFM

In section 3.1 it was shown that assuming both the inflow and disk velocity to be homogeneous results in the system of equations of the ABFM-H, given by Equation 3.14 and Equation 3.15. The ABFM-1W and ABFM-2W are formulated as extensions of this model. Conducting an elaborate verification of the ABFM-H thus builds a solid foundation for validating the more complex coupled models.

This procedure is structured as follows. The effects of the chosen tip correction are evaluated in subsection 4.1.1. Then, subsection 4.1.2 verifies whether the nondimensional distributions of $\frac{u_d}{U_0}$ and q_0 are correctly reproduced. To assess the capabilities of the ABFM-H, its solutions are compared with those of BEM in subsection 4.1.3. Extending the ABFM-H to the ABFM-1W and ABFM-2W requires a discretised formulation. Therefore, the section ends with an assessment of the discretisation requirements in subsection 4.1.4.

4.1.1. Evaluating the Tip Correction

In subsection 3.1.1.1 it was seen that several different tip corrections exist. For this work, the Glauert correction of Equation 3.8 was selected. To calculate the correction, the inflow angle ϕ is required. An approximate value of ϕ can be obtained from Equation 3.9, which neglects the azimuthal induction of the blade.

It will now be assessed whether this assumption is valid. Noting that the azimuthal velocity in the rotor plane is half the value in the wake[72], the exact formula for the inflow angle can be obtained from the geometry of Figure 2.1 and is given in Equation 4.1.

$$\sin(\phi) = \frac{u_d}{V_{rel}} = \frac{u_d}{\sqrt{u_d^2 + (\Omega r + \frac{1}{2}u_\theta)^2}} \quad (4.1)$$

In this case, the inflow angle is directly affected by the azimuthal velocity. As a result, the right-hand side of Equation 4.1 will depend on the tip correction itself, as can be seen by substituting Equation 3.5 into Equation 4.1. This means that when azimuthal induction is included, Equation 3.8 becomes implicit

and dependent on q_0 . As such, the outcomes of the ABFM-H and the shape of the tip correction function cannot be determined independently.

However, an iterative solver can be employed to find a solution that satisfies both the ABFM and Equation 4.1, if the thrust coefficient and the tip-speed ratio are known. For a range of cases, the resulting tip correction is shown in Figure 4.1. Here, the blue and orange lines indicate the Glauert correction, computed using Equation 3.9 and Equation 4.1, respectively, while the green line shows the Prandtl correction.

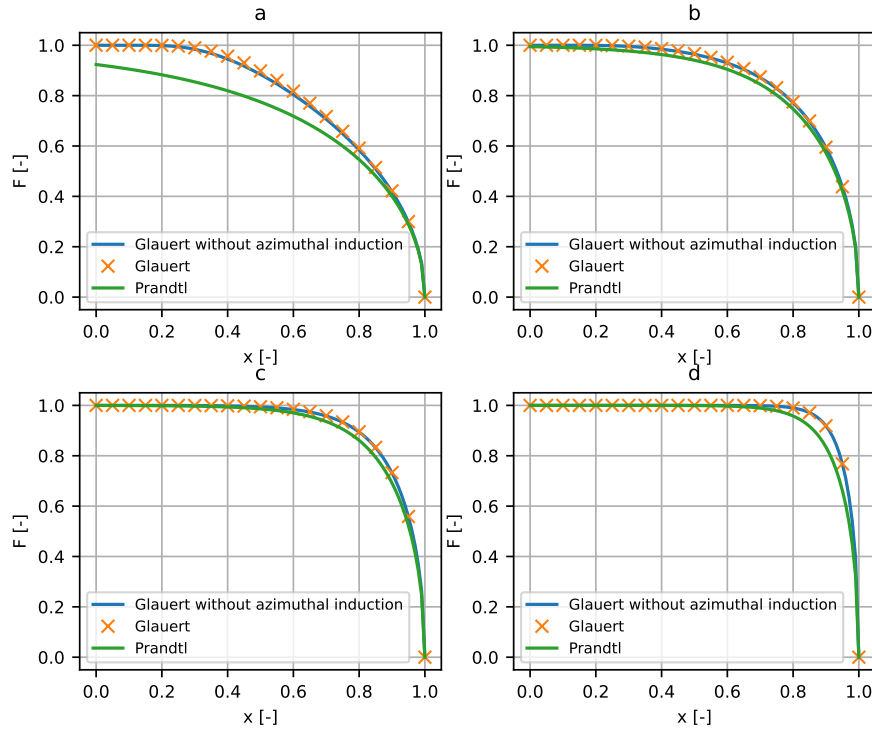


Figure 4.1: Comparison of different tip corrections for a variety of cases. Blue: The Glauert tip correction of Equation 3.8 calculated using Equation 3.9. Orange: The Glauert tip correction of Equation 3.8 calculated using Equation 4.1. Green: The Prandtl tip correction of Equation 3.7. Case a: $C_T = 0.3$, $\lambda = 1$. Case b: $C_T = 0.3$, $\lambda = 3$. Case c: $C_T = 0.5$, $\lambda = 5$. Case d: $C_T = 0.9$, $\lambda = 9$

For the cases considered, the blue and orange lines are almost identical, indicating that the influence of azimuthal induction on the tip correction is negligible. A visible difference only appears when both C_T and λ are very low, but even in this case, the impact of neglecting the azimuthal induction remains small. This is expected, since the value of the tip correction only deviates significantly from unity close to the tip. In this region, the blade velocity Ωr is very large. On the other hand, u_θ generally reaches its maximum near $\bar{\delta}$, which typically lies between 10% and 20% of the blade span.

It should be noted that Figure 4.1 was obtained for axisymmetric cases. More generally, in non-axisymmetric cases azimuthal variations can lead to increased uncertainties. This is particularly relevant for more complex flow cases, such as yaw. Regardless, the tip correction will always be an approximation. Both the Prandtl and Glauert corrections are successfully used in practice[73, 46], even though Figure 4.1 shows that they can yield somewhat different results. This illustrates that, although a tip correction is required, its exact implementation is of secondary importance. Since the Glauert correction is the most widely used[73], it is adopted for this work. However, since the implicit formulation is impractical, the formulation using Equation 3.9 will be used.

4.1.2. Verification of Non-dimensional distributions

As explained in section 3.1, the ABFM computes force distributions based on the imposed azimuthal velocity profile of Equation 3.5. In non-dimensional form, these distributions depend only on a few

model parameters and are completely decoupled from the turbine geometry. The distributions reported in literature[75] can therefore be used directly for verification.

To allow for a fair comparison, this section will use the same model parameters as those used in the reference. These correspond to $a_c = 1.256$, $b_c = 2$, $\bar{\delta} = 0.1$, $S_0 = 0$, and the use of Equation 3.7 for the tip correction. Note that these values differ from the values defined in section 3.1 and are thus used only for this section, the remainder of this work will use the standard values of section 3.1. A useful consequence of using Equation 3.7 instead of Equation 3.8 is that u_d and q_0 become decoupled. As a result, the azimuthal velocity distribution becomes independent of C_P , which simplifies the verification process.

For a given thrust coefficient and tip-speed ratio, the ABFM-H can now be used to solve for the induced azimuthal velocity profile. These distributions are presented in Figure 4.2 and Figure 4.3, for low and high values of C_T , respectively. In addition, the rotor circulation is shown in Figure 4.4. As these distributions are independent of turbine geometry, a one-to-one match with the literature is achieved.

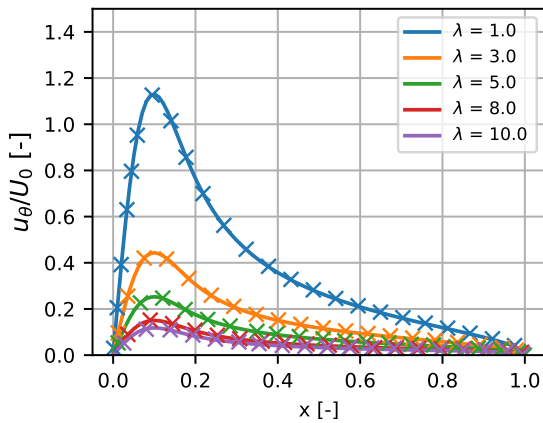


Figure 4.2: Non-dimensional azimuthal velocity distribution at $C_T = 0.3$, values from literature[75] indicated by crosses

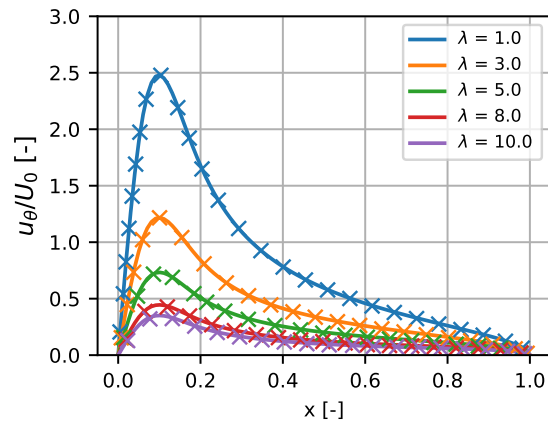


Figure 4.3: Non-dimensional azimuthal velocity distribution at $C_T = 0.9$, values from literature[75] indicated by crosses

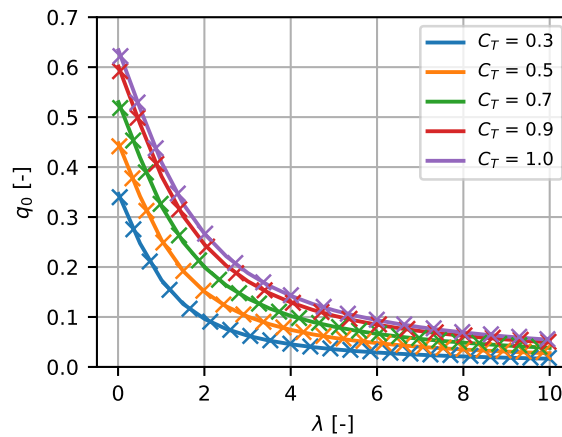


Figure 4.4: Non-dimensional rotor circulation for different thrust coefficients and tip-speed ratios, values from literature[75] indicated by crosses

4.1.3. Comparison of ABFM-H and BEM

To assess the capabilities of the ABFM-H, the force distributions of the IEA-15MW reference turbine are evaluated. This is done for the three velocities listed in Table 3.2, $5 \frac{m}{s}$, $10.5 \frac{m}{s}$, and $20 \frac{m}{s}$. These values correspond to below-rated, near-rated and above-rated wind speed conditions, respectively.

For each wind speed, the accompanying thrust coefficient, power coefficient, and tip-speed ratio are obtained using OpenFAST. These values are shown in Table 4.1. An overview of the BEM model that is used and its settings can be found in Appendix B. The solution of the ABFM-H can then be computed, after which the blade load distributions are obtained from Equation 3.36 and Equation 3.37.

Table 4.1: Operating conditions for the IEA-15MW reference turbine at low, rated and high velocity. The complete turbine curves are provided in Appendix B

| U_0 | Description | C_T | C_P | λ |
|-------|--------------------------------|--------|--------|-----------|
| 5 | Slightly above cut-in velocity | 0.791 | 0.478 | 9.158 |
| 10.5 | Near rated velocity | 0.711 | 0.468 | 9.158 |
| 20 | Close to cut-out velocity | 0.0814 | 0.0677 | 4.808 |

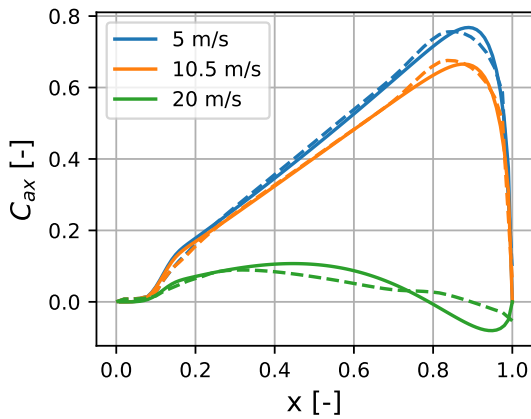


Figure 4.5: Axial force coefficient for an IEA-15MW reference turbine operating at $5 \frac{m}{s}$, $10.5 \frac{m}{s}$ and $20 \frac{m}{s}$. Solid lines: ABFM-H, dashed lines: BEM

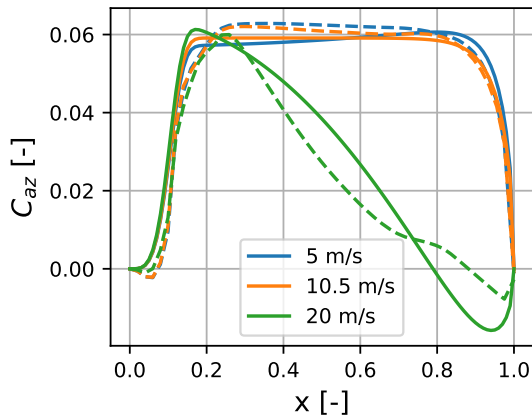


Figure 4.6: Azimuthal force coefficient for an IEA-15MW reference turbine operating at $5 \frac{m}{s}$, $10.5 \frac{m}{s}$ and $20 \frac{m}{s}$. Solid lines: ABFM-H, dashed lines: BEM

These distributions are shown in Figure 4.5 and Figure 4.6 for the axial and azimuthal force coefficients, respectively. As expected, the ABFM accurately resolves the distributions at $10.5 \frac{m}{s}$, which is the rated operating condition. At $5 \frac{m}{s}$, BEM predicts a slightly higher axial force coefficient, which is correctly captured by the ABFM. The fit for the azimuthal force coefficient is slightly worse for $5 \frac{m}{s}$, but still satisfactory.

At $20 \frac{m}{s}$, the ABFM-H deviates significantly from BEM. This is to be expected, as in this case the turbine is operating far from its design point. As a result, the circulation is no longer constant along the blade span and the ABFM solution depends heavily on the parameter S_0 , which is obtained from a regression fit[72].

Still, the results are somewhat reasonable. For both coefficients, the maximum values are predicted with acceptable accuracy and the distributions for the inboard section of the blades are captured well. However, when the loads start to decrease, the ABFM-H fails to accurately represent the remainder of the distribution. It is noteworthy that both models predict the force coefficients to become negative near the blade tip, causing the turbine to locally behave as a propeller. This phenomenon further complicates the flow physics, making it even more impressive that the ABFM manages to capture some of these complex flow features without any knowledge of the geometry of the turbine.

4.1.4. Numerical Errors of the Discretized ABFM

To couple the ABFM with a LES, the discretised formulation of Equation 3.28 and Equation 3.29 must be used. These are evaluated on a polar grid, as was shown in Figure 3.4. To ensure that the numerical errors are small, this polar grid must be sufficiently fine. On the other hand, computational efficiency favours a coarser grid. This section therefore evaluates the resolution requirements of the ABFM.

These requirements are found by evaluating the ABFM-H both analytically and numerically for a specific case. The selected case corresponds to the $10.5 \frac{m}{s}$ scenario of Table 4.1. The analytically obtained solution was already presented in subsection 4.1.3 and corresponds to a disk velocity of $u_d = 7.0 \frac{m}{s}$.

However, in the discretised formulation of the model, described in subsection 3.1.4, $u_d(x, \theta)$ is a required input. Hence, if $u_d(x, \theta) = 7.0 \frac{m}{s}$ and $\rho(x, \theta) = constant$, the discretised ABFM should reproduce the homogeneous results. In this way, the numerical errors can be evaluated without requiring a coupling to the LES. It should be noted that azimuthal influences only affect the ABFM through the distributions of $u_d(x, \theta)$ and $\rho(x, \theta)$, which are homogeneous. As such, this approach cannot be used to assess the azimuthal grid requirements.

Nevertheless, the required mesh density in the radial direction can be evaluated. To this end, the discretised ABFM is evaluated using $N_R = 10$, $N_R = 30$ and $N_R = 90$. In addition, both linear spacing and cosine spacing along the radial direction are tested. The results are listed in Table 4.2. It can be seen that the results converge well, even at relatively low resolutions. Overall, the cosine distribution performs slightly better, which is expected as it better captures the gradients near the tip and root of the blades. This trend is further confirmed by comparing the results for the azimuthal loading coefficient in Figure 4.7. In this figure, it can clearly be seen that the results converge to the analytical solution for higher mesh resolutions.

Table 4.2: Convergence of the degrees of freedom of the discretised ABFM for a uniform inflow at $10.5 \frac{m}{s}$

| N_r | Distribution type | $q_0 [-]$ | Relative error [%] | $\overline{u_{d_{ABFM}}} [\frac{m}{s}]$ | Relative error [%] |
|-------|-------------------|-----------|--------------------|---|--------------------|
| - | Analytical | 0.04158 | - | 6.9697 | - |
| 90 | Cosine | 0.04158 | 0.000 | 6.9697 | 0.000 |
| 30 | Cosine | 0.04155 | -0.08 | 6.9697 | 0.000 |
| 10 | Cosine | 0.04125 | -0.8 | 6.9717 | 0.03 |
| 90 | Linear | 0.04156 | -0.06 | 6.9696 | -0.001 |
| 30 | Linear | 0.04146 | -0.3 | 6.9693 | -0.006 |
| 10 | Linear | 0.04093 | -1.6 | 6.9697 | -0.001 |

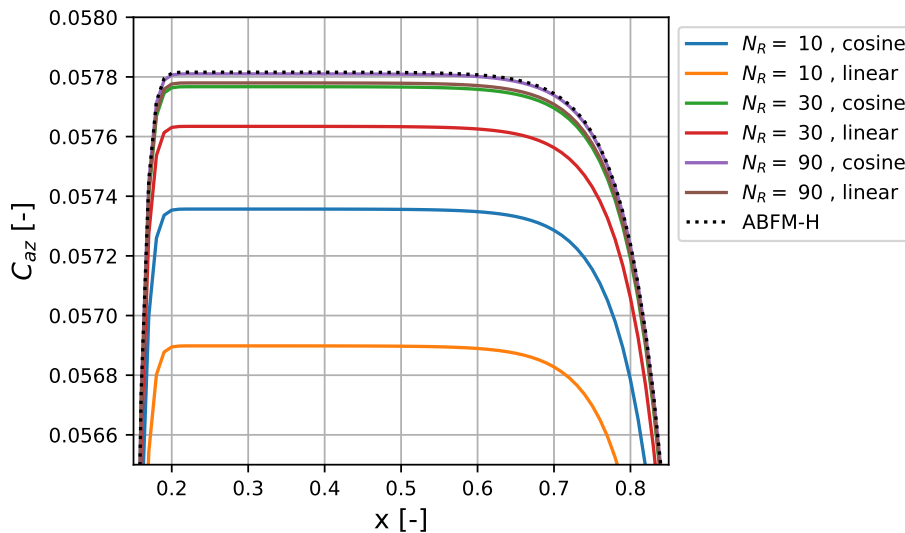


Figure 4.7: Convergence of the azimuthal force coefficient of the discretised ABFM for a uniform inflow at $10.5 \frac{m}{s}$, as compared to the ABFM-H

Based on these results, a cosine-spaced mesh with $N_r = 10$ is already sufficient to obtain an accuracy of 99%. However, in practice, additional considerations apply. It is desirable for the ABFM mesh to be denser than the LES mesh, such that all turbulent structures are adequately captured in the ABFM without introducing numerical interpolation artifacts. In subsection 3.3.4, the desired LES resolution was

set to $\Delta_{LES} = \frac{R}{4}$. It follows that $N_r > 4$ is required for a linear mesh. However for a cosine-spaced distribution more nodes are required to maintain sufficient resolution across the mid-span. Therefore, $N_R = 10$ is likely too coarse in practice and $N_r = 30$ is selected instead.

A similar argument applies to the number of points along the azimuthal direction. Considering a uniform spacing along the edge of the disk, the largest perimeter of a cell on the polar grid is $l = \frac{2\pi R}{N_\theta}$. This perimeter should then be smaller than the LES grid size, such that the turbulence is correctly captured. For the targeted resolution of $\Delta_{LES} = \frac{R}{4}$ this results in $N_\theta > 25$.

In the case that the ABFM is used with two-way coupling, the polar grid is also used to project the forces onto the LES. As a result, additional projection requirements may apply, which is covered in more detail in subsection 4.3.1.

4.2. Accuracy of the ABFM-1W in Uniform Flow

Now that the base framework of the ABFM has been verified, it can be coupled to the LES using the framework of Figure 3.8 to create the ABFM-1W. The coupling here only works in a single direction and can thus be seen as a post-processing step. As such, the LES itself is not influenced by the ABFM-1W, which greatly simplifies the verification procedure.

It will now be evaluated whether the ABFM-1W can recreate the results of the ABFM-H for a uniform inflow at $U_0 = 10.5 \frac{m}{s}$. In subsection 4.2.1 it will be verified that the LES correctly reconstructs the freestream velocity, which is required to make a fair comparison between the ABFM-1W and the ABFM-H. Then, in subsection 4.2.2, the ability of the ABFM-1W to reconstruct the correct values of q_0 and $\overline{u_{d_{ABFM}}}$ will be analysed. Since the model is fed by the LES, forces are smeared and azimuthal dependencies will be resolved, if they exist. This can affect the distribution of several variables. In subsection 4.2.3 it will therefore be checked whether the disk velocity and forces behave as expected. The section will end with an evaluation of the resulting blade loads in subsection 4.2.4.

4.2.1. Obtaining the Reference Velocity

To test the implementation of the ABFM-1W, the U105 case of Table 3.2 will be simulated. Since the inflow velocity is nearly uniform, the solution is expected to converge towards the ABFM-H, except for numerical errors.

To ensure a fair comparison, the ABFM-1W and ABFM-H should use the same input values. As such, it is assessed if the freestream velocity is correctly reconstructed during the simulation of the ABFM-1W. As shown in Figure 3.14, the freestream distribution experienced by the turbine is slightly disturbed, experiencing a small gradient from $10.22 \frac{m}{s}$ at the bottom of the disk to $10.54 \frac{m}{s}$ near the top, with an average of $10.42 \frac{m}{s}$. On top of that, the velocity field slightly fluctuates in time, due to the turbulence that is resolved by the LES.

However, these results are obtained from Figure 3.14, which were found by simulating the domain without a turbine. At runtime, evaluation of the rotor plane velocity includes the self induction of the rotor. The reference freestream velocity must then be estimated using the calibration of subsection 3.2.2. The same calibration can be used to obtain the thrust, power, and average induction factor of the turbine at each time step of the LES.

This results in a time series for each of these variables. For the reference velocity, the statistical distribution of this time series is visualised in Figure 4.8 using a boxplot. The box represents the first and third quartiles, while the orange line shows the median. The whiskers then indicate the last data point within 1.5 times the interquartile range from the box.

From Figure 4.8 it can be seen that the median reference velocity is $10.37 \frac{m}{s}$, which is very close to the average value of $10.42 \frac{m}{s}$ found for Figure 3.14. The box around the median shows that some minor turbulence is present, which causes the reference velocity to fluctuate between $10.22 \frac{m}{s}$ and $10.54 \frac{m}{s}$. This confirms that the reconstructed reference velocity closely matches the provided input profile but also actively resolves the effects of turbulence.

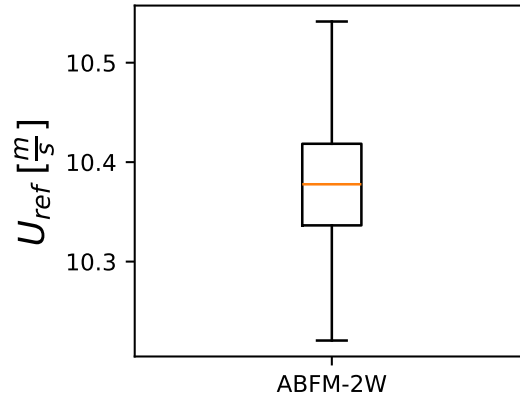


Figure 4.8: Distribution of observed reference velocity of the ABFM-1W for a uniform inflow of $10.5 \frac{m}{s}$

4.2.2. Consistency in the Degrees of Freedom

At each time step, the values of T , P , λ , and U_{ref} are computed from the freestream calibration of subsection 3.2.2. With the turbine conditions known, the ABFM-1W can be evaluated.

To obtain the forces, first the degrees of freedom of the system, q_0 and $\overline{u_{d_{ABFM}}}$, must be determined from Equation 3.30 and Equation 3.35. As the velocity changes in time, these equations should be evaluated at every time step, resulting in a time series of both quantities, i.e. $q_0 = q_0(t)$ and $\overline{u_{d_{ABFM}}} = \overline{u_{d_{ABFM}}}(t)$. The statistical distributions of these quantities in time are shown as boxplots in Figure 4.9 and Figure 4.10. Here, the ABFM-H results are constructed using the time-averaged values of C_T , C_P , λ , and U_{ref} obtained from the LES.

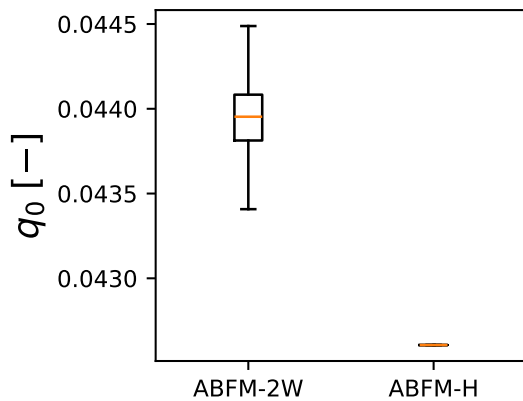


Figure 4.9: Realised rotor induction of the ABFM-1W for a uniform inflow of $10.5 \frac{m}{s}$, as compared to the ABFM-H

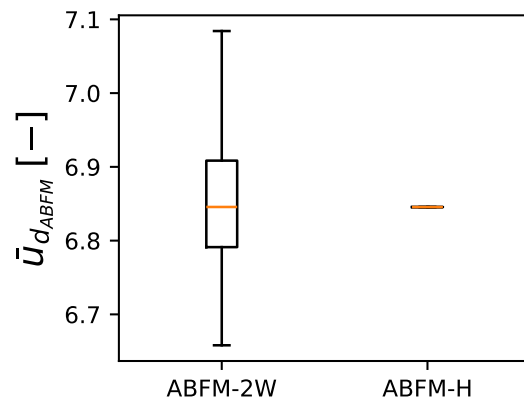


Figure 4.10: Realised ABFM disk velocity of the ABFM-1W for a uniform inflow of $10.5 \frac{m}{s}$, as compared to the ABFM-H

In Figure 4.10 it can be seen that the ABFM-1W reconstructs $\overline{u_{d_{ABFM}}}$ of the ABFM-H with high accuracy. The agreement for q_0 in Figure 4.9 is slightly worse, but still within a 5% margin of the ABFM-H results. Some differences are expected, as the ABFM-1W uses a velocity distribution obtained from the LES. This distribution includes several complex effects, such as turbulence, interference with the ground, and even turbulent wake breakdown. These effects cannot be resolved by the ABFM-H, leading to differences between the two models. Therefore, to better assess whether the differences of Figure 4.9 are plausible, the resulting force and velocity distributions should be analysed in more detail. This will be done in the following sections.

4.2.3. Evaluation of Disk Parameters

As the provided inflow to the rotor disk is almost perfectly uniform, it is expected that there are, on average, no significant azimuthal influences on the turbine. To verify this, the disk velocity distribution, which includes the effect of rotor induction, is averaged over time and shown in Figure 4.11. Several interesting observations can be made.

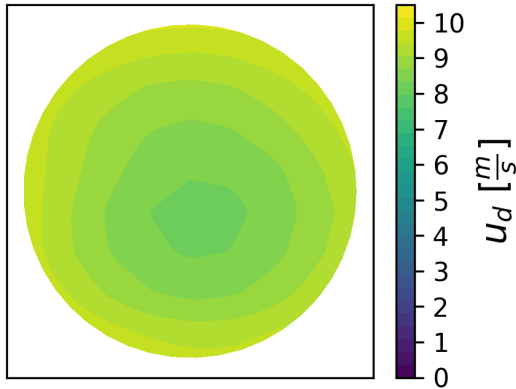


Figure 4.11: Time-averaged disk velocity of the ABFM-1W for a uniform inflow of $10.5 \frac{m}{s}$

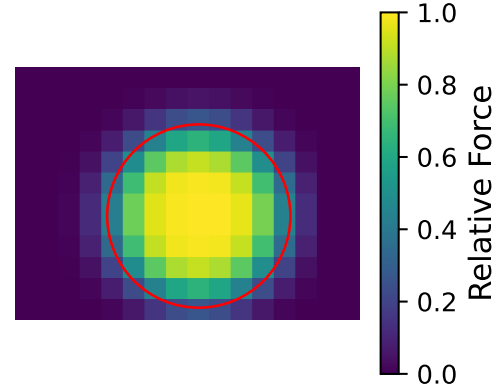


Figure 4.12: Visualisation of the force projection kernel of the ABFM-1W, the red circle indicates the edge of the rotor disk

To begin with, the flow is not completely axisymmetric. Instead, the lower part of the disk experiences a slightly reduced velocity. This, however, is consistent with the provided inflow in Figure 3.14, which also showed a mild shear in the velocity profile.

Moreover, there is a noticeable radial gradient in the velocity. The turbine is simulated using the ASP-Turbine module of ASPIRE, which employs a uniform AD model. In an ideal case, the resulting disk velocity distribution would also be uniform. However, ASPTurbine employs a 3D-Gaussian projection kernel, which causes the projected force on the grid to no longer be uniform. This can be seen in Figure 4.12, where the red line indicates the rotor disk.

It is evident that the middle of the disk carries a higher load and thus achieves a higher induction. This is an inherent consequence of the 3D-Gaussian projection method and, as a result, a truly uniform disk velocity cannot be obtained. However, since the smearing length scales with the grid resolution, the effect will be less apparent for finer grids. Alternatively, employing different smearing techniques, where no smearing is applied in radial direction, could help mitigate this effect. However, changing the smearing strategy will also affect the behaviour of the LES.

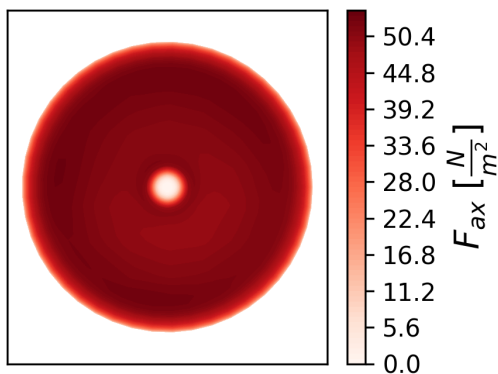


Figure 4.13: Time-averaged axial force distribution of the ABFM-1W for a uniform inflow of $10.5 \frac{m}{s}$

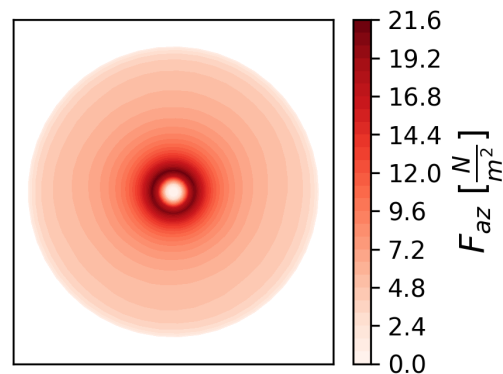


Figure 4.14: Time-averaged azimuthal force distribution of the ABFM-1W for a uniform inflow of $10.5 \frac{m}{s}$

Based on the velocity profiles, the force distributions can be calculated. These are shown in Figure 4.13 and Figure 4.14, for the axial and azimuthal force, respectively. The axial force is almost constant for a large part of the disk. Using Equation 3.36, it can be seen that this corresponds to a linear increase in the axial force coefficient along the central part of the blade, which is in line with the results from Figure 4.5. Minor azimuthal dependencies are present, consistent with the slight non-uniformity observed for the velocity in Figure 4.11.

For the azimuthal forces in Figure 4.14, the distribution is also almost axisymmetric and the force decreases in the radial direction, as expected. However, it cannot be concluded whether the distribution has the correct shape. This will be evaluated in more detail in subsection 4.2.4.

4.2.4. Evaluation of Blade Loading

To better assess the accuracy of the results shown in Figure 4.13 and Figure 4.14, these distributions will now be converted to blade loads. First, the disk loading is averaged over the azimuthal direction and then in time. Afterwards, the methodology of subsection 3.1.5 is used to find the blade load distributions.

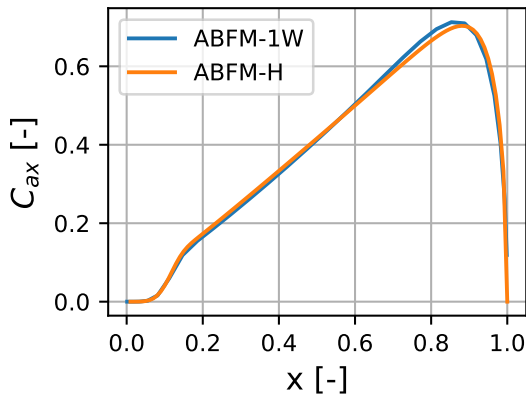


Figure 4.15: Time and azimuthally averaged axial force coefficient of the ABFM-1W for a uniform inflow of $10.5 \frac{m}{s}$, as compared to the ABFM-H

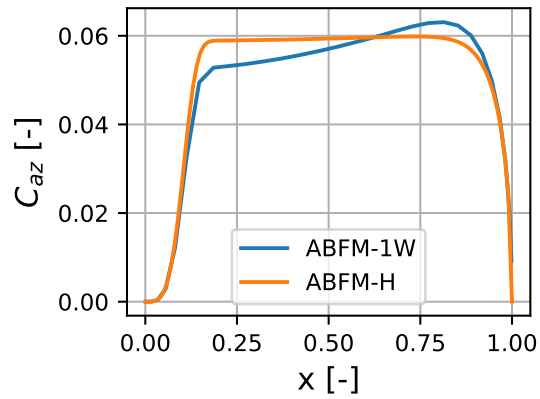


Figure 4.16: Time and azimuthally averaged azimuthal force coefficient of the ABFM-1W for a uniform inflow of $10.5 \frac{m}{s}$, as compared to the ABFM-H

The results are shown in Figure 4.15 and Figure 4.16 for the axial and azimuthal force coefficients, respectively. The time-averaged C_T , C_P , λ , and U_{ref} are also obtained from the LES and are subsequently used to construct the ABFM-H solution. Since the inflow is almost perfectly uniform, the ABFM-1W should converge to the ABFM-H, provided that turbulence is absent and that the distribution of $u_d(x, \theta)$ is properly captured in the LES.

As shown in Figure 4.15, the axial force coefficient of the ABFM-1W indeed closely follows the homogeneous prediction. Somewhat surprisingly, however, this is not the case for the azimuthal force, as can be seen in Figure 4.16. Instead of maintaining a constant value along the midsection of the blade, the ABFM-1W predicts an increasing coefficient along the span.

To understand why the ABFM-1W fails to capture the azimuthal force coefficient, even though it predicts the axial coefficient correctly, the equations for both force distributions must be evaluated. Combining Equation 3.2, Equation 3.23, and Equation 3.19, Equation 4.2 is obtained. Meanwhile, combining Equation 3.4, Equation 3.24, Equation 3.19, and Equation 3.5 yields Equation 4.3.

$$f_{ax} = \rho \frac{u_\theta}{U_0} \left(\lambda U_{ref} x + \frac{1}{2} \left(\frac{q_0}{x} - S_0 x \right) F(x, \theta) g(x) \frac{u_{dLES}(x, \theta)}{1 - \bar{a}} \right) \quad (4.2)$$

$$f_{az} = \rho \frac{u_\theta}{U_0} \left(\frac{\overline{u_{dABFM}}}{u_{dLES}} \frac{u_{dLES}(x, \theta)}{1 - \bar{a}} \right) \quad (4.3)$$

A comparison of Equation 4.2 and Equation 4.3 shows that both force distributions scale with u_{dLES} . However, this disk velocity influences the two force distributions differently. In Equation 4.3, the distribution of u_{dLES} directly influences the forces. Meanwhile, in Equation 4.2, the velocity is multiplied by the tip correction. This function goes to zero at the tip, mitigating the influence of the disk velocity in this region. In addition, from Equation 3.28 and Equation 3.29 it is seen that the axial force is constrained to the thrust coefficient, while the azimuthal force is constrained to the power. Since points at larger radial positions have a larger moment arm, the azimuthal force thus becomes more sensitive to velocity variations close to the edge of the disk.

Overall, this causes the azimuthal force to be highly sensitive to the accuracy of the disk velocity distribution. Since both the ABFM-1W and the ABFM-H in Figure 4.16 are constrained to the same power coefficient, their integrals, weighted by the radial coordinate, must be equal. As shown in Figure 4.11, u_{dLES} is overestimated at the edge of the disk for the ABFM-1W. As a result, the azimuthal forces near the tip are overestimated, causing the model to underestimate the forces in the inner blade region to meet the C_P constraint. This behaviour is consistent with the results of the ABFM-1W in Figure 4.16.

Accurately resolving u_{dLES} is therefore essential for the ABFM-1W to reliably capture the azimuthal forces. This is expected to be achievable if the force projection is performed such that the resulting projected force remains uniform and does not extend beyond the rotor disk, in contrast to the distribution shown in Figure 4.12. However, if the smearing approach is altered, this will affect the results of the LES. The main advantage of employing a one-way coupling approach in the first place was that it allowed the computation of force distributions without altering the LES results. Therefore, if smearing strategies are to be optimised to specifically improve the accuracy of the ABFM-1W, it would be more logical to employ the ABFM-2W instead.

4.3. Verification of the ABFM-2W

The ABFM-2W is designed to achieve a greater accuracy than the ABFM-1W. Not only are the forces coupled back to the LES, but there is also more freedom in implementing the force smearing algorithm. The adopted smearing strategy is tailored to resolve the disk velocity more accurately by only smearing the forces along the axial direction, as explained in subsection 3.3.3. However, this also results in a model that is significantly more complex than the ABFM-1W, as illustrated by the difference between Figure 3.8 and Figure 3.11.

Although much of the implementation of the ABFM-1W can be reused, some new elements have also been added, and a rigorous verification procedure is required to ensure a proper implementation. First, subsection 4.3.1 analyses whether the proposed smearing strategy can accurately project the forces. Then, the U105 case of Table 3.2 is simulated with the ABFM-2W, to see how accurately it performs under simple conditions. More specifically, the rotor induction and modelled average disk velocity will be evaluated in subsection 4.3.2, the disk velocity in subsection 4.3.3, and the disk and blade loads in subsection 4.3.4.

4.3.1. Equivalence of the Force Projection

In subsection 3.3.3, the new smearing approach was introduced, which smears the forces only in the axial direction. This approach was designed to minimise the projection of force outside of the rotor disk, such that the rotor induction is represented as realistically as possible.

The algorithm combines a 1D smearing approach with a trilinear interpolation to project the forces from the ABFM grid onto the LES. Since both the operations conserve force and moment around the x_{ax} -axis, the total thrust and power obtained by integrating the force distributions are unchanged after the projection. This can easily be verified. However, a correct implementation also requires that the resulting shape of the projected force distribution represents the intended loading.

This will be evaluated by applying the force projection algorithm to a uniform test loading. The projection is performed at $\Delta_{LES} = \frac{D}{8}$, corresponding to the proposed resolution of subsection 3.3.4. The rotor is assumed to have no tilt ($\alpha = 0$) and is placed normal to x_{LES} , such that $\chi = 0$. As a result, the smearing axis aligns with the x_{LES} -axis. Since only axial smearing is applied, the shape of the force distribution is constant along the x_{LES} -direction. To assess whether the projected force remains uniform in the radial and azimuthal direction, therefore only the projected force in a $y_{LES}z_{LES}$ plane through the turbine has

to be evaluated.

The ABFM grid should be defined with a higher resolution than the LES grid, to ensure that no cells are skipped when interpolating from one grid to another. As an initial attempt, a polar grid with $N_r = 30$ and $N_\theta = 60$ is selected. For the radial direction, cosine spacing is applied. As demonstrated in Figure 4.7 this reduces numerical errors with respect to a linear spacing.

The resulting force projection for a uniform test force is shown in Figure 4.17. It should be noted that the colormap is non-linear to better visualise the cell-to-cell variation in force within the uniform region, while also showing the force contribution of cells intersecting the rotor disk. It can be seen that the distribution is significantly more uniform than Figure 4.12. For all inner cells in the grid, indicated with a black dot, the force is within 2.1% of the cell with the highest load. Meanwhile, no loading is assigned to cells that are completely outside the rotor disk. Cells that intersect the rotor disk have a loading that approximately scales with the overlap area.

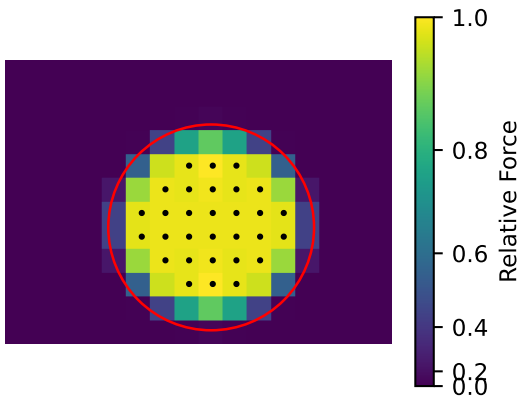


Figure 4.17: Resulting force projection of a uniform loading using the force projection algorithm of subsection 3.3.3 with $N_r = 30$, $N_\theta = 60$ and $\Delta_{LES} = \frac{D}{8}$. All cells indicated with a dot are within 2.1% of the maximal loading

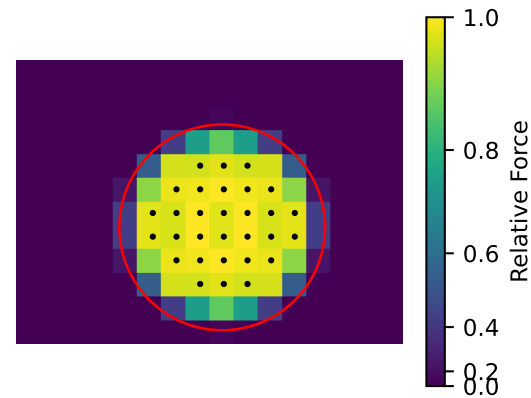


Figure 4.18: Resulting force projection of a uniform loading using the force projection algorithm of subsection 3.3.3 with $N_r = 10$, $N_\theta = 60$ and $\Delta_{LES} = \frac{D}{8}$. All cells indicated with a dot are within 3.5% of the maximal loading

An interesting observation is that the projection does not behave the same in the y and z directions. This is caused by the offset between the turbine midpoint and the cell centers of the LES grid cells. Along the y -direction, the rotor disk spans 9 cells, whereas along the z -direction it spans 10. Along the z -direction, the same loading must therefore be spread over an additional cell. This is most apparent in the topmost and bottommost cells that lie completely within the rotor disk.

Overall, the projection behaves as expected and produces satisfactory distributions. It will now be investigated whether the mesh density can be reduced without introducing errors. First, the density along the radial direction is reduced to $N_r = 10$, using a cosine spacing. The result is shown Figure 4.18 and is remarkably good, considering that the dotted cells are still within 3.5% of the maximum load. However, the cell-to-cell pattern is oscillatory, which is undesirable. As such, $N_r = 30$ will be used as a baseline.

Along the azimuthal direction, it was already established in subsection 4.1.4 that $N_\theta \geq 26$ is required to properly resolve turbulence in the ABFM. Therefore, the projection quality at $N_\theta = 30$ and $N_\theta = 45$ will now be tested. The results are shown in Figure 4.19 and Figure 4.20, respectively. At half the resolution of Figure 4.17, $N_\theta = 30$ results in only slightly higher deviations for the middle cells, up to 2.7%. However, for $N_\theta = 45$, the maximum deviation is reduced to just 0.8%, even outperforming the higher resolution case. This is likely caused by the symmetry introduced at $N_\theta = 60$, which generates small load concentrations at angles where the azimuthal grid aligns with the Cartesian grid. For $N_\theta = 45$, this symmetry breaks, causing the load to spread more uniformly. As such, $N_\theta = 45$ will be used for the remainder of this work.

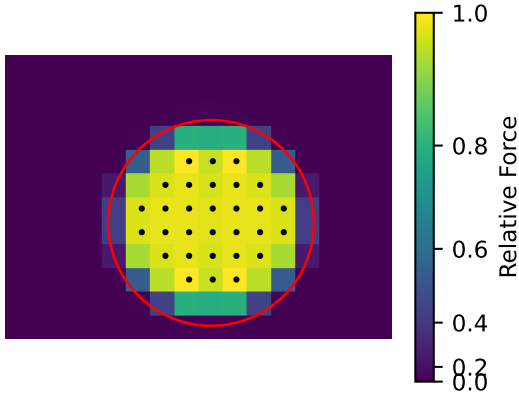


Figure 4.19: Resulting force projection of a uniform loading using the force projection algorithm of subsection 3.3.3 with $N_r = 30$, $N_\theta = 30$ and $\Delta_{LES} = \frac{D}{8}$. All cells indicated with a dot are within 2.7% of the maximal loading

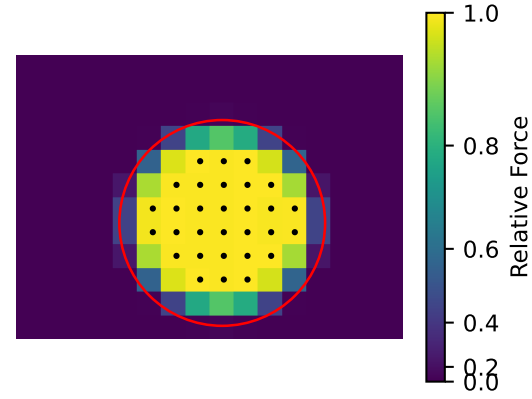


Figure 4.20: Resulting force projection of a uniform loading using the force projection algorithm of subsection 3.3.3 with $N_r = 30$, $N_\theta = 45$ and $\Delta_{LES} = \frac{D}{8}$. All cells indicated with a dot are within 0.8% of the maximal loading

This verification was carried out for a rotor disk without any tilt or yaw, such that it was perfectly aligned with the LES grid. However, when yaw or tilt is applied, the projection cylinder of Figure 3.12 rotates with respect to the LES grid. As a result, the apparent grid spacing of the LES, when viewed along the axial direction, increases due to the triangle inequality. The same number of cylindrical cells are thus projected onto a smaller number of LES cells. It is therefore expected that applying yaw or tilt to the rotor will not degrade the quality of the projection.

4.3.2. Consistency of the degrees of freedom

Now that the effectiveness of the force projection algorithm has been established, the ABFM-2W can be used to simulate the U105 case from Table 3.2. The analysis of section 4.2 will now be repeated to assess whether the ABFM-1W behaves differently than the ABFM-2W.

Since the freestream conditions remain unchanged, the average freestream profile of Figure 3.14 is obtained. However, due to the rotor self-induction, the ABFM-2W is unable to directly observe this profile. Instead, it must reconstruct the freestream conditions from its measured disk velocity, using the methodology described in subsection 3.2.2. The resulting reference velocity is shown in Figure 4.21. As found in subsection 4.2.1, the average freestream velocity of the U105 simulation is $10.42 \frac{m}{s}$. It thus follows that the reconstructed reference velocity has a slight positive bias, but is generally close to the true velocity. Compared with Figure 4.8, the ABFM-2W shows a slightly larger spread, but overall the agreement between the two models is good.

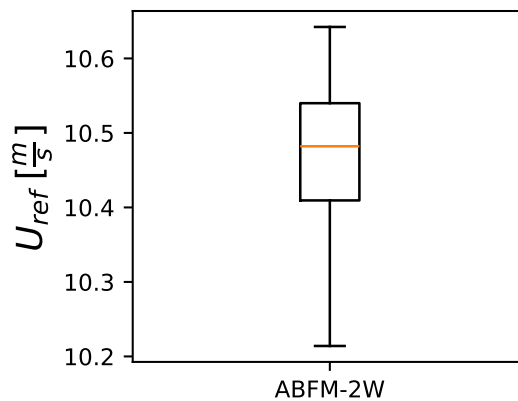


Figure 4.21: Distribution of observed reference velocity of the ABFM-2W for a uniform inflow of $10.5 \frac{m}{s}$

With the reference velocity known, the ABFM-2W can be evaluated at each time step of the simulation. The resulting distributions of q_0 and $\overline{u_{d_{ABFM}}}$ are displayed in the boxplots of Figure 4.22 and Figure 4.23, with the ABFM-H included as a reference. Since the disk velocity distribution is different than for the ABFM-1W, the resulting q_0 and $\overline{u_{d_{ABFM}}}$ are also slightly different from those provided in Figure 4.9 and Figure 4.10. However, the trends remain consistent; $u_{d_{ABFM}}$ is captured with high accuracy, while q_0 appears to be slightly higher than for the ABFM-H. The impact this has on the force distribution will be shown in the following subsections.

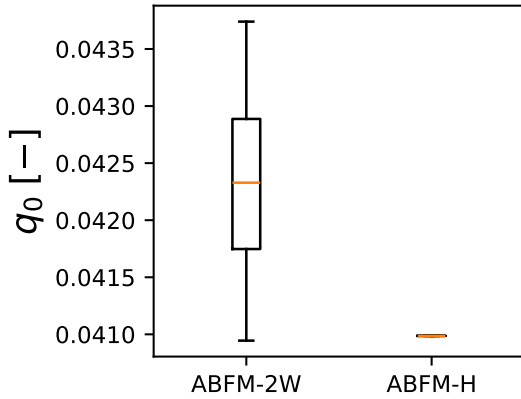


Figure 4.22: Realised rotor induction of the ABFM-2W for a uniform inflow of $10.5 \frac{m}{s}$, as compared to the ABFM-H

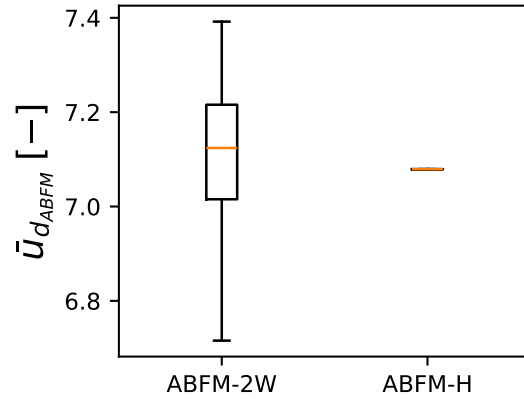


Figure 4.23: Realised ABFM disk velocity for the ABFM-2W for a uniform inflow of $10.5 \frac{m}{s}$, as compared to the ABFM-H

4.3.3. Reconstruction of the Disk Velocity

In subsection 4.2.4 it was shown that accurately resolving the disk velocity distribution is essential to correctly predict the azimuthal blade loads. For the ABFM-1W, a clear radial increase was observed in Figure 4.11, attributed to the force projection. Since the ABFM-2W applies smearing only in the axial direction, this effect is expected to disappear. It can be seen in Figure 4.24 that the distribution is indeed more uniform for a large part of the disk.

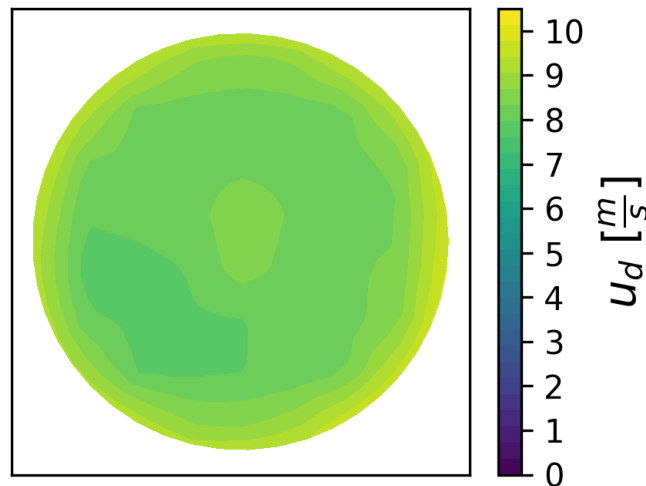


Figure 4.24: Time-averaged disk velocity of the ABFM-2W for a uniform inflow of $10.5 \frac{m}{s}$

However, near the edge of the disk, a steep gradient is still observed. Rather than resulting from smearing, this high velocity on the edge appears to be a numerical interpolation artifact. Recall that

$u_{d_{LES}}$ is obtained by trilinear interpolation from the LES grid using the eight surrounding points. For cells near the edge, it is likely that some neighbours are located outside of the rotor disk itself. From Figure 3.9 it can be seen that this is the case for the indicated blue cell and some other ABFM cells near the outer edge of the circle. More generally, if $r > R - \Delta_{LES}$, interpolation using cells outside the rotor disk is expected.

However, all cells outside of the rotor disk carry a significantly lower force and therefore experience less induction, resulting in higher velocities than for those within the rotor disk. If these high velocity cells are used for interpolation, the interpolation result will be overestimated, as is observed in Figure 4.24. However, the resulting profile is still significantly better than Figure 4.11 and it remains to be seen to what extent these edge effects influence the force distributions. This will be evaluated in subsection 4.3.4.

In case it is necessary to reduce these artifacts, there are two possible solutions. The simplest approach is to increase the cell density of the LES, as the artifacts are confined to polar cells that lie within Δ_{LES} of the edge. Alternatively, a different interpolation technique could be applied near the edge of the disk, one that samples the velocity only from cells inside the rotor disk. This would require an algorithm to determine which cells cannot be sampled, along with an extrapolation strategy that chooses the appropriate samples from inside the disk and their interpolation weights. Such an algorithm would likely depend on grid spacing and azimuthal position, making it non-trivial to implement. Therefore, this approach will not be considered further in this work.

4.3.4. Accuracy of the Force Distributions

When $u_{d_{LES}}$ is provided as input to the ABFM-2W, the disk force distributions can be computed. The time-averaged results are shown in Figure 4.25 and Figure 4.26 for the axial and azimuthal loading, respectively.

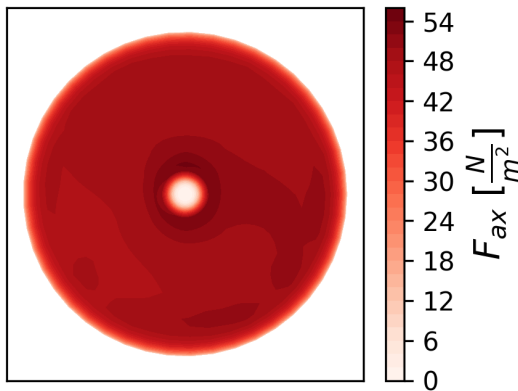


Figure 4.25: Time-averaged axial force distribution of the ABFM-2W for a uniform inflow of $10.5 \frac{m}{s}$

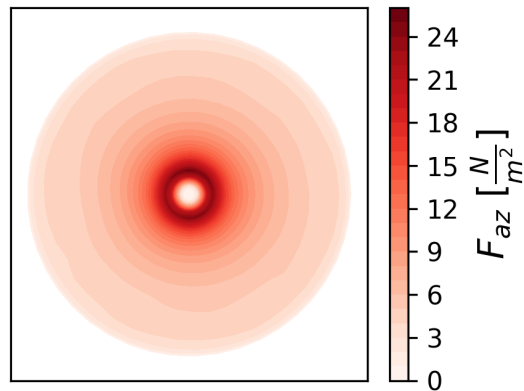


Figure 4.26: Time-averaged azimuthal force distribution of the ABFM-2W for a uniform inflow of $10.5 \frac{m}{s}$

The axial force in Figure 4.25 is relatively constant across a large portion of the disk, in line with the blade loads of Figure 4.5. Minor deviations can be observed, which correlate with regions of higher and lower velocity in Figure 4.24. These changes are likely caused by a combination of slight wind shear, see Figure 3.14, and azimuthally dependent induction resulting from wake rotation. The azimuthal forces in Figure 4.26 behave as expected. Slight azimuthal dependencies can be distinguished, these are again likely caused by small non-uniformities in the inflow.

To better assess the shape of the distributions, the forces are averaged in the azimuthal direction and subsequently converted to blade loads using Equation 3.36 and Equation 3.37. The results are displayed in Figure 4.27 and Figure 4.28. The axial force coefficient shows a near-perfect agreement, with only a slight overestimation near the tip. The azimuthal coefficient, on the other hand, still exhibits some numerical artifacts. As discussed in subsection 4.2.4, the azimuthal force is highly sensitive to the distribution of the disk velocity. As shown in Figure 4.24, the velocity is overestimated near the edge of the disk, and this effect is clearly reflected in Figure 4.28.

Because the velocity near the edge of the disk is too high, the force is overestimated in this region. Since the model is constrained to the power coefficient, the force is underestimated in the mid-section of the blade. Nonetheless, since the shape of u_d is well captured for the majority of the rotor, the azimuthal force distribution remains reasonably accurate up to the outermost LES cell on the disk, beyond which interpolation artifacts begin to dominate.

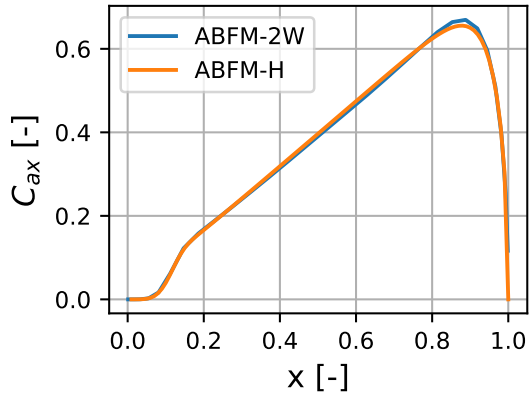


Figure 4.27: Time and azimuthally averaged axial force coefficient of the ABFM-2W for a uniform inflow of $10.5 \frac{m}{s}$

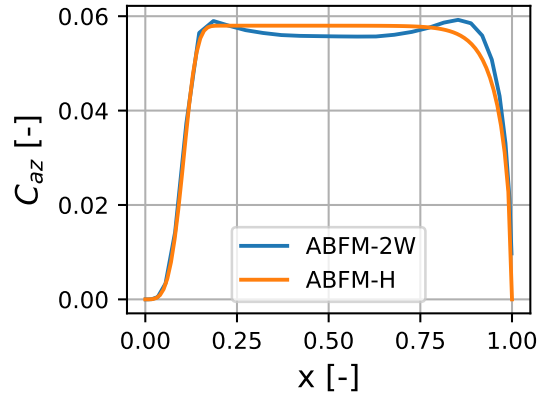


Figure 4.28: Time and azimuthally averaged azimuthal force coefficient of the ABFM-2W for a uniform inflow of $10.5 \frac{m}{s}$

Although the ABFM-2W is better at reconstructing the azimuthal force coefficient than the ABFM-1W, it is still not capable of exactly reproducing the homogeneous result. If the blade loads are the desired result of the simulation, it is valid to question whether the use of the ABFM-1W or ABFM-2W should be preferred over the simpler ABFM-H. However, it is important to realise that the current verification case was chosen specifically such that the ABFM-H could be employed.

In general, uniform inflows rarely occur in practice, as the ABL is dominated by complicated phenomena such as wind shear and turbulence. These effects can significantly alter the blade loadings experienced by the turbine but cannot be resolved by the ABFM-H. In such cases, the ABFM-1W and the ABFM-2W can still be used to provide insight into the loading behaviour, even if the results are not exact. The capability of these models to capture more complex and realistic flow cases will be investigated in chapter 5.

5

Results and Discussion

Following the verification of the ABFM-1W and ABFM-2W in chapter 4, this chapter will evaluate their performance for more complex and realistic flows. This evaluation is performed by comparing the results of both models to the BEM model of Appendix B. First, section 5.1 investigates the turbine operating conditions achieved during each simulation. Afterwards, section 5.2 analyses the resulting blade loads and compare them to BEM results. The chapter ends with a discussion about the turbine wakes. In section 5.3 the differences in wake behaviour between the ABFM-1W and ABFM-2W will be analysed, and section 5.4 will investigate what this means for a turbine that is experiencing a partially waked inflow.

5.1. Reconstruction of Turbine Operating Conditions

The ABFM-1W and ABFM-2W require total thrust and power as input parameters. Due to turbulence, these values vary slightly over time and must be determined from the freestream calibration described in section 3.2. To enable a fair comparison of the force distributions across different simulations, the total loading has to be similar. The statistical distributions in time of thrust and power will therefore be examined in subsection 5.1.1 and subsection 5.1.2, respectively.

5.1.1. Turbine Thrust

During the simulation a time series of the thrust values is collected. The statistical distributions for each simulation listed in Table 3.2 are presented as boxplots in Figure 5.1 for the uniform flows and in Figure 5.2 for the sheared flows. In these plots, the BEM reference is generated with the OpenFAST model described in Appendix B, using a steady inflow. To ensure a fair comparison, this BEM simulation is conducted at the average reference velocity of the ABFM-1W and ABFM-2W. The thrust of the ABFM-1W and ABFM-2W is obtained from the freestream calibration described in subsection 3.2.2, using the same turbine curves as the BEM simulation. As such, the ABFM-1W and ABFM-2W should predict thrust levels similar to those of BEM, the only deviations arising from turbulence and calibration errors.

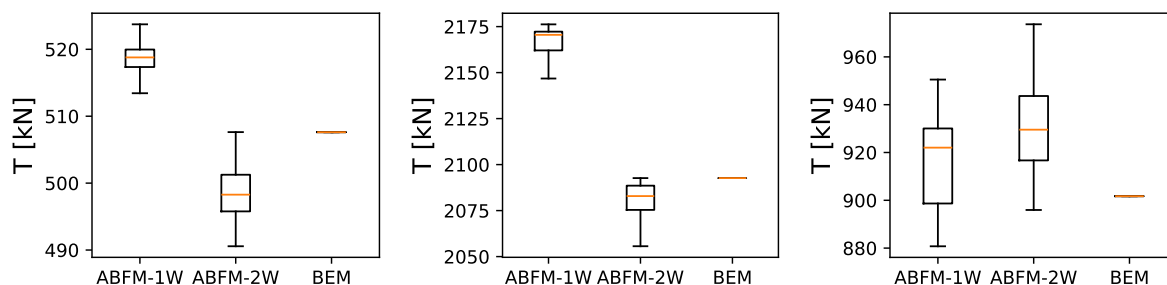


Figure 5.1: Distribution of thrust for the ABFM-1W and ABFM-2W, as compared to the BEM model of Appendix B for a uniform inflow at: $5 \frac{m}{s}$ (left), $10.5 \frac{m}{s}$ (middle) and $20 \frac{m}{s}$ (right)

For the uniform inflows shown in Figure 5.1, the ABFM-1W consistently predicts higher thrust than the BEM reference. The trend for the ABFM-2W is less consistent, although the overall difference between the median thrust compared to BEM is slightly smaller. For all three velocities the interquartile range, indicated by the box, falls within 4% of the BEM reference for both ABFM models. Given that the LES experiences turbulence and that the thrust is based solely on a calibrated correlation, this result is considered quite close. Similar trends are observed for the sheared inflows in Figure 5.2. The values of the ABFM median thrust and BEM median thrust remain close, with differences of up to approximately 6%.

It is noteworthy that, due to shear, the BEM result is no longer constant in time, even though the inflow is steady. Instead, the thrust oscillates with a frequency of $f = \frac{N_b \lambda U_{ref}}{2\pi R}$, as the turbine blades pass through regions with higher and lower velocity. However, the freestream calibration determines the thrust from the average wind power over the entire disk $\overline{\rho u_d^3}$. As such, the ABFM models do not capture this oscillation, which slightly increases the differences with respect to BEM.

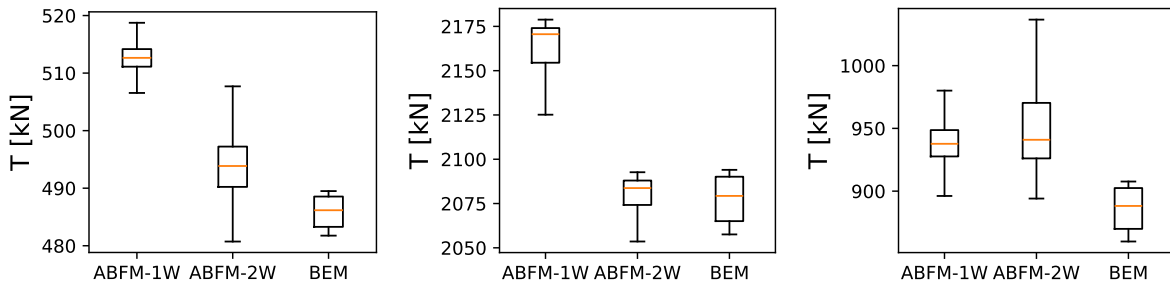


Figure 5.2: Distribution of thrust for the ABFM-1W and ABFM-2W, as compared to the BEM model of Appendix B for a sheared inflow at: $5 \frac{m}{s}$ (left), $10.5 \frac{m}{s}$ (middle) and $20 \frac{m}{s}$ (right)

5.1.2. Turbine Power

A similar analysis to that performed for the thrust is now repeated for the power. The resulting statistical distributions of the turbine power in time for the uniform and sheared cases are shown in Figure 5.3 and Figure 5.4, respectively. Once again, the trends are similar for uniform and sheared flows, which suggests that calibrating based on $\overline{\rho u_d^3}$ can reliably capture the behaviour for different inflow profiles.

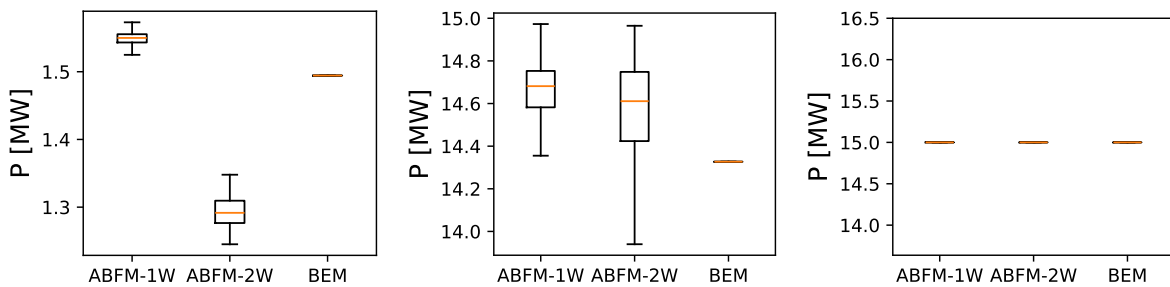


Figure 5.3: Distribution of power for the ABFM-1W and ABFM-2W, as compared to the BEM model of Appendix B for a uniform inflow at: $5 \frac{m}{s}$ (left), $10.5 \frac{m}{s}$ (middle) and $20 \frac{m}{s}$ (right)

Overall, the ABFM-2W shows a larger spread in the power at lower velocities. This is likely caused by the ABFM-2W allowing for non-uniform induction over the disk, making it more difficult to correlate $\overline{\rho u_d^3}$ with the turbine conditions. Still, for most cases, the predicted power of both models closely matches the BEM reference. Only for the $U_0 = 5 \frac{m}{s}$ case in Figure 5.3 is the power of the ABFM-2W significantly underestimated, showing a deviation of over 13%. Presumably, this is because $P \propto \overline{\rho u_d^3}$, making the power estimation highly sensitive to the disk velocity. As this quantity cannot be measured with perfect accuracy, some uncertainty in the power estimate is inevitable. Since the total power is substantially lower at $5 \frac{m}{s}$, the relative error is larger for this case.

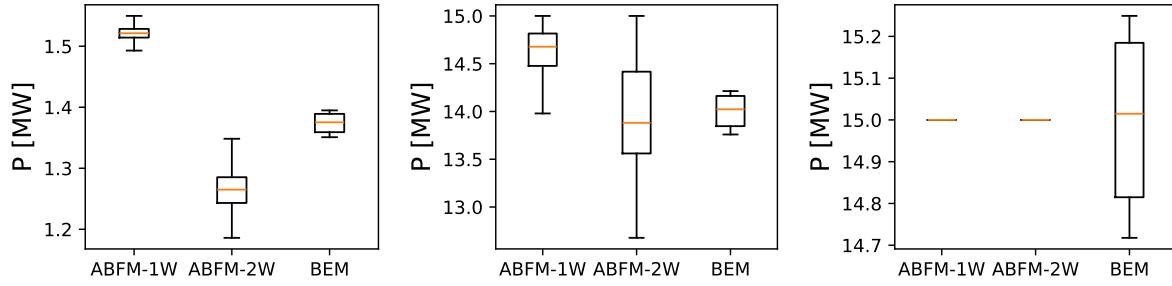


Figure 5.4: Distribution of power for the ABFM-1W and ABFM-2W, as compared to the BEM model of Appendix B for a sheared inflow at: $5 \frac{m}{s}$ (left), $10.5 \frac{m}{s}$ (middle) and $20 \frac{m}{s}$ (right)

At $10.5 \frac{m}{s}$, the predicted power is below the rated value. As shown in Figure 3.14, the achieved freestream velocity at the disk is slightly lower than $10.5 \frac{m}{s}$, which explains why the power is slightly below rated as well. The ABFM-1W and ABFM-2W deviate by only a few percent with respect to the BEM prediction, despite the inclusion of turbulence in these models. At $20 \frac{m}{s}$, the velocity is far above rated. Since the power is capped to the rated value, there is no spread in the distribution for ABFM-1W and ABFM-2W. For the BEM simulation under sheared inflow conditions, shown in Figure 5.4, the power oscillates slightly around its mean value. This is caused by the blades periodically passing through regions of higher and lower velocity. As explained in subsection 5.1.1, this high-frequency oscillation cannot be captured by the freestream velocity calibration and is thus absent in the ABFM-1W and ABFM-2W.

5.2. Evaluation of Blade Force Distributions

In section 5.1, it was seen that in most scenarios, the thrust and power of the turbine could be reconstructed with acceptable accuracy. This is a prerequisite for accurately modelling the blade load distributions, since thrust and power are input values to the ABFM.

This section will now evaluate to what extent the blade loads can be reproduced by both the ABFM-1W and ABFM-2W. The results are compared with the BEM reference in subsection 5.2.1 for the uniform flow, and in subsection 5.2.2 for the sheared flows.

5.2.1. Uniform Flows

A baseline for the behaviour of the ABFM in uniform flows has been established in chapter 4. This section investigates whether these results are consistent along different velocities. At each LES time step, the disk loading distributions $f_{ax}(x, \theta)$ and $f_{az}(x, \theta)$ are determined for both the ABFM-1W and ABFM-2W. In addition, a time series of the blade position is recorded by calculating the rotational speed of the blade from Equation 3.23. The time series of the blade loading can then be constructed from Equation 3.36 and Equation 3.37 by evaluating them at $\theta = \theta_{blade}(t)$.

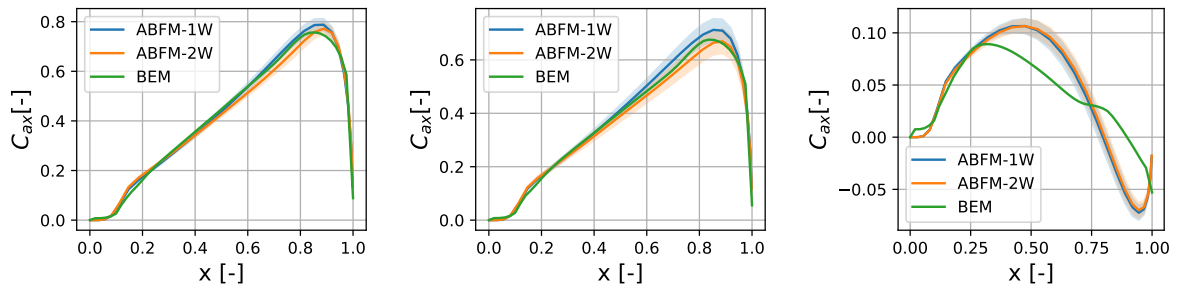


Figure 5.5: Axial force coefficient of the ABFM-1W and ABFM-2W, as compared to the BEM model of Appendix B for a uniform inflow. The lines indicate the time-averaged value, while the shaded area shows the area of $\mu \pm 2\sigma$. Cases: $5 \frac{m}{s}$ (left), $10.5 \frac{m}{s}$ (middle) and $20 \frac{m}{s}$ (right)

The resulting axial force coefficients are shown in Figure 5.5, where the solid lines indicate the time-averaged values and the shaded area represents the range within two standard deviations of the mean. As a reference, the BEM results, obtained using the model described in Appendix B, are also shown. Since the BEM results are generated using a steady inflow, the solution remains constant in time, resulting in a standard deviation of zero.

The distribution is captured very well at both $5 \frac{m}{s}$ and $10.5 \frac{m}{s}$, although at the latter, the ABFM-1W predicts a slightly too high loading. This overestimation is directly caused by an overprediction of the thrust, as noted earlier in Figure 5.1. Although the axial force remains reasonably accurate for this specific case, it illustrates that accurate modelling of the blade loads depends directly on how precisely the turbine operating conditions can be determined.

The right graph of Figure 5.5 shows that at $20 \frac{m}{s}$, the axial force is captured with significantly lower accuracy. This is in accordance with the results of subsection 4.1.3, which showed that the ABFM inherently struggles under operating conditions far from rated. However, it should be noted that the ABFM-1W and ABFM-2W reconstruct the loading without any knowledge of the geometry of the turbine. Considering this, the resulting distribution is significantly more accurate than the assumption of a uniform loading, as used in alternative AD models that do not contain geometric inputs. Both ABFM models accurately resolve the inner part of the blade, but lose their accuracy for $x > 0.25$. Nevertheless, the overall trend of the loading distribution is captured to some extent.

As mentioned in subsection 4.2.1, the turbulence intensity for the uniform inflow case is relatively low, at approximately 2% at the rotor. Even at this low turbulence level its influence is clearly not negligible. Especially at $10.5 \frac{m}{s}$, the standard deviation of the loading is considerable. This is expected, since the turbine curve is the steepest around this velocity, as can be seen in Appendix B.

In addition to the axial force coefficient, the azimuthal force coefficient is also evaluated. These results are shown in Figure 5.6. In the left graph of Figure 5.6, it can be seen that at $5 \frac{m}{s}$, both the ABFM-1W and ABFM-2W show a large discrepancy. It is important however, to understand the underlying cause for each model.

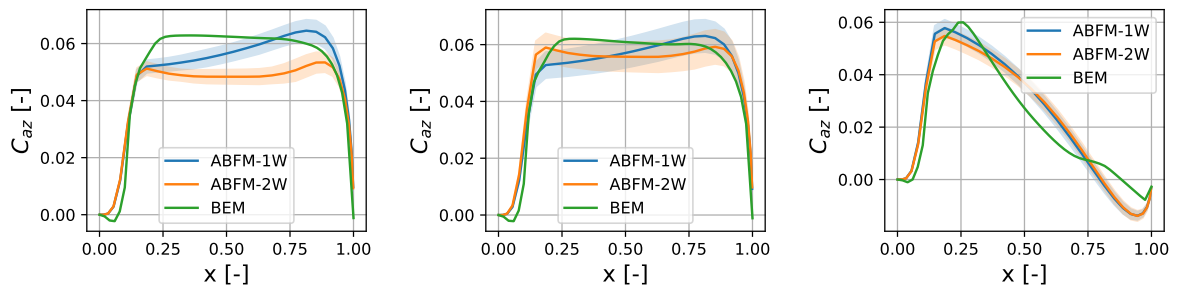


Figure 5.6: Azimuthal force coefficient of the ABFM-1W and ABFM-2W, as compared to the BEM model of Appendix B for a uniform inflow. The lines indicate the time-averaged value, while the shaded area shows the area of $\mu \pm 2\sigma$. Cases: $5 \frac{m}{s}$ (left), $10.5 \frac{m}{s}$ (middle) and $20 \frac{m}{s}$ (right)

The ABFM-1W appears to better capture the total power, as confirmed by Figure 5.3. However, it completely fails to reproduce the shape of the distribution, predicting an increasing trend instead of the intended (almost) flat profile. As previously discussed in subsection 4.2.4, this discrepancy is directly caused by the force smearing algorithm of the uniform AD model and cannot be resolved without fundamentally altering the LES setup. For the ABFM-2W, on the other hand, the overall shape of the distribution is captured reasonably well across most of the blade. Near the tip, a slight increase is observed, which, as discussed in subsection 4.3.4, is caused by interpolation artifacts near the edge of the disk. Nevertheless, this effect is relatively small and the main discrepancy lies in the underprediction of the loading across the entire blade. This suggests that the turbine power is not accurately predicted, which is consistent with the conclusions from subsection 5.1.2. It is therefore expected that, if the turbine conditions are accurately reconstructed, the ABFM-2W outperforms the ABFM-1W.

This is confirmed by the middle graph of Figure 5.6, which shows the azimuthal force coefficient at

$10.5 \frac{m}{s}$. In this case, both the ABFM-1W and ABFM-2W matched the power prediction well, as was shown Figure 5.3. Consequently, ABFM-2W shows significantly better agreement with the BEM solution, while the ABFM-1W still fails to capture the correct shape of the distributions and predicts an increasing loading along the radial direction.

At $20 \frac{m}{s}$, as shown in the right graph of Figure 5.6, both ABFM models show a surprisingly good agreement with the BEM reference. The ABFM results appear smoother, which is expected for an analytical model. In contrast, the BEM solution exhibits notable kinks, caused by changes in airfoil geometry along the blade span. It makes sense that the ABFM cannot capture these strongly geometry-dependent effects, but the overall trend of the azimuthal loading is still captured with decent accuracy.

Apart from that, the azimuthal force coefficient appears to be even more sensitive to turbulence than the axial coefficient. It was already seen in subsection 4.2.4 and subsection 4.3.4 that this coefficient is indeed very sensitive to the disk velocity distribution. The effect is most pronounced at $10.5 \frac{m}{s}$, where the gradient of the power curve is steepest. At $20 \frac{m}{s}$, on the other hand, the standard deviation is significantly reduced. This occurs because, above rated velocity, the total power remains constant with wind speed. Changes in the loading are then only affected by changes in tip-speed ratio and redistribution of loading over the disk due to heterogeneity in the inflow.

5.2.2. Sheared Flows

In subsection 5.2.1, it was seen that the ABFM-1W and ABFM-2W provide useful load predictions for uniform flows. This section will now evaluate how well the models perform under a sheared inflow, which requires accurately resolving the effects of non-uniform inflow. First, subsection 5.2.2.1 will evaluate the loading in a manner similar to subsection 5.2.1, by considering the time series of the blade position. Then, the azimuthal dependencies will be analysed in greater detail in subsection 5.2.2.2 by evaluating the forces at two distinct azimuthal positions.

5.2.2.1. Time-averaged Blade Loading

The blade loading will be determined in the same way as in subsection 5.2.1. At each time step, the blade position is determined from the rotational speed of the rotor. The disk loading distribution is then evaluated at the corresponding blade location and converted into blade loads using Equation 3.36 and Equation 3.37. The resulting distributions are averaged in time and the results are shown in Figure 5.7 and Figure 5.8. Again, the shaded area indicates the region within two standard deviations from the mean.

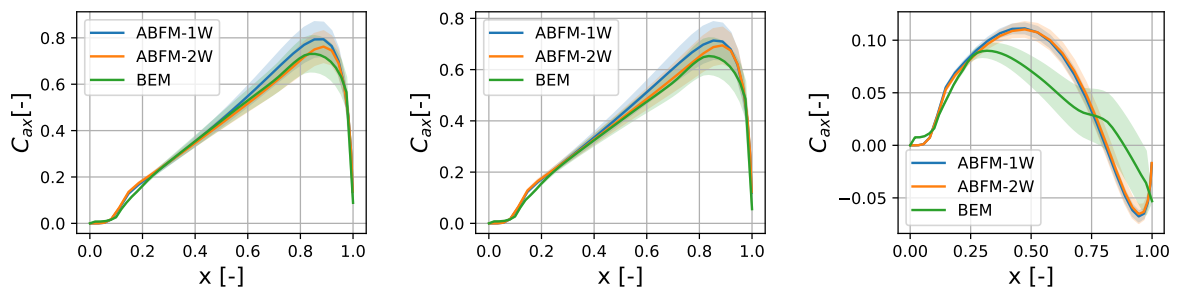


Figure 5.7: Axial force coefficient of the ABFM-1W and ABFM-2W, as compared to the BEM model of Appendix B for a sheared inflow. The lines indicate the time-averaged value, while the shaded area shows the area of $\mu \pm 2\sigma$. Cases: $5 \frac{m}{s}$ (left), $10.5 \frac{m}{s}$ (middle) and $20 \frac{m}{s}$ (right)

It can be seen that the standard deviation of both the axial and azimuthal loading over time is significantly greater than in Figure 5.5 and Figure 5.6. This is a direct consequence of wind shear, because the observed velocity profile experienced by the blade changes significantly at each time step as it moves around the disk. Because the sheared inflow profile is not symmetric, see Figure 3.14 and because the aerodynamic forces do not scale linearly with velocity, the resulting force distribution is skewed around the mean. For clarity, only the mean and standard deviation are shown here. However, since the complete time series is available, higher-order statistical moments can also be evaluated, if desired.

For sheared inflows, the total thrust was captured accurately, as shown in Figure 5.2. Consequently, the average axial force coefficient is expected to be accurately predicted as well. For the first two graphs of Figure 5.7, corresponding to $5 \frac{m}{s}$ and $10.5 \frac{m}{s}$, this is indeed the case, although the axial force is slightly overpredicted near the tip. At $20 \frac{m}{s}$, in the right graph of Figure 5.7, the ABFM-1W and ABFM-2W fail to accurately reconstruct the average profile. This should be expected, since this was also the case for the uniform inflow in Figure 5.5.

For the average azimuthal force coefficient in Figure 5.8, the observations are similar to those in Figure 5.6. The ABFM-2W more accurately reconstructs the shape of the loading distribution, while the ABFM-1W systematically predicts an increasing load along the span, consistent with the conclusions of subsection 4.2.4. At $5 \frac{m}{s}$, the ABFM-2W again underpredicts the loading. Similar to the uniform case, this is caused by an underestimation of the predicted turbine power, as shown in Figure 5.4. At $10.5 \frac{m}{s}$, both models are in reasonable agreement with the BEM results, with the ABFM-2W capturing the shape of the distribution slightly better. As with the uniform inflows, the detailed BEM profile at $20 \frac{m}{s}$, in the right graph of Figure 5.8, cannot be fully reconstructed, although the overall shape of the distribution remains reasonably close.

For both the axial and azimuthal loading, the standard deviations are large relative to the mean loading, even for the BEM reference solution, which only considers steady conditions. This indicates that the change in loading over a single revolution is much greater than the variation in loading due to turbulent effects. Consequently, isolating the effect of turbulence from these plots is challenging. Instead an alternative approach is required, which will be demonstrated in subsection 5.2.2.2.

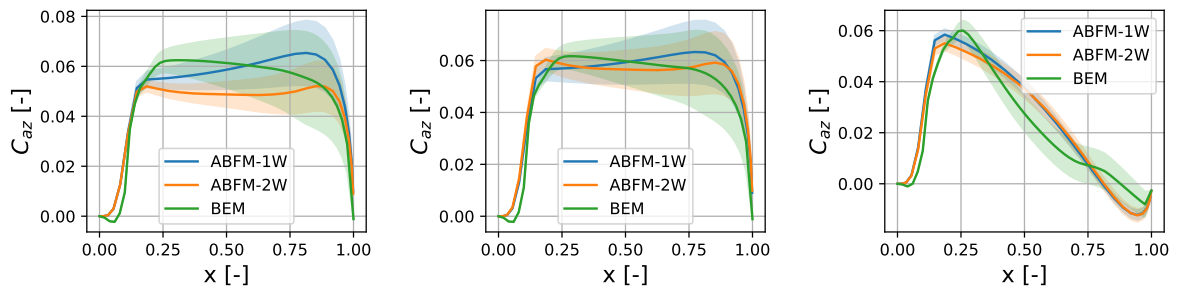


Figure 5.8: Azimuthal force coefficient of the ABFM-1W and ABFM-2W, as compared to the BEM model of Appendix B for a sheared inflow. The lines indicate the time-averaged value, while the shaded area shows the area of $\mu \pm 2\sigma$. Cases: $5 \frac{m}{s}$ (left), $10.5 \frac{m}{s}$ (middle) and $20 \frac{m}{s}$ (right)

5.2.2.2. Azimuthal Dependencies of the Blade Loading

In subsection 5.2.2.1, the average blade loading over time was shown, as would be experienced by a blade rotating through the rotor disk. This approach was ideal for determining the mean loading, but makes direct evaluation of the load profile across the disk difficult. This section will therefore focus on the blade loading at two distinct azimuthal positions.

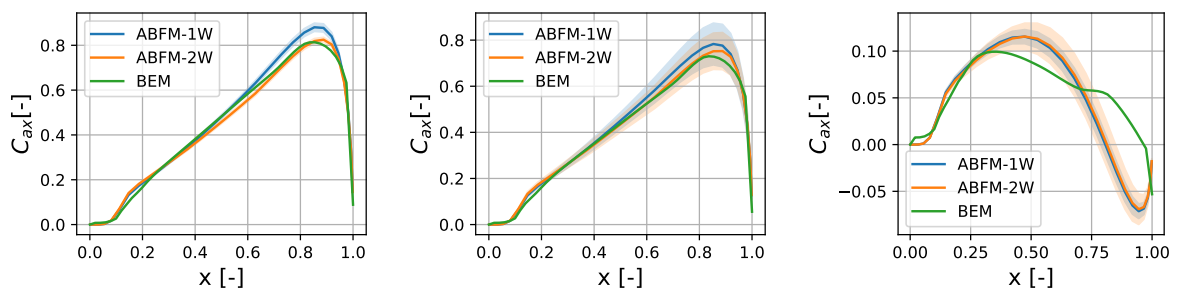


Figure 5.9: Axial force coefficient of the ABFM-1W and ABFM-2W, as compared to the BEM model of Appendix B for a sheared inflow. The lines indicate the time-averaged value at a constant position of $\theta = \frac{\pi}{2}$, while the shaded area shows the area of $\mu \pm 2\sigma$. Cases: $5 \frac{m}{s}$ (left), $10.5 \frac{m}{s}$ (middle) and $20 \frac{m}{s}$ (right)

For this analysis, the blade location is fixed at $\theta = \frac{\pi}{2}$ and $\theta = \frac{3\pi}{2}$. These angles corresponds to the position where the turbine blade points straight up and straight down, respectively. Due to the sheared wind profile, these locations correspond, on average, to the moment during a revolution where the blade experiences its minimal and maximal forces. The resulting axial force coefficients are shown in Figure 5.9 and Figure 5.10 for $\theta = \frac{\pi}{2}$ and $\theta = \frac{3\pi}{2}$, respectively. The shaded area indicates the region within two standard deviations of the mean.

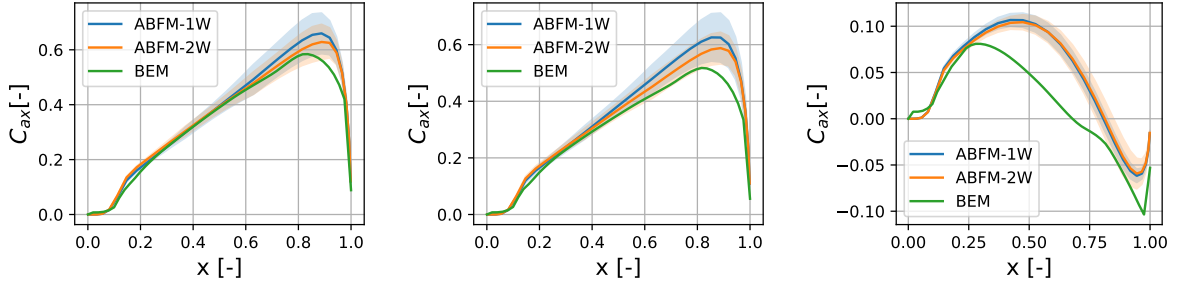


Figure 5.10: Axial force coefficient of the ABFM-1W and ABFM-2W, as compared to the BEM model of Appendix B for a sheared inflow. The lines indicate the time-averaged value at a constant position of $\theta = \frac{3\pi}{2}$, while the shaded area shows the area of $\mu \pm 2\sigma$. Cases: $5 \frac{m}{s}$ (left), $10.5 \frac{m}{s}$ (middle) and $20 \frac{m}{s}$ (right)

The time-averaged axial loads in Figure 5.7 were overestimated by both the ABFM-1W and the ABFM-2W. For $\theta = \frac{\pi}{2}$, Figure 5.9 shows that the axial forces are in closer agreement with the BEM results for all velocities. However, if the effect of shear were captured correctly, the forces at $\theta = \frac{\pi}{2}$ would be expected to be underestimated. This suggests that the effect of shear is not completely resolved. Further confirmation is provided by evaluating the axial forces at $\theta = \frac{3\pi}{2}$ in Figure 5.10, where the blade pointing downward. In this case, the axial forces are clearly overestimated with respect to BEM. The effect is most noticeable near the tip, where the local velocity deviates the most from the reference velocity.

These trends are even more pronounced for the azimuthal force coefficients at $\theta = \frac{\pi}{2}$ and $\theta = \frac{3\pi}{2}$, shown in Figure 5.11 and Figure 5.12, respectively. For each velocity, Figure 5.11 clearly shows that the azimuthal forces are lower than the BEM reference for $\theta = \frac{\pi}{2}$. However, both ABFM successfully capture the positive force gradient along the mid-span. Conversely, both models correctly predict a downward gradient at $\theta = \frac{3\pi}{2}$, as shown in Figure 5.12, although the forces themselves are overestimated, particularly near the tip.

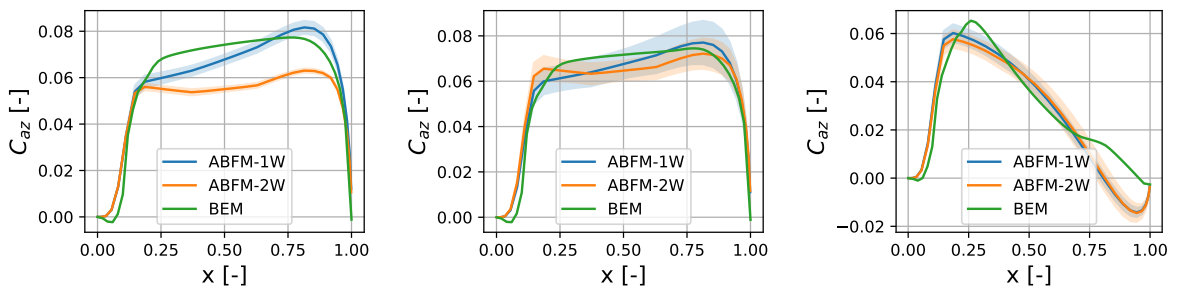


Figure 5.11: Azimuthal force coefficient of the ABFM-1W and ABFM-2W, as compared to the BEM model of Appendix B for a sheared inflow. The lines indicate the time-averaged value at a constant position of $\theta = \frac{\pi}{2}$, while the shaded area shows the area of $\mu \pm 2\sigma$. Cases: $5 \frac{m}{s}$ (left), $10.5 \frac{m}{s}$ (middle) and $20 \frac{m}{s}$ (right)

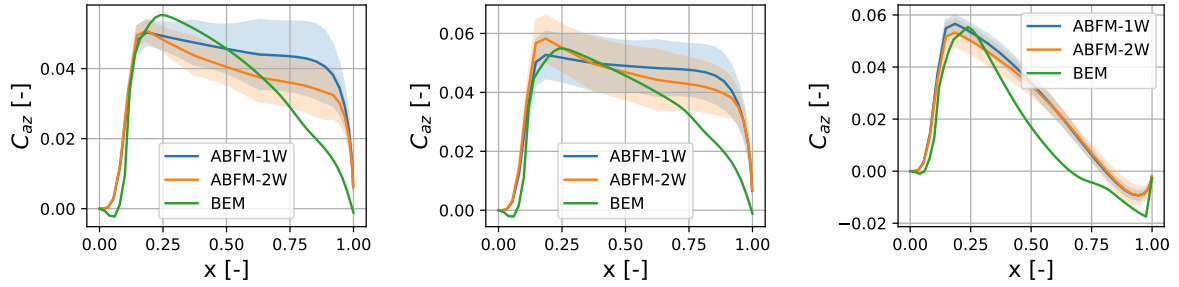


Figure 5.12: Azimuthal force coefficient of the ABFM-1W and ABFM-2W, as compared to the BEM model of Appendix B for a sheared inflow. The lines indicate the time-averaged value at a constant position of $\theta = \frac{\pi}{2}$, while the shaded area shows the area of $\mu \pm 2\sigma$. Cases: $5 \frac{m}{s}$ (left), $10.5 \frac{m}{s}$ (middle) and $20 \frac{m}{s}$ (right)

Overall, the ABFM-2W more accurately captures the effect of shear than the ABFM-1W, as the shape of the distributions matches the BEM reference more closely. This is expected, as the ABFM-2W showed a superior capability to resolve the disk velocity. Still, both models tend to underestimate the forces at $\theta = \frac{\pi}{2}$, while overestimating them at $\theta = \frac{3\pi}{2}$. Recall that the thrust and power coefficients are an input to both ABFM models. In reality, these coefficients are dependent on the azimuthal position of the turbine blade. However, for practical purposes these coefficients had to be obtained from the calibration procedure described in subsection 3.2.2. This calibration cannot resolve the thrust and power gradients on the timescale of a single revolution, because it makes use of time-averaged disk quantities with a timescale of $\tau = 10s$, as explained in subsection 3.2.3. As a result, the thrust and power coefficient inputs to the ABFM are azimuthally independent.

Therefore, the ABFM-1W and ABFM-2W can only resolve the average effect of shear. These models distribute the thrust and power, averaged over multiple revolutions, across the disk such that the loading is consistent with the measured disk velocity. As a direct result, the time gradients of thrust and power on the timescale of a single revolution are not captured, causing minima and maxima in the loading along the azimuthal direction to be flattened out, consistent with the observations in Figure 5.9- Figure 5.12. The axial forces are constrained by the thrust coefficient, while the azimuthal forces are constrained by the power coefficient. Since the power is proportional to U^3 , the relative changes in power over a revolution are larger than the relative changes in thrust, which explains why this effect is more pronounced for the azimuthal forces than for the axial forces.

5.3. Comparison of Wake Characteristics

In section 5.2, the blade load distributions were obtained using the ABFM-1W and ABFM-2W. In most cases, these models provided accurate results, comparable to those obtained from BEM. Even in cases where the distributions were less accurate, the models still provided significantly more information than the assumption of a constant load distribution used by uniform AD models.

Therefore, the ABFM-2W is expected to yield a more realistic wake behaviour than the ABFM-1W. As a baseline, subsection 5.3.1 presents the wake characteristics of both models for a uniform inflow at $10.5 \frac{m}{s}$. Next, the influence of the inflow profile is examined by analysing the wakes of a sheared flow at $10.5 \frac{m}{s}$ in subsection 5.3.2. The section ends with an analysis of how turbine conditions affect the wake, based on the simulation of a uniform inflow at $20 \frac{m}{s}$, as presented in subsection 5.3.3.

5.3.1. Uniform Inflow at Rated Velocity

For both the ABFM-1W and ABFM-2W, the flow field is recorded during the simulation. These fields are now used to visualise the wakes. Since the ABFM-1W does not actively communicate any loads to the LES, this simulation represents the wakes of a uniform AD model, implemented using the ASPTurbine module of ASPIRE. The ABFM-2W, on the other hand, actively couples the load distributions obtained by the model back to the LES.

To understand the wake differences between the two models, Figure 5.13 presents the instantaneous axial velocity profile behind the turbine for both the ABFM-1W and the ABFM-2W. For the ABFM-1W,

on the left of Figure 5.13, the influence of the uniform AD model is clear, as the wake itself is very uniform. In contrast, the ABFM-2W in the right panel of Figure 5.13 shows a clear root vortex in the near-wake of the turbine, caused by the force distribution going to zero at the root.

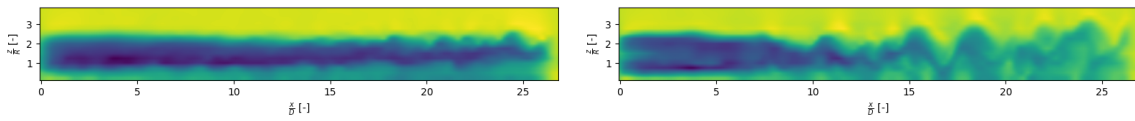


Figure 5.13: Instantaneous velocity profile downstream of the turbine for a uniform inflow profile of $10.5 \frac{m}{s}$. Left: ABFM-1W, Right: ABFM-2W

Moreover, the wake of the ABFM-2W is visually more turbulent. At approximately seven rotor diameters downstream of the turbine, instabilities become visible and rapidly develop into turbulent wake breakdown by around ten diameters. For the ABFM-1W, on the other hand, notable instabilities only begin to form at approximately 15 diameters downstream and a complete turbulent wake breakdown does not occur. It is worth noting that the freestream turbulence intensity at hub-height was only 2%. In practice, the stability of the ABL has a significant effect on the wake development as well. Nevertheless, Figure 5.13 demonstrates that the method used to project the turbine forces onto the LES can significantly influence the characteristics of the wake.

To further investigate the wake characteristics, the time-averaged axial velocity of the ABFM-1W and ABFM-2W at four different downstream positions is visualised in the top and bottom panels of Figure 5.14, respectively. In this figure, the rotor disk is indicated by a dotted line as a reference. For the ABFM-1W, the smearing effect of the 3D Gaussian kernel is evident. Even at only one diameter downstream of the turbine, the wake exhibits a significant radial gradient, extending well beyond the rotor disk. Although some wake expansion behind the turbine is expected, the observed effect here appears to be artificial. The resulting smoothing effect is more pronounced in the horizontal direction than in the vertical direction, consistent with the smearing lengths chosen for each axis in subsection 3.3.4.

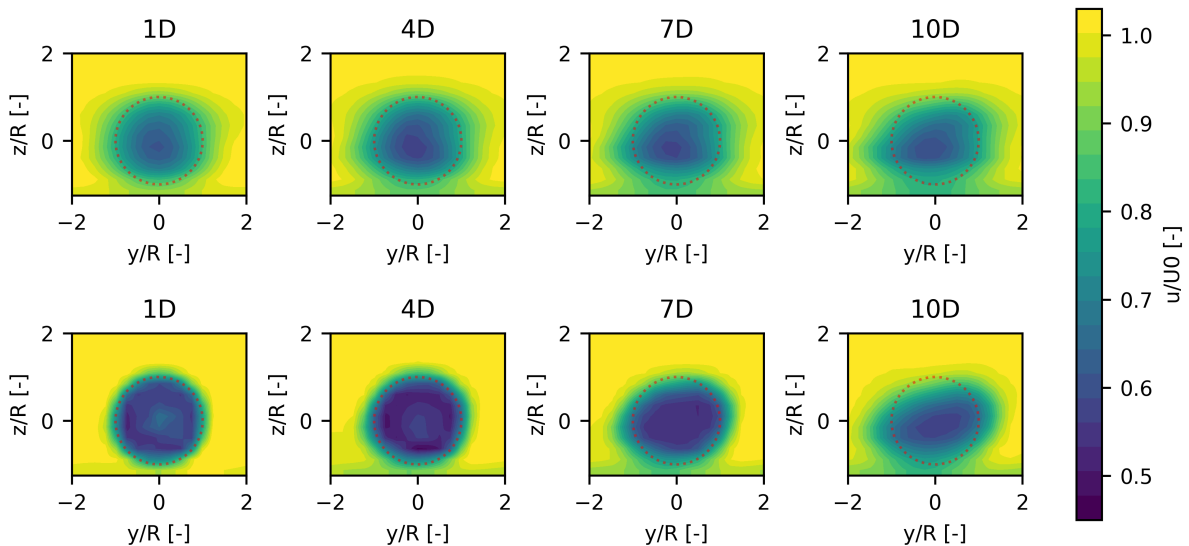


Figure 5.14: Non-dimensional time-averaged axial velocity downstream of the turbine at four distinct planes for a uniform inflow at $10.5 \frac{m}{s}$. The rotor disk is indicated by the dotted line. Top: ABFM-1W, Bottom: ABFM-2W

For the ABFM-2W, shown in the bottom of Figure 5.14, the results appear more physically realistic. At one diameter downstream, the radius of the wake is similar to that of the turbine. Further downstream the wake gradually expands as it decelerates further. At one and four diameters downstream, the root vortex is also visible for the ABFM-2W. At larger downstream distances, this vortex breaks down due to mixing with the surrounding wake.

The wake expansion of both models primarily occurs in the horizontal direction. This is partly due to interference with the ground, which limits downwards expansion of the wake. Additionally, the ambient conditions in the LES resemble a stable ABL, which suppress vertical movement.

For a more quantitative analysis, the wake profiles from Figure 5.14, evaluated at $\frac{z}{R} = 0$, are shown in Figure 5.15. Once again, the smearing of the ABFM-1W wake is evident, as the velocity profile exhibits a wide Gaussian shape. As a result, the wake deficit of the ABFM-1W is smaller than that of the ABFM-2W, except at the root vortex at one diameter downstream. The effect of the force distribution of the ABFM-2W on the radial induction profile is clearly visible in the wake close to the rotor. Further downstream, the wake mixes with the atmosphere, resulting in a more uniform velocity profile. As a result, the wakes of the ABFM-1W and ABFM-2W start to look more similar further downstream. However, at seven diameters downstream the two models still predict a distinctly different wake profile. Only after ten rotor diameters are the profiles of the two models close to each other. The wakes of both models are not symmetric around $\frac{y}{R} = 0$, but instead are slightly shallower for positive y -values. This is caused by the rotation of the wake due to azimuthal forces of the turbine.

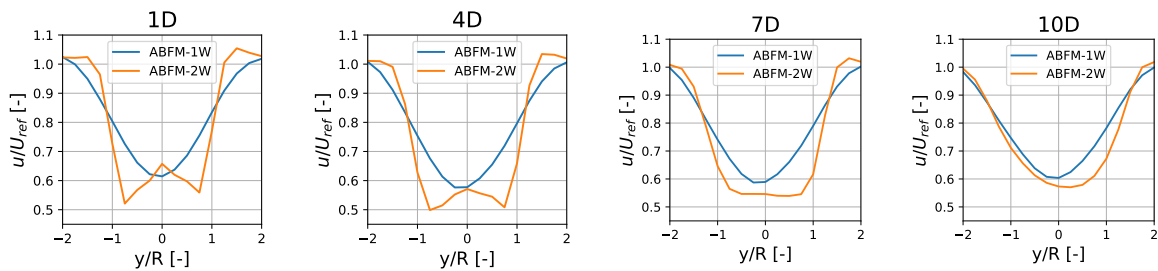


Figure 5.15: Time-averaged non-dimensional axial velocity profile along the horizontal direction for $\frac{z}{R} = 0$ at multiple downstream locations

A similar analysis to that of Figure 5.15 can be performed by evaluating the velocity profiles in Figure 5.14 along the vertical direction, specifically at $\frac{y}{R} = 0$. In this case, the profiles only extend up to the ground at $z = -1.25R$ in the negative z -direction. On the lower half of the turbine, the wakes show a slightly higher velocity deficit, as less mixing with air from the atmosphere can occur.

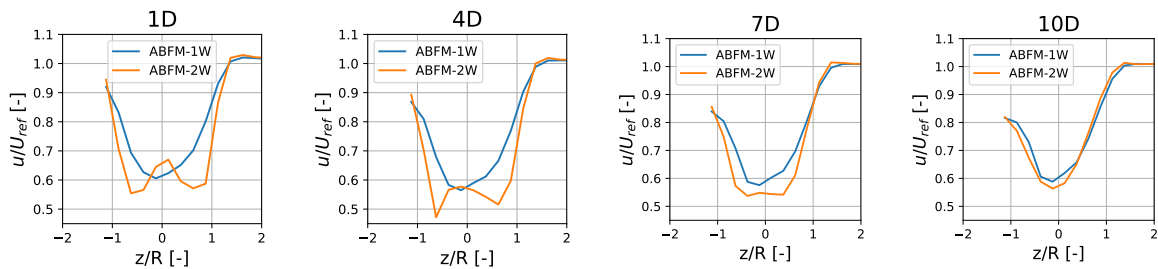


Figure 5.16: Time-averaged non-dimensional axial velocity profile along the vertical direction at $\frac{y}{R} = 0$ at multiple downstream locations

As discussed above, the smearing length of the ABFM-1W is smaller along the vertical direction and, as a result, resulting in less severe smoothing effects. Consequently, the ABFM-1W and ABFM-2W wakes converge to the same shape more rapidly along this direction, especially for $\frac{z}{R} > 1$.

In addition to the axial velocity, the azimuthal velocity of the wake will be analysed. The vertical azimuthal velocity profiles at $\frac{y}{R} = 0$ are shown in Figure 5.17 for the same four downstream positions. It can be seen that the wake rotation near the center of the ABFM-2W wake is significantly higher than for the ABFM-1W. This demonstrates the impact of explicitly projecting the force distribution, rather than assuming a uniform one.

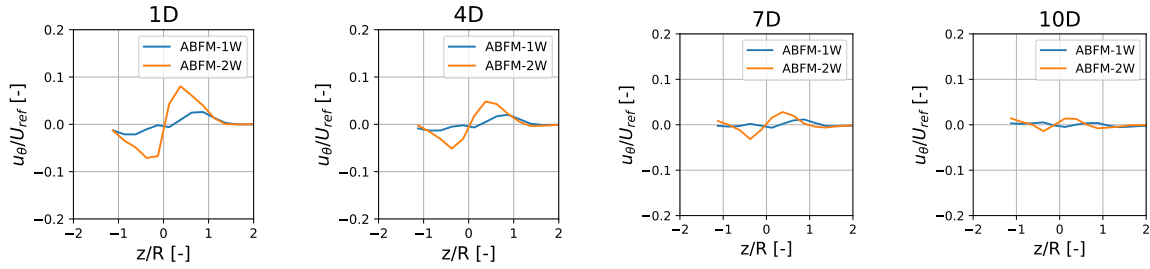


Figure 5.17: Time-averaged non-dimensional azimuthal velocity profile at multiple downstream locations for the ABFM-1W and the ABFM-2W.

From subsection 4.3.3, it can be seen that the peak azimuthal forces on the disk predominantly occur close to the root. The total azimuthal force projected onto the grid is determined from the power. When assuming a uniform distribution, this power is achieved for a lower total imposed azimuthal force compared to when the distribution of Figure 4.26 is used. As such, the wake rotation close to the rotor is significantly underpredicted for the ABFM-1W. These effects are most notable at the downstream positions of $1D$ and $4D$. For both models, most of the rotation is already dampened out at $7D$ and at $10D$ both models predict only a very small rotational component of the wake.

Another important parameter is the turbulence intensity, defined as the standard deviation of the velocity, divided by its mean. Strong velocity gradients along the edge of the wake generate shear stresses that promote mixing with the atmosphere, thereby increasing turbulent fluctuations. The vertical turbulence intensity profile at $\frac{y}{R} = 0$ is shown in Figure 5.18, for the same downstream positions of $1D$, $4D$, $7D$, and $10D$. Instabilities in the flow require time to develop, resulting in a low dependence of turbulence intensity on the projection method near the rotor, as is clearly evident at $1D$. However, at $4D$ the turbulence intensity of the ABFM-2W is already significantly higher than for the ABFM-1W. This is in agreement with the findings from Figure 5.13, where more turbulence was observed for the ABFM-2W.

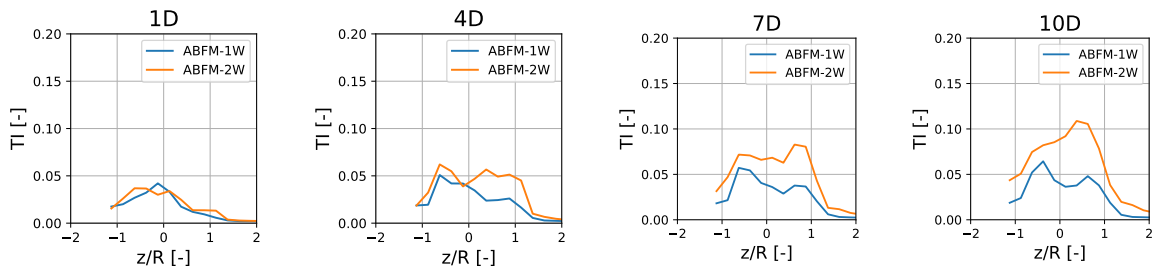


Figure 5.18: Time-averaged turbulence intensity along the vertical direction for $\frac{y}{R} = 0$ at multiple downstream locations for the ABFM-1W and the ABFM-2W.

This higher turbulence intensity is likely driven by two different mechanisms. First, the ABFM-2W resolves the root vortex, which is entirely neglected by a uniform AD model. Second, the ABFM-2W consistently exhibits higher velocity gradients, both within the wake and at the interface with the ambient flow, compared to the ABFM-1W. As a result, higher stresses are imposed on the flow, leading to enhanced turbulent fluctuations.

5.3.2. Sheared Inflow at Rated Velocity

When the inflow profile is sheared, the resulting turbine wake will also be sheared. This subsection examines the wake characteristics of both the ABFM-1W and ABFM-2W for the S105 case listed in Table 3.2.

The instantaneous axial velocity profile for these simulations is shown in the left and right plots of Figure 5.19, respectively. Compared to Figure 5.13, the velocity close to the ground is lower due to

the shear. Similar to the uniform inflow case, the ABFM-2W shows a larger production of turbulence and a turbulent wake breakdown at approximately ten diameters downstream of the turbine. Again, the ABFM-1W wake remains more stable, likely due to smearing effects and the absence of the root vortex.

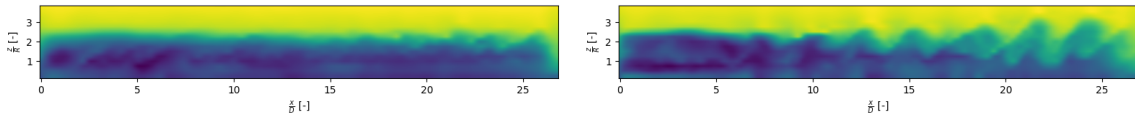


Figure 5.19: Instantaneous velocity profile downstream of the turbine for a sheared inflow profile of $10.5 \frac{m}{s}$. Left: ABFM-1W, Right: ABFM-2W

The time-averaged axial velocity at multiple downstream locations is visualised in Figure 5.20. A significant vertical gradient can be observed in both the wake and the ambient flow due to the wind shear. The smearing effects of the ABFM-1W are even more pronounced than those observed in the uniform inflow case. This effect is most clearly visible at one diameter downstream in the top panel of Figure 5.20, where the contour lines outside of the rotor disk do not return to a horizontal orientation, especially at $\frac{y}{R} = -2$. This is in contrast to the ABFM-2W, where the contour lines outside of the wake quickly return to horizontal, indicating a steep boundary between the wake and the ambient flow.

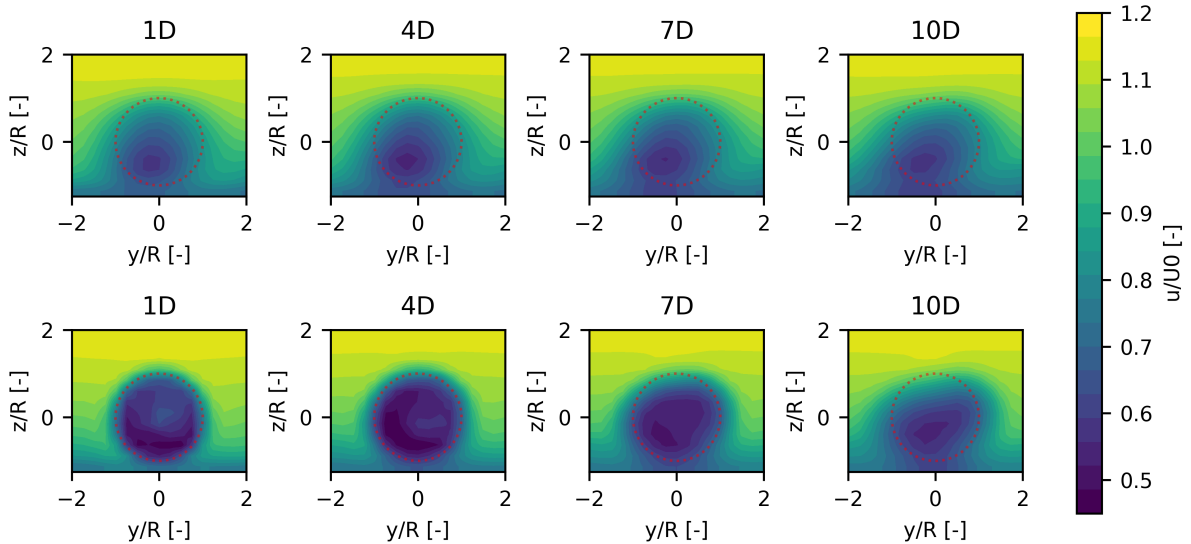


Figure 5.20: Non-dimensional time-averaged axial velocity downstream of the turbine at four distinct planes for a sheared inflow at $10.5 \frac{m}{s}$. The rotor disk is indicated by the dotted line. Top: ABFM-1W, Bottom: ABFM-2W

The axial velocity profile at $\frac{y}{R} = 0$ in the vertical direction downstream of the turbine is further clarified by Figure 5.21. The trends are very similar to those of the uniform inflow profile shown in Figure 5.16, with the exception that there is a clear vertical velocity gradient imposed by the inflow. For the ABFM-2W, the root vortex remains distinguishable up to 4 diameters downstream of the turbine, although it no longer defines the shallowest part of the wake. As seen for the uniform inflow, the sharp gradients within the wake of the ABFM-2W have flattened out around seven rotor diameters downstream and by ten diameters the wake closely resembles that of the ABFM-1W.

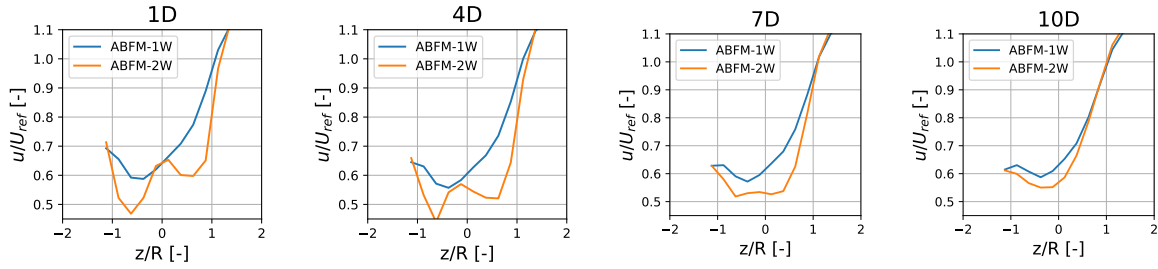


Figure 5.21: Time-averaged non-dimensional axial velocity profile along the vertical directions for $\frac{y}{R} = 0$ at multiple downstream locations for the ABFM-1W and the ABFM-2W for a sheared inflow.

The azimuthal velocity for the sheared wake is shown in Figure 5.22. Again, the trends are nearly identical to those in Figure 5.17. Only at one diameter downstream is the maximal azimuthal velocity slightly higher than in the uniform case, but the difference is almost negligible.

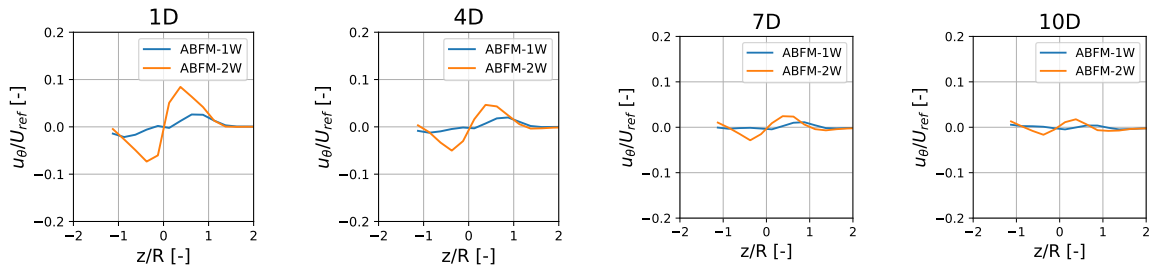


Figure 5.22: Time-averaged non-dimensional azimuthal velocity profile along the vertical direction for $\frac{y}{R} = 0$ at multiple downstream locations for the ABFM-1W and the ABFM-2W for a sheared inflow.

For the turbulence intensity, however, the impact of shear is significant. Figure 5.23 shows the turbulence intensity along the vertical direction at $\frac{y}{R} = 0$ for various downstream locations. A Comparison with Figure 5.18 reveals that, at one diameter downstream of the turbine, the turbulence intensity close to the ground is significantly higher. This is expected, since the velocity gradient along the z -axis induces additional shear stresses onto the flow, which promotes instabilities. As the velocity gradient is largest in the lower part of the disk, the associated shear stresses are also greater in this region, leading to a higher turbulence intensity near the ground.

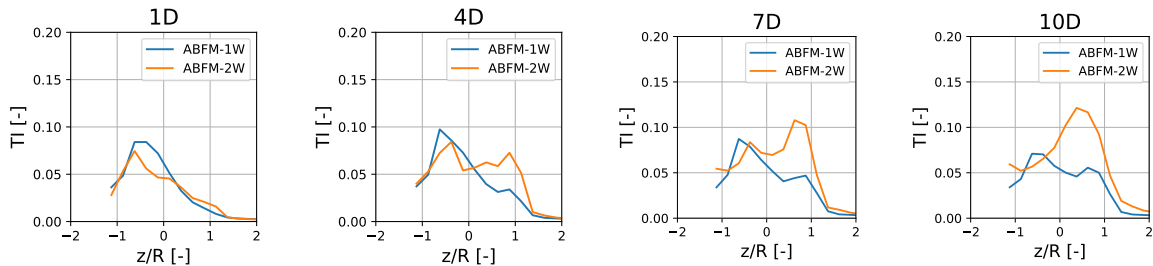


Figure 5.23: Time-averaged turbulence intensity along the vertical direction for $\frac{y}{R} = 0$ at multiple downstream locations for the ABFM-1W and the ABFM-2W for a sheared inflow.

In contrast to the uniform flow, the turbulence intensity for a sheared inflow in the lower half of the disk is higher for the ABFM-1W than the ABFM-2W, especially at $x = 1D$ and $x = 4D$. This difference is most likely attributed to the differences in imposed force distributions. The ABFM-2W accounts for shear in the force projection, concentrating the force in the upper half of the disk where velocities are

higher. As a result, the ABFM-1W imposes a stronger loading in the lower part of the disk than the ABFM-2W, which leads to increased turbulence intensities in these areas.

5.3.3. Uniform Inflow at 20m/s

The impact of the turbine operating conditions on the wake characteristics will now be investigated. At $5 \frac{m}{s}$ and $10.5 \frac{m}{s}$, the turbine operates with similar thrust and power coefficients, and no significant differences in wake behaviour is observed. However, at $20 \frac{m}{s}$, the differences in the wake profiles are substantial. The analysis will focus on the uniform inflow case, as the differences between the uniform and sheared wakes were already presented in subsection 5.3.2.

Several notable differences with respect to the $10.5 \frac{m}{s}$ case can be observed from the instantaneous velocity profile of the wakes, shown in Figure 5.24. Compared to Figure 5.13, the wake is significantly harder to distinguish from the ambient flow. This is due to the turbine operating at a low thrust coefficient, and consequently, low induction. At $10.5 \frac{m}{s}$, the ABFM-2W showed a clear wake breakdown, whereas the instabilities in Figure 5.24 do not evolve into turbulent wake breakdown. This is a result of the relatively smaller velocity deficit between the wake and the ambient flow, which leads to a reduced turbulence production.

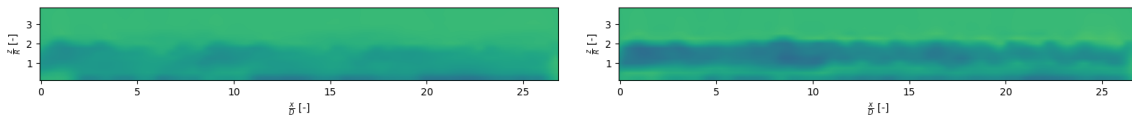


Figure 5.24: Instantaneous velocity profile downstream of the turbine for a uniform inflow profile of $20 \frac{m}{s}$. Left: ABFM-1W, Right: ABFM-2W

The wake of the ABFM-2W is noticeably deeper than that of the ABFM-1W. This difference is also evident in the time-averaged axial velocity profiles in Figure 5.25. For the ABFM-1W, the smearing artifacts appear less severe than in the $10.5 \frac{m}{s}$ case show in Figure 5.14. These smearing artifacts are caused by a radial velocity gradient resulting from the force projection method. Since the induction of the rotor is significantly reduced at $U_0 = 20 \frac{m}{s}$, this radial velocity gradient is also lower, which limits the impact of smearing.

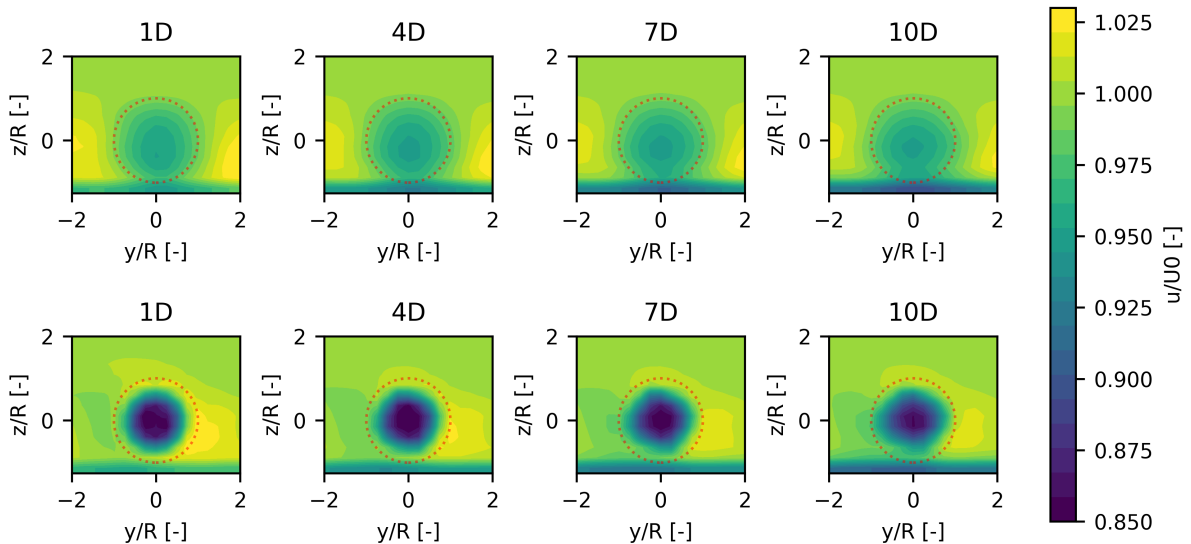


Figure 5.25: Time-averaged non-dimensional axial velocity downstream of the turbine at four distinct planes for a uniform inflow at $20 \frac{m}{s}$. The rotor disk is indicated by the dotted line. Top: ABFM-1W, Bottom: ABFM-2W

For the ABFM-2W, the wakes look fundamentally different from the $10.5 \frac{m}{s}$ case shown in Figure 5.14. The wake of the ABFM-2W is significantly deeper than that of the ABFM-1W and its radius appears

to be smaller than the rotor radius. This is further illustrated in Figure 5.26, which shows the axial velocity profiles in vertical direction for $\frac{y}{R} = 0$. Here, the differences with Figure 5.16 become even more apparent. To explain these differences, it is necessary to examine the force distribution imposed on the LES.

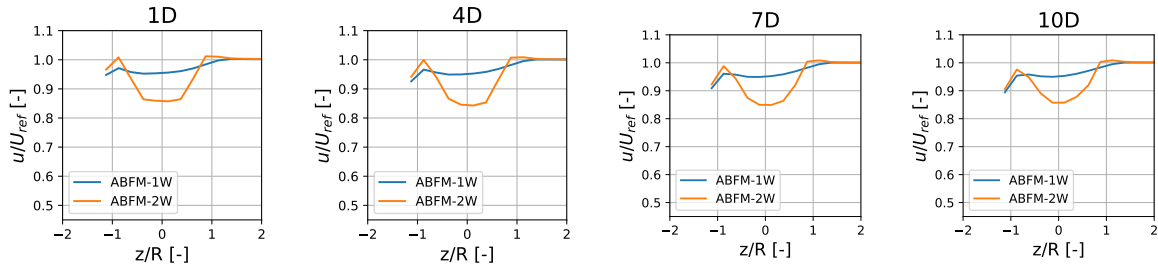


Figure 5.26: Time-averaged non-dimensional axial velocity profile along the vertical direction for $\frac{y}{R} = 0$ at multiple downstream locations for the ABFM-1W and the ABFM-2W for a uniform inflow at $20 \frac{m}{s}$.

At $U_0 = 20 \frac{m}{s}$, Figure 5.5 shows that the axial forces concentrate more on the inward section of the blade with respect to lower velocities. As a result, stronger induction occurs at the inner part of the rotor disk, leading to a locally more uniform wake. However, Figure 5.5 also indicates that at $U_0 = 20 \frac{m}{s}$, the axial forces become negative near the tip of the blade. This means that the blade will locally start acting like a propeller. Consequently, more momentum must be extracted by the inner part of the disk to compensate. This explains why the ABFM-2W wake is deeper and less wide than the ABFM-1W.

Next, the azimuthal velocity of the wake along the vertical direction at $\frac{y}{R} = 0$ is shown in Figure 5.27. Again, the difference in wake behaviour between the ABFM-1W and ABFM-2W is substantial. For the ABFM-1W, the wake rotation is almost negligible. Compared to Figure 5.17, the turbine operates at a similar power and rotational speed. The azimuthal force projected by the uniform AD model is thus the same as for the $10.5 \frac{m}{s}$ case, but the freestream velocity differs by almost a factor of two. As a result, the non-dimensional azimuthal velocity is significantly lower.

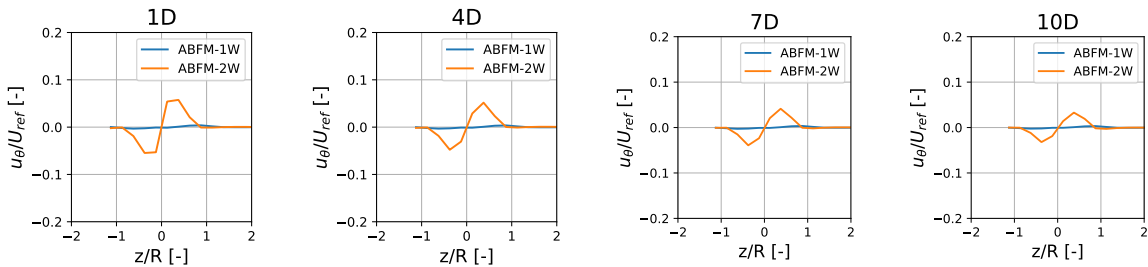


Figure 5.27: Time-averaged non dimensional azimuthal velocity profile along the vertical direction for $\frac{y}{R} = 0$ at multiple downstream locations for the ABFM-1W and the ABFM-2W for a uniform inflow at $20 \frac{m}{s}$.

The ABFM-2W, however, shows a different wake rotation behaviour. The ABFM-2W calculates the azimuthal velocity from Equation 3.5, where S_0 represents the solid body wake rotation term. As the rotor is operating far from the rated condition at $U_0 = 20 \frac{m}{s}$, this S_0 term dominates the azimuthal velocity, imposing solid-body rotation onto the wake. In Figure 5.27, this dominance is reflected in the shape of the azimuthal velocity profile. At rated velocity conditions, the azimuthal velocity is predominantly induced by the rotor circulation, which causes a large spike close to the root. This is clearly observed in Figure 5.16. However, in Figure 5.26, the azimuthal velocity close to the root is significantly flatter, caused by this solid-body rotation component. As a result, the azimuthal velocities are greater for larger radial coordinate.

As previously noted for Figure 5.24, the turbulence production is lower compared to $U_0 = 10.5 \frac{m}{s}$. This can also be seen in the turbulence intensity profile along the vertical direction at $\frac{y}{R} = 0$ in Figure 5.28.

The turbulence intensity remains below 4%, whereas values up to 10% were observed at $U_0 = 10.5 \frac{m}{s}$. This reduction is caused by a lower turbine thrust. This reduces the vorticity at the interface between the wake and the ambient flow. Furthermore, Figure 5.26 revealed that the root vortex is less prevalent, contributing to a greater wake stability.

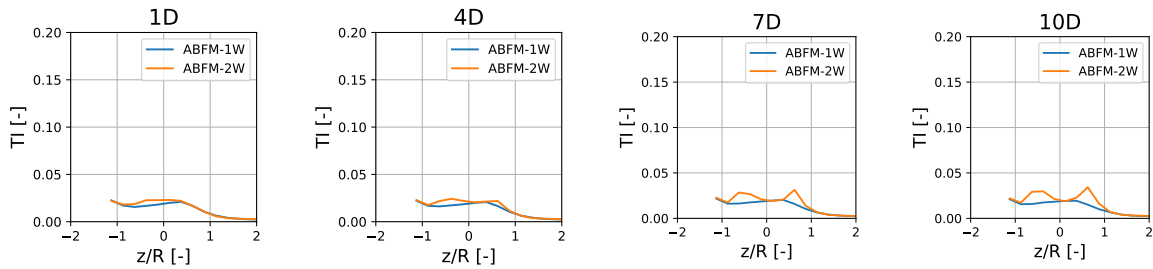


Figure 5.28: Time-averaged turbulence intensity along the vertical direction for $\frac{y}{R} = 0$ at multiple downstream locations for the ABFM-1W and the ABFM-2W for a uniform inflow at $20 \frac{m}{s}$.

5.4. Application to Turbines with a Partially Waked Inflow

Up until now, all inflow profiles have been defined in a controlled manner to allow for a straightforward validation of the results. However, in reality, the inflow experienced by a turbine is highly chaotic. Especially within a wind farm, the turbine inflow is often governed by the wake of another turbine. This section therefore evaluates the loading for a turbine operating in a partial wake.

This partially waked inflow is obtained by repeating simulation U105 from Table 3.2 with a second turbine in the domain. This second turbine is positioned five diameters downstream of the first and is offset half a diameter laterally. In this staggered configuration, part of the rotor disk is exposed to the wake of the upstream turbine, while the remainder experiences a relatively undisturbed ambient flow.

As a result, the inflow of this turbine will be highly heterogeneous and unsteady. This simulation therefore serves as a test to evaluate whether the ABFM-1W and ABFM-2W are capable of resolving these more chaotic and realistic inflows. As shown in section 5.3, the wake characteristics of the ABFM-1W and ABFM-2W are fundamentally different. This setup allows for assessing the influence of the wake characteristics on the resulting load distributions. In reality, the stability of the atmosphere also has a significant impact on the wake characteristics, but this effect is beyond the scope of the current study. Instead, this section aims to qualitatively demonstrate that the force projection method can significantly influence the load assessment of a turbine.

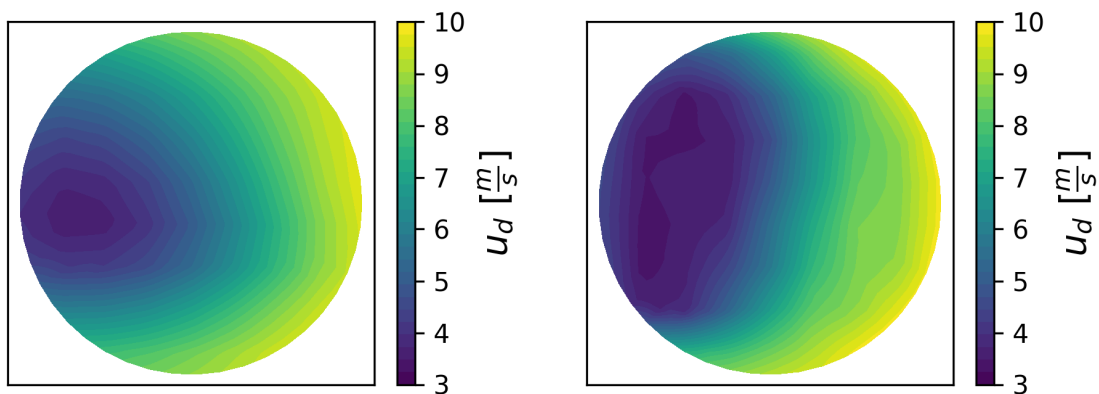


Figure 5.29: Distribution of the time-averaged disk velocity for a wind turbine placed 5D downstream of another turbine and offset 0.5D laterally for a uniform inflow of $10.5 \frac{m}{s}$. Left: ABFM-1W, Right: ABFM-2W

To understand the force distributions, it is helpful to first examine the disk velocity distribution experi-

enced by the downstream turbine. This velocity is obtained by averaging the velocity field in time. The results are shown in the left and right graphs of Figure 5.29, for the ABFM-1W and ABFM-2W, respectively. It can be seen that the projection method somewhat influences the velocity distribution, although the effect of the partial wake is clearly distinguishable for both cases.

On the left side of Figure 5.29, the ABFM-1W shows a gradual radial increase in disk velocity from the deepest point of the wake outward. Since the forces are modelled by a uniform AD, the radial velocity gradient is smooth and almost the same in every direction. In contrast, the ABFM-2W actively couples the forces and velocities within the LES. This coupling causes the self-induction pattern of the rotor to adapt to the local flow. As a result, the rotor induction appears to concentrate in the waked area. Similar results were also obtained by Navarro Diaz et al.[49].

The impact of this non-uniform disk velocity on the force distributions becomes evident when examining the time-averaged axial forces, shown in the left and right graphs of Figure 5.30, for the ABFM-1W and ABFM-2W. The resemblance to Figure 5.29 is clear, regions with a higher velocity also exhibit greater axial forces. The exception is near the root and tip, where the force drops to zero due to the tip and root corrections.

The ABFM-1W captures the force distribution reasonably well, even though the turbine is represented by only uniform forces in the LES. This suggests that the self-induction pattern of the rotor is merely a secondary effect, and that the primary shape of the force distribution is governed by the turbine inflow. Nevertheless, accurately capturing local effects on the force distributions requires detailed knowledge of the disk velocity distribution. Here, the ABFM-2W shows two advantages over the ABFM-1W. First, section 5.3 demonstrated that the wake characteristics of the ABFM-2W are more realistic than those of the ABFM-1W. Second, the active coupling mechanism between the shape of the force distribution and disk velocity ensures that the ABFM-2W can capture the self-induction distribution of the waked turbine. Meanwhile, the uniform AD model of the ABFM-1W will always yield a uniform self-induction pattern.

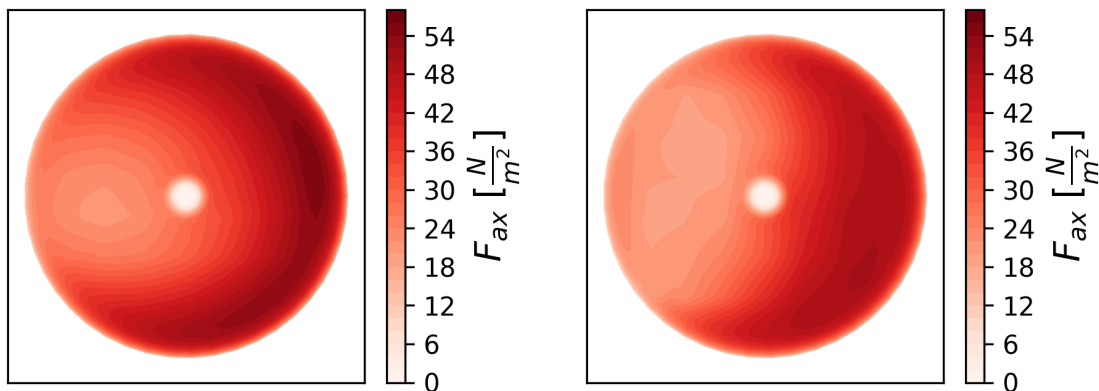


Figure 5.30: Distribution of the-time averaged axial force per unit rotor area for a wind turbine placed 5D downstream of another turbine and offset 0.5D laterally for a uniform inflow of $10.5 \frac{m}{s}$. Left: ABFM-1W, Right: ABFM-2W

The same analysis conducted for the axial forces can be repeated for the azimuthal forces. The shape of the azimuthal forces is shown in Figure 5.31. Compared to the uniform case shown in Figure 4.26, the loading now correlates with the non-uniform disk velocity shown in Figure 5.29, with higher forces occurring in regions of higher velocity and lower forces in regions of lower velocity. The influence of the wake seems more pronounced for the ABFM-2W, resulting in a low loading on the left side of the disk. For the ABFM-1W, the wake of the upstream turbine is more diffuse, as was shown in Figure 5.15. As a result, the ABFM-1W predicts somewhat higher loading in this waked region and a reduced peak loading. The results comply with the observed disk velocity distributions in Figure 5.29.

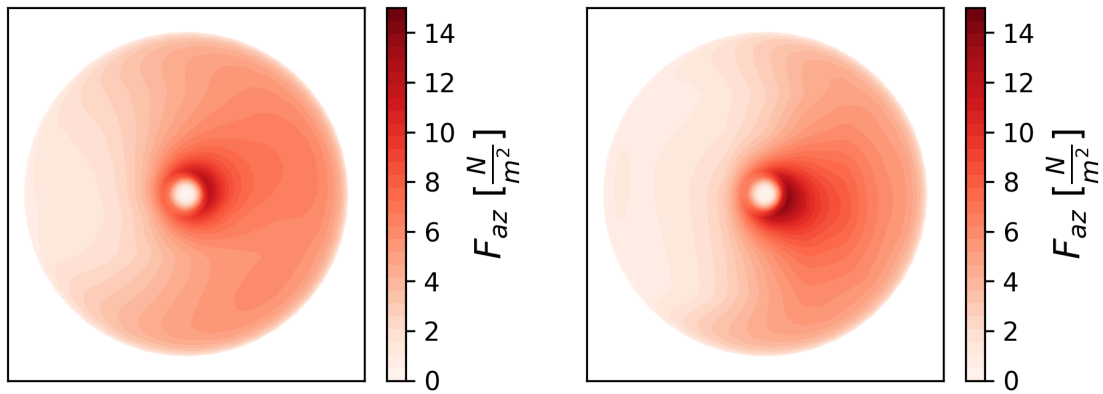


Figure 5.31: Distribution of the time-averaged azimuthal force per unit rotor area for a wind turbine placed 5D downstream of another turbine and offset 0.5D laterally for a uniform inflow of $10.5 \frac{m}{s}$. Left: ABFM-1W, Right: ABFM-2W

Until now, only the time-averaged forces have been shown. However, the wake is highly chaotic, causing temporal fluctuations in the forces. This is illustrated by considering the standard deviation in time of several quantities across the rotor disk of the downstream turbine. The standard deviation of the disk velocity is shown in the left and right graph of Figure 5.32, for the ABFM-1W and ABFM-2W, respectively. Both models show higher standard deviation in the lower part of the disk, due to a locally slightly deeper wake, as was shown in Figure 5.16.

More importantly, the shape of the distribution is significantly different for the ABFM-1W and the ABFM-2W. For the ABFM-1W, the wake is artificially diffuse, as was already observed in Figure 5.15, causing a relatively smooth distribution of the standard deviation over the disk. The ABFM-2W, on the other hand, shows very sharp gradients at the edge of the wake. The exact location of the wake is not constant, but oscillates on time. Since the ABFM-2W exhibits such a steep transition between the wake and the ambient flow, some points of the waked turbine experience alternating high ambient and low wake velocities. This results in a distinct ring of high standard deviation, located at the edge of the wake, as shown in Figure 5.32. For the ABFM-1W, this effect cannot be distinguished, as the wake is excessively smeared.

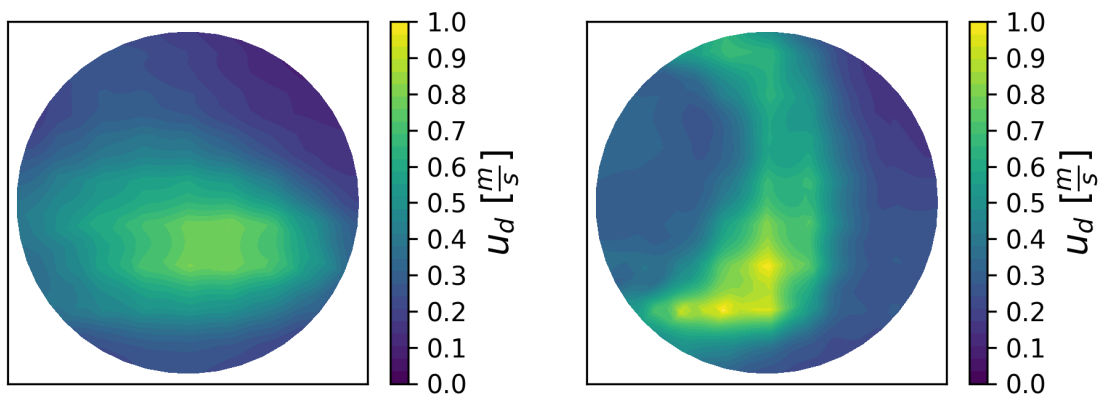


Figure 5.32: Distribution of the temporal standard deviation of the axial disk velocity for a wind turbine placed 5D downstream of another turbine and is offset 0.5D laterally, for a uniform inflow of $10.5 \frac{m}{s}$. Left: ABFM-1W, Right: ABFM-2W

The standard deviations for the forces are shown in Figure 5.33 for the axial forces and in Figure 5.34. In both figures, the left and right graph correspond to the ABFM-1W and ABFM-2W, respectively. For the axial forces in Figure 5.33, it is clear that the pattern is very similar to the standard deviation of the

disk velocity shown in Figure 5.32. This observation aligns with expectations, as Figure 5.30 previously demonstrated that changes in velocity directly influence the tangential force.

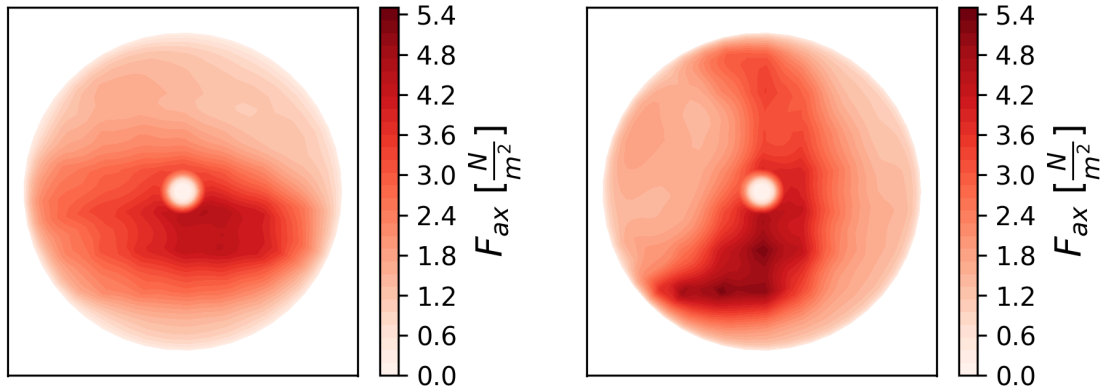


Figure 5.33: Distribution of the temporal standard deviation of the axial force per unit rotor area for a wind turbine placed 5D downstream of another turbine and is offset 0.5D laterally, for a uniform inflow of $105 \frac{m}{s}$. Left: ABFM-1W, Right: ABFM-2W

The pattern of the standard deviation of the velocity can still be distinguished in the standard deviation of the azimuthal forces shown in Figure 5.34, although high values are concentrate near the root. Figure 5.31 shows that for a large part of the disk the azimuthal force is quite low. Consequently, the standard deviation of the azimuthal force is also low in this region. High standard deviation in force therefore occur in regions where both the mean force and the standard deviation of the velocity are high.

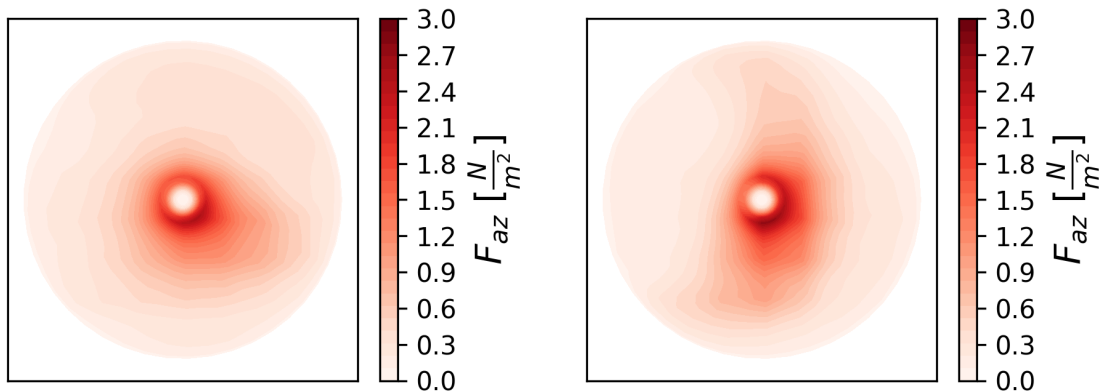


Figure 5.34: Distribution of the temporal standard deviation of the azimuthal force per unit rotor area for a wind turbine placed 5D downstream of another turbine and is offset 0.5D laterally, for a uniform inflow of $105 \frac{m}{s}$. Left: ABFM-1W, Right: ABFM-2W

Comparison of the standard deviations between the ABFM-1W to the ABFM-2W reveals significant differences, even though the mean loading presented in Figure 5.30 and Figure 5.31 exhibits similar trends. It can thus be concluded that both models capture the average dynamics of the partially waked inflow, but accurately resolving the wake characteristics is essential to correctly capture higher order statistical moments of the time series of the force distributions. In section 5.3, it was shown that the ABFM-1W exhibits excessive flow smoothing due to numerical smearing effects. This effect was not observed for the ABFM-2W. Furthermore, the ABFM-2W employs a more physical force projection. Therefore, for accurate simulation of a turbine under waked conditions, it is recommended to employ the ABFM-2W.

6

Conclusion

In this thesis, it was explored whether the blade force distributions of a turbine could be estimated from LES, with limited knowledge of the turbine geometry. This was achieved by implementing an Analytical Body Force Model (ABFM). The ABFM computed the axial and azimuthal force distributions based on the turbine operating conditions. Coupling the ABFM to the LES posed several challenges.

First, the turbine conditions needed to be determined. These were related to the freestream velocity using the characteristic turbine curves. However this velocity cannot be directly sampled in the LES due to turbulence and induction effects. Instead, a calibration simulation was performed to generate a lookup table relating these quantities to the average wind power over the disk, $\overline{\rho_a u_d^3}$.

Next, the ABFM was coupled to the LES, using both one-way coupling (ABFM-1W) and two-way coupling (ABFM-2W). For both models, the velocity from the LES was interpolated onto a polar grid defined on the rotor disk, using trilinear interpolation. For the ABFM-2W, the resulting force distribution was projected back onto the LES by smearing the forces along the axial direction using a 1D Gaussian kernel, then distributing them onto the LES grid based on trilinear interpolation weights. In contrast, the projected forces of the ABFM-1W were obtained from a uniform Actuator Disk model.

With this setup, the ABFM-1W and ABFM-2W were able to accurately resolve the force distributions for a variety of cases. For uniform and sheared inflows, the ABFM-2W compared closely to BEM for the time-averaged axial and azimuthal force coefficients. The ABFM-1W also successfully reconstructed the axial forces. Azimuthal force predictions were consistently less accurate than those of the ABFM-2W, though still reasonable. Both the ABFM-1W and ABFM-2W partially captured the azimuthal variation in loading for sheared flows. Here, the average shear effect was well represented, but changes in the loading due to oscillations in the thrust and power at the sub-revolution timescale could not be resolved. Again, the agreement with BEM was closer for the ABFM-2W than for the ABFM-1W.

The resulting wakes of the ABFM-1W and ABFM-2W showed very distinct features. Due to the implementation of the ABFM-1W, the wake was identical to that of the underlying uniform Actuator Disk model. Employing the ABFM-2W instead showed a clear improvement in wake characteristics. The ABFM-2W not only resolved the root vortex and radial induction pattern, but also avoided numerical smoothing. This is in contrast to the ABFM-1W, which showed an artificially diffuse wake caused by the 3D Gaussian projection kernel.

The most complex case evaluated was a turbine experiencing a partially waked inflow. Both the ABFM-1W and ABFM-2W resolved the time-averaged effect of the wake on the loading, showing significantly lower forces in the waked region. However, only the ABFM-2W accurately captured the standard deviation of these forces. A clear ring of high standard deviation was observed on the rotor disk, near the edge of the incoming wake, as these regions would alternately experience waked and ambient conditions. For the ABFM-1W, the wake of the upstream turbine was too diffuse to resolve this effect.

Several limitations of the proposed methodology were also experienced. These limitations and possible solutions that could be investigated in future work, are described in chapter 7.

7

Recommendations for Future Work

In this thesis it was shown that it is possible to obtain the blade loads from Analytical Body Force Models coupled to a LES for a variety of cases. Especially in industry, where turbine geometries are often unknown, this approach promises to be a good alternative. Still, a variety of challenges and limitations were encountered during the project, which could be further investigated in future work.

First of all, it was found that it was hard to correctly sample the disk velocity from the LES, while the accuracy of the force distributions depends heavily on this step. For the ABFM-1W the smearing effects of the uniform AD model caused a radial gradient in the disk velocity. It is expected that this can be prevented by applying the same smearing methodology of subsection 3.3.3, but then for a uniform force distribution.

Still, for the ABFM-2W the disk velocity near the edge of the disk was not captured either. The main cause here was that near the edge of the disk, the velocity is interpolated using points outside of the disk, which causes a positive bias in the velocity. It is recommended to investigate other interpolation approaches which do not sample outside of the disk. However, turbulent fluctuations should still be captured in a realistic manner. It is not directly clear how to meet both these requirements under all conditions.

Another source of error was the freestream velocity calibration. Obtaining the turbine thrust, power and average induction factor by measuring only the average available wind power on the disk, $\overline{\rho u_d^3}$ was found to work decently, but errors of up to 5% were still regularly encountered. As these values are used as a direct input of the ABFM, these errors propagate into the accuracy of the resolved force distributions. It should therefore be investigated whether this calibration can be done in a different way to give more reliable results. If the calibration is altered, the effect of wind shear should also be considered more carefully. Since the current approach only makes use of a disk averaged value, it is blind to changes in thrust and power over a single rotor revolution. Possibly, instead of taking the average over the entire disk, the available wind power could be calculated at the location of the blades to better capture the heterogeneity of the problem.

Taking the blade location into account can also increase accuracy in other places in the model. Currently, the ABFM-2W still operates as an AD model, such that the LES does not see the influence of separate blades. Navarro Diaz et al.[49] already showed that the ABFM can be used in a similar setup as the approach of this work to perform Actuator Line computations. However, AL methods are generally infeasibly expensive for industry purposes. It is therefore suggested to transform the load projection into an Actuator Sector approach. For as far as known, this has not yet been done with analytical body force models, but it promises to further increase the accuracy of the LES by capturing some of the vortical structures at the tip. Admittedly, this approach only makes sense if the timestep of the LES is small enough to resolve individual revolutions. This requirement might be more expensive than the CFL stability requirement, especially at the resolution of $\Delta_{LES} = \frac{D}{8}$ used in this work, thereby increasing computational cost.

Further modifications could also be made to the analytical model itself to better capture complicated inflows. It was seen that the predicted loads are significantly worse if the rotor is operating at low thrust and power coefficient, but it might be possible to correct for this. In addition, the model currently does not account for radial flow along the turbine, which limits its application for cases with a high rotor yaw. Inherently BEM can also not directly deal with yaw, but additional correction models are available. As the behaviour of the ABFM is similar to BEM, it might be possible to adopt those models for use in the ABFM.

All of the above proposed changes help the model to better capture the aerodynamics of the rotor. However, in reality the turbine is also impacted by a variety of different effects. It is expected that a more realistic simulation can be performed by coupling several modules together, such as is done in the OpenFAST software. Coupling the aerodynamic forces with a simple beam module could already provide more insights on aero-elastic effects of the turbines. Similarly, the implementation of a turbine controller can greatly effect the total thrust and power that the turbine generates, which in turn effects the load distributions. Including a turbine controller can therefore be important for dealing with changing inflow conditions, such as changes in wind speed and direction.

A last recommendation is further validation of the model. For uniform and sheared inflows, the load distributions could be compared to a BEM reference. However, for investigating the wake dynamics and evaluating the forces on a partially waked turbine, BEM could no longer provide validation data. In this case, results from higher-fidelity models, such as Actuator Line computations, would be desired. Unfortunately, it was not feasible to obtain these results within the time frame of this thesis. As such, the comparison of those models under these conditions was mostly performed in a qualitative way.

References

- [1] Dries Allaerts and Johan Meyers. “Large eddy simulation of a large wind-turbine array in a conventionally neutral atmospheric boundary layer”. In: *Physics of Fluids* 27.6 (June 2015). ISSN: 1089-7666. DOI: 10.1063/1.4922339.
- [2] John Anderson. *Fundamentals of Aerodynamics*. Mar. 16, 2016.
- [3] H. Asmuth. “Efficient Large-eddy Simulation for Wind Energy Applications”. PhD thesis. Uppsala Universitet, Apr. 28, 2022.
- [4] Mehmet Bakırcı and Sezayi Yılmaz. “Theoretical and computational investigations of the optimal tip-speed ratio of horizontal-axis wind turbines”. In: *Engineering Science and Technology, an International Journal* 21.6 (Dec. 2018), pp. 1128–1142. ISSN: 2215-0986. DOI: 10.1016/j.jestech.2018.05.006.
- [5] A. Betz. “Schraubenpropeller mit Giringstem Energieverlust”. In: *Göttingen Narichten* (1919).
- [6] James Bleeg et al. “Wind Farm Blockage and the Consequences of Neglecting Its Impact on Energy Production”. In: *Energies* 11.6 (June 2018), p. 1609. ISSN: 1996-1073. DOI: 10.3390/en11061609.
- [7] Daniel C. Bratton and Carole A. Womeldorf. “The Wind Shear Exponent: Comparing Measured Against Simulated Values and Analyzing the Phenomena That Affect the Wind Shear”. In: *ASME 2011 5th International Conference on Energy Sustainability, Parts A, B, and C*. ES2011. ASMEDC, Jan. 2011. DOI: 10.1115/es2011-54823.
- [8] Maarten J. van den Broek et al. “Dynamic wind farm flow control using free-vortex wake models”. In: *Wind Energy Science* 9.3 (Mar. 2024), pp. 721–740. ISSN: 2366-7451. DOI: 10.5194/wes-9-721-2024.
- [9] A. R. Brown et al. “Large eddy simulation of the diurnal cycle of shallow cumulus convection over land”. In: *Quarterly Journal of the Royal Meteorological Society* 128.582 (Apr. 2002), pp. 1075–1093. ISSN: 1477-870X. DOI: 10.1256/003590002320373210.
- [10] Tony L Burton et al. *Wind Energy Handbook*. John Wiley & Sons, 2001. ISBN: 9781119451099.
- [11] CBS. “Nearly half the electricity produced in the Netherlands is now renewable”. In: *Centraal Bureau voor de Statistiek* (Mar. 7, 2024).
- [12] Przemek Chojecki. “What is Moore’s Law? Is it Dead?” In: *builtin* (Sept. 17, 2023).
- [13] Matthew J. Churchfield et al. “An Advanced Actuator Line Method for Wind Energy Applications and Beyond”. In: *35th Wind Energy Symposium* (Jan. 2017). DOI: 10.2514/6.2017-1998.
- [14] Paolo Congedo and Maria Grazia De Giorgi. “Optimizing of a wind turbine rotor by CFD modeling”. In: *2008 ANSYS Italian Conference*. Oct. 2008.
- [15] Nirav Dangi et al. “The effect of turbulent coherent structures in atmospheric flow on wind turbine loads”. In: *Renewable Energy* 241 (Mar. 2025), p. 122248. ISSN: 0960-1481. DOI: 10.1016/j.renene.2024.122248.
- [16] Jean M. Delery. “Aspects of vortex breakdown”. In: *Progress in Aerospace Sciences* 30.1 (Jan. 1994), pp. 1–59. ISSN: 0376-0421. DOI: 10.1016/0376-0421(94)90002-7.
- [17] Mahmoud Elgendi et al. “A review of wind turbines in complex terrain”. In: *International Journal of Thermofluids* 17 (Feb. 2023), p. 100289. ISSN: 2666-2027. DOI: 10.1016/j.ijft.2023.100289.
- [18] Dennis Elliott, Marc Schwartz, and George Scott. “Wind Resource Base”. In: *Encyclopedia of Energy*. Elsevier, 2004, pp. 465–479. ISBN: 9780121764807. DOI: 10.1016/b0-12-176480-x/00335-1.
- [19] Lucía Fernández. “Share of electricity generation from wind energy sources worldwide from 2010 to 2023”. In: *Statista* (June 24, 2024).

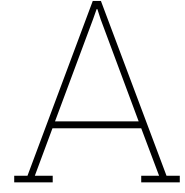
- [20] Genesal Energy. *Efficient Energy with Wind Power*. URL: <https://genesalenergy.com/en/applications/wind-farms/> (visited on 12/09/2024).
- [21] Abhimanyu Ghoshal. "Colossal 20-MW wind turbine is the largest on the planet (for now)". In: *New Atlas* (Sept. 4, 2024).
- [22] H. Glauert. "Airplane propellers". In: *Durand 4* (1935), pp. 169–310.
- [23] Hans Hersbach et al. "The ERA5 global reanalysis". In: *Quarterly Journal of the Royal Meteorological Society* 146.730 (June 2020), pp. 1999–2049. ISSN: 1477-870X. DOI: 10.1002/qj.3803.
- [24] T. Heus et al. "Formulation of and numerical studies with the Dutch Atmospheric Large-Eddy Simulation (DALES)". In: *Geoscientific Model Development Discussion* (Feb. 2010). DOI: 10.5194/gmdd-3-99-2010.
- [25] T. Heus et al. "Formulation of the Dutch Atmospheric Large-Eddy Simulation (DALES) and overview of its applications". In: *Geoscientific Model Development* 3.2 (Sept. 2010), pp. 415–444. ISSN: 1991-9603. DOI: 10.5194/gmd-3-415-2010.
- [26] Wei Huang, Rongjiang Tang, and Huihuan Ma. "The review of Vortex lattice method for offshore wind turbines". In: *Renewable Energy* 236 (Dec. 2024), p. 121450. ISSN: 0960-1481. DOI: 10.1016/j.renene.2024.121450.
- [27] IEA Wind Task 37. *IEA-15-240-RWT Monopile Configuration*. <https://github.com/IEAWindSystems/IEA-15-240-RWT/tree/master/OpenFAST/IEA-15-240>. Accessed: 2025-06-01. 2020.
- [28] Innovation Quarter. *Terugblij 2022 - Jaarverslag InnovationQuarter*. Apr. 21, 2023.
- [29] International Civil Aviation Organization. *Manual of the ICAO Standard Atmosphere*. ICAO Doc 7488-CD. Montreal, Canada, 1993.
- [30] IRENA. *Renewable Power Generation Costs in 2023*. 2024. ISBN: 978-92-9260-621-3.
- [31] M P van der Laan et al. "A CFD code comparison of wind turbine wakes". In: *Journal of Physics: Conference Series* 524 (June 2014), p. 012140. ISSN: 1742-6596. DOI: 10.1088/1742-6596/524/1/012140.
- [32] M. P. van der Laan et al. "Faster wind farm AEP calculations with CFD using a generalized wind turbine model". In: *Journal of Physics: Conference Series* 2265.2 (May 2022), p. 022030. ISSN: 1742-6596. DOI: 10.1088/1742-6596/2265/2/022030.
- [33] M. Paul van der Laan et al. "Thek- ϵ -fPmodel applied to double wind turbine wakes using different actuator disk force methods: Thek- ϵ -fPmodel applied to double wind turbine wakes". In: *Wind Energy* 18.12 (Oct. 2014), pp. 2223–2240. ISSN: 1095-4244. DOI: 10.1002/we.1816.
- [34] J. Gordon Leishman. "Aerodynamics of Horizontal Axis Wind Turbines". In: *Advances in Wind Energy Conversion Technology*. Springer Berlin Heidelberg, 2011, pp. 1–69. ISBN: 9783540882589. DOI: 10.1007/978-3-540-88258-9_1.
- [35] Mads H. Aa. Madsen et al. "CFD-based curved tip shape design for wind turbine blades". In: *Wind Energy Science* 7.4 (July 2022), pp. 1471–1501. ISSN: 2366-7451. DOI: 10.5194/wes-7-1471-2022.
- [36] Luis A. Martínez-Tossas, Matthew J. Churchfield, and Stefano Leonardi. "Large eddy simulations of the flow past wind turbines: actuator line and disk modeling: LES of the flow past wind turbines: actuator line and disk modeling". In: *Wind Energy* 18.6 (Apr. 2014), pp. 1047–1060. ISSN: 1095-4244. DOI: 10.1002/we.1747.
- [37] L. A. Martínez-Tossas, M. J. Churchfield, and C. Meneveau. "Optimal smoothing length scale for actuator line models of wind turbine blades based on Gaussian body force distribution". In: *Wind Energy* 20.6 (Jan. 2017), pp. 1083–1096. ISSN: 1099-1824. DOI: 10.1002/we.2081.
- [38] Pier Francesco Melani et al. "An insight into the capability of the actuator line method to resolve tip vortices". In: *Wind Energy Science* 9.3 (Mar. 2024), pp. 601–622. ISSN: 2366-7451. DOI: 10.5194/wes-9-601-2024.
- [39] Hang Meng, Fue-Sang Lien, and Li Li. "Elastic actuator line modelling for wake-induced fatigue analysis of horizontal axis wind turbine blade". In: *Renewable Energy* 116 (Feb. 2018), pp. 423–437. ISSN: 0960-1481. DOI: 10.1016/j.renene.2017.08.074.

- [40] Rick Merritt. “Why GPUs Are Great for AI”. In: *NVIDIA* (Dec. 4, 2023).
- [41] Alexander R. Meyer Forsting, Georg Raimund Pirrung, and Néstor Ramos-García. “A vortex-based tip/smearing correction for the actuator line”. In: *Wind Energy Science* 4.2 (June 2019), pp. 369–383. ISSN: 2366-7451. DOI: 10.5194/wes-4-369-2019.
- [42] Robert F. Mikkelsen. *Actuator Disc Methods Applied to Wind Turbines*. June 3, 2003. ISBN: 87-7475-296-0.
- [43] Charles Mockett. “A comprehensive study of detached-eddy simulation”. PhD. Technische Universität Berlin, 2009. DOI: <https://doi.org/10.14279/depositonce-2305>.
- [44] Mohammad Mehdi Mohammadi et al. “An actuator sector model for wind power applications: a parametric study”. In: *Wind Energy Science* 9.6 (June 2024), pp. 1305–1321. ISSN: 2366-7451. DOI: 10.5194/wes-9-1305-2024.
- [45] Mohammad Mehdi Mohammadi et al. “An aeroelastic coupling of an actuator sector model with OpenFAST in atmospheric flows”. In: *Journal of Physics: Conference Series* 2767.2 (June 2024), p. 022037. ISSN: 1742-6596. DOI: 10.1088/1742-6596/2767/2/022037.
- [46] P.J. Moriarty and A.C.Hansen. *AeroDyn Theory Manual*. Jan. 2005.
- [47] W. Munters and J. Meyers. “An optimal control framework for dynamic induction control of wind farms and their interaction with the atmospheric boundary layer”. In: *Philosophical Transactions of the Royal Society A: Mathematical, Physical and Engineering Sciences* 375.2091 (Mar. 2017), p. 20160100. ISSN: 1471-2962. DOI: 10.1098/rsta.2016.0100.
- [48] Jörn Nathan et al. “Analysis of the swept actuator line method”. In: *E3S Web of Conferences* 5 (2015). Ed. by Matthew J. Churchfield, p. 01001. ISSN: 2267-1242. DOI: 10.1051/e3sconf/20150501001.
- [49] Gonzalo Pablo Navarro Diaz et al. “Actuator line model using simplified force calculation methods”. In: *Wind Energy Science* 8.3 (Mar. 2023), pp. 363–382. ISSN: 2366-7451. DOI: 10.5194/wes-8-363-2023.
- [50] NREL. *OpenFAST*. Version v4.0.2. July 2024. DOI: <https://doi.org/10.5281/zenodo.14847846>. URL: <https://doi.org/10.5281/zenodo.14847846>.
- [51] M. de Oliveira, R.C. Puraca, and B.S. Carmo. “Blade-resolved numerical simulations of the NREL offshore 5 MW baseline wind turbine in full scale: A study of proper solver configuration and discretization strategies”. In: *Energy* 254 (Sept. 2022), p. 124368. ISSN: 0360-5442. DOI: 10.1016/j.energy.2022.124368.
- [52] David A. Peters and Cheng Jian He. “Correlation of Measured Induced Velocities with a Finite- \square State Wake Model”. In: *Journal of the American Helicopter Society* 36.3 (July 1991), pp. 59–70. ISSN: 2161-6027. DOI: 10.4050/jahs.36.59.
- [53] Fernando Porté-Agel, Yu-Ting Wu, and Chang-Hung Chen. “A Numerical Study of the Effects of Wind Direction on Turbine Wakes and Power Losses in a Large Wind Farm”. In: *Energies* 6.10 (Oct. 2013), pp. 5297–5313. ISSN: 1996-1073. DOI: 10.3390/en6105297.
- [54] Fernando Porté-Agel et al. “Large-eddy simulation of atmospheric boundary layer flow through wind turbines and wind farms”. In: *Journal of Wind Engineering and Industrial Aerodynamics* 99.4 (Apr. 2011), pp. 154–168. ISSN: 0167-6105. DOI: 10.1016/j.jweia.2011.01.011.
- [55] L. Prandtl. “Tragflügeltheorie. I. Mitteilung”. In: *Nachrichten von der Gesellschaft der Wissenschaften zu Göttingen, Mathematisch-Physikalische Klasse* 1918 (1918), pp. 451–477. URL: <http://eudml.org/doc/59036>.
- [56] Raj K. Rai et al. “A code-independent generalized actuator line model for wind farm aerodynamics over simple and complex terrain”. In: *Environmental Modelling & Software* 94 (Aug. 2017), pp. 172–185. ISSN: 1364-8152. DOI: 10.1016/j.envsoft.2017.05.001.
- [57] P.A. Costa Rocha et al. “ k - ω SST (shear stress transport) turbulence model calibration: A case study on a small scale horizontal axis wind turbine”. In: *Energy* 65 (Feb. 2014), pp. 412–418. ISSN: 0360-5442. DOI: 10.1016/j.energy.2013.11.050.
- [58] Pierre Sagaut. *Large Eddy Simulations for Incompressible Flows*. Springer-Verlag, 2006. ISBN: 3540263446. DOI: 10.1007/b137536.

- [59] B. Sanderse, S.P. van der Pijl, and B. Koren. "Review of computational fluid dynamics for wind turbine wake aerodynamics". In: *Wind Energy* 14.7 (Feb. 2011), pp. 799–819. ISSN: 1099-1824. DOI: 10.1002/we.458.
- [60] Jérôme Schalkwijk et al. "High-Performance Simulation of Turbulent Clouds on a Desktop PC Exploiting the GPU". In: *American Meteorological Society* (Mar. 1, 2012).
- [61] Jörg Schneemann et al. "Offshore wind farm global blockage measured with scanning lidar". In: *Wind Energy Science* 6.2 (Apr. 2021), pp. 521–538. ISSN: 2366-7451. DOI: 10.5194/wes-6-521-2021.
- [62] Michael Schollenberger, Thorsten Lutz, and Ewald Krämer. "Boundary Condition Based Actuator Line Model to Simulate the Aerodynamic Interactions at Wingtip Mounted Propellers". In: *New Results in Numerical and Experimental Fluid Mechanics XII* (Sept. 2019), pp. 608–618. ISSN: 1860-0824. DOI: 10.1007/978-3-030-25253-3_58.
- [63] Wen Zhong Shen, Jens Nørkær Sørensen, and Robert Mikkelsen. "Tip Loss Correction for Actuator/Navier–Stokes Computations". In: *Journal of Solar Energy Engineering* 127.2 (Apr. 2005), pp. 209–213. ISSN: 1528-8986. DOI: 10.1115/1.1850488.
- [64] Wen Zhong Shen, Jian Hui Zhang, and Jens Nørkær Sørensen. "The Actuator Surface Model: A New Navier–Stokes Based Model for Rotor Computations". In: *Journal of Solar Energy Engineering* 131.1 (Jan. 2009). ISSN: 1528-8986. DOI: 10.1115/1.3027502.
- [65] WZ Shen, JN Sørensen, and Zhang. JH. "Actuator surface model for wind turbine flow computations". In: *European Wind Energy Conference and Exhibition*. May 7, 2007.
- [66] Michael Shives and Curran Crawford. "Mesh and load distribution requirements for actuator line CFD simulations". In: *Wind Energy* 16.8 (Aug. 2012), pp. 1183–1196. ISSN: 1099-1824. DOI: 10.1002/we.1546.
- [67] Jagdeep Singh and Jahrul M Alam. "Large-Eddy Simulation of Utility-Scale Wind Farm Sited over Complex Terrain". In: *Energies* 16.16 (Aug. 2023), p. 5941. ISSN: 1996-1073. DOI: 10.3390/en16165941.
- [68] Jayanarayanan Sitaraman, Dimitri J. Mavriplis, and Earl P. Duque. "Wind Farm simulations using a Full Rotor Model for Wind Turbines". In: *32nd ASME Wind Energy Symposium*. American Institute of Aeronautics and Astronautics, Jan. 2014. DOI: 10.2514/6.2014-1086.
- [69] H. Snel. "Survey of induction dynamics modeling within BEM-like codes - Dynamic inflow and yawed flow modeling revisited". In: *20th 2001 ASME Wind Energy Symposium* (Jan. 2001). DOI: 10.2514/6.2001-27.
- [70] J. N. Sørensen, W. Z. Shen, and X. Munduate. "Analysis of wake states by a full-field actuator disc model". In: *Wind Energy* 1.2 (Dec. 1998), pp. 73–88. ISSN: 1099-1824. DOI: 10.1002/(sici)1099-1824(199812)1:2<73::aid-we12>3.0.co;2-l.
- [71] Jens N Sørensen and Søren J Andersen. "Validation of analytical body force model for actuator disc computations". In: *Journal of Physics: Conference Series* 1618.5 (Sept. 2020), p. 052051. ISSN: 1742-6596. DOI: 10.1088/1742-6596/1618/5/052051.
- [72] Jens N. Sørensen. "Generalized analytical body force model for actuator disc computations of wind turbines". In: *Wind Energy Science* 8.6 (June 20, 2023), pp. 1017–1027. ISSN: 2366-7451. DOI: 10.5194/wes-8-1017-2023.
- [73] Jens Nørkær Sørensen. *General Momentum Theory for Horizontal Axis Wind Turbines*. Springer International Publishing, 2016. ISBN: 9783319221144. DOI: 10.1007/978-3-319-22114-4.
- [74] Jens Nørkær Sørensen and Gunner Christian Larsen. "A Minimalistic Prediction Model to Determine Energy Production and Costs of Offshore Wind Farms". In: *Energies* 14.2 (Jan. 2021), p. 448. ISSN: 1996-1073. DOI: 10.3390/en14020448.
- [75] Jens Nørkær Sørensen et al. "Analytical body forces in numerical actuator disc model of wind turbines". In: *Renewable Energy* 147 (Mar. 2020), pp. 2259–2271. ISSN: 0960-1481. DOI: 10.1016/j.renene.2019.09.134.

- [76] Jens Nørkær Sørensen and Wen Zhong Shen. “Numerical Modeling of Wind Turbine Wakes”. In: *Journal of Fluids Engineering* 124.2 (May 2002), pp. 393–399. ISSN: 1528-901X. DOI: 10.1115/1.1471361.
- [77] Rob Stoll et al. “Large-Eddy Simulation of the Atmospheric Boundary Layer”. In: *Boundary-Layer Meteorology* 177.2–3 (Aug. 2020), pp. 541–581. ISSN: 1573-1472. DOI: 10.1007/s10546-020-00556-3.
- [78] R C Storey, S E Norris, and J E Cater. “Modelling Turbine Loads during an Extreme Coherent Gust using Large Eddy Simulation”. In: *Journal of Physics: Conference Series* 524 (June 2014), p. 012177. ISSN: 1742-6596. DOI: 10.1088/1742-6596/524/1/012177.
- [79] R. C. Storey, S. E. Norris, and J. E. Cater. “An actuator sector method for efficient transient wind turbine simulation”. In: *Wind Energy* 18.4 (Mar. 2014), pp. 699–711. ISSN: 1099-1824. DOI: 10.1002/we.1722.
- [80] R.C. Storey, J.E. Cater, and S.E. Norris. “Large eddy simulation of turbine loading and performance in a wind farm”. In: *Renewable Energy* 95 (Sept. 2016), pp. 31–42. ISSN: 0960-1481. DOI: 10.1016/j.renene.2016.03.067.
- [81] Roland B. Stull. *An Introduction to Boundary Layer Meteorology*. Springer Netherlands, 1988. ISBN: 9789400930278. DOI: 10.1007/978-94-009-3027-8.
- [82] Niels Troldborg. “Actuator Line Modeling of Wind Turbine Wakes”. PhD. Technical University of Denmark, Jan. 12, 2009.
- [83] Niels Troldborg et al. “Brief communication: How does complex terrain change the power curve of a wind turbine?” In: *Wind Energy Science* 7.4 (July 2022), pp. 1527–1532. ISSN: 2366-7451. DOI: 10.5194/wes-7-1527-2022.
- [84] Takanori Uchida and Yuji Ohya. “Large-eddy simulation of turbulent airflow over complex terrain”. In: *Journal of Wind Engineering and Industrial Aerodynamics* 91.1–2 (Jan. 2003), pp. 219–229. ISSN: 0167-6105. DOI: 10.1016/s0167-6105(02)00347-1.
- [85] Whiffle. *Aspire Documentation*. Whiffle. Sept. 23, 2024.
- [86] Whiffle. *Whiffle solutions*. 2024. URL: <https://whiffle.nl/solutions/> (visited on 11/20/2024).
- [87] David C. Wilcox. *Turbulence Modeling for CFD*. 3rd ed. D C W Industries, 2006. ISBN: 978-1928729082.
- [88] R. E. Wilson and P B.S. Lissaman. *Applied aerodynamics of wind power machines*. Oregon State University, 1974.
- [89] Wind Europe. “Wind energy in Europe 2023 Statistics and the outlook for 2024-2030”. In: *Wind Europe* (Feb. 28, 2024).
- [90] Ka Wu and Fernando Porté-Agel. “Flow Adjustment Inside and Around Large Finite-Size Wind Farms”. In: *Energies* 10.12 (Dec. 2017), p. 2164. ISSN: 1996-1073. DOI: 10.3390/en10122164.
- [91] Yu-Ting Wu and Fernando Porté-Agel. “Large-Eddy Simulation of Wind-Turbine Wakes: Evaluation of Turbine Parametrisations”. In: *Boundary-Layer Meteorology* 138.3 (Dec. 2010), pp. 345–366. ISSN: 1573-1472. DOI: 10.1007/s10546-010-9569-x.
- [92] Yu-Ting Wu and Fernando Porté-Agel. “Modeling turbine wakes and power losses within a wind farm using LES: An application to the Horns Rev offshore wind farm”. In: *Renewable Energy* 75 (Mar. 2015), pp. 945–955. ISSN: 0960-1481. DOI: 10.1016/j.renene.2014.06.019.
- [93] Chi Yan and Cristina L. Archer. “Assessing compressibility effects on the performance of large horizontal-axis wind turbines”. In: *Applied Energy* 212 (Feb. 2018), pp. 33–45. ISSN: 0306-2619. DOI: 10.1016/j.apenergy.2017.12.020.
- [94] Xiaolei Yang, Maggie Pakula, and Fotis Sotiropoulos. “Large-eddy simulation of a utility-scale wind farm in complex terrain”. In: *Applied Energy* 229 (Nov. 2018), pp. 767–777. ISSN: 0306-2619. DOI: 10.1016/j.apenergy.2018.08.049.
- [95] Ziyang Yu et al. “Aeroelastic Performance Analysis of Wind Turbine in the Wake with a New Elastic Actuator Line Model”. In: *Water* 12.5 (Apr. 2020), p. 1233. ISSN: 2073-4441. DOI: 10.3390/w12051233.

- [96] M. H. Zhang. *Appendix II: IEC Classification of Wind Turbines*. In: *Wind Resource Assessment and Micro-Siting: Science and Engineering*. Wiley, June 2015, pp. 269–270. ISBN: 9781118900116. DOI: 10.1002/9781118900116.app2.
- [97] Ye Zhang, Shuanghou Deng, and Xiaofang Wang. “RANS and DDES simulations of a horizontal-axis wind turbine under stalled flow condition using OpenFOAM”. In: *Energy* 167 (Jan. 2019), pp. 1155–1163. ISSN: 0360-5442. DOI: 10.1016/j.energy.2018.11.014.
- [98] Ye Zhang, Alexander van Zuijlen, and Gerard van Bussel. “Massively separated turbulent flow simulation around non-rotating MEXICO blade by means of RANS and DDES approaches in OpenFOAM”. In: *33rd AIAA Applied Aerodynamics Conference*. American Institute of Aeronautics and Astronautics, June 2015. DOI: 10.2514/6.2015-2716.
- [99] Dan Zhao et al. “Aerodynamics of horizontal axis wind turbines and wind farms”. In: *Wind Turbines and Aerodynamics Energy Harvesters*. Elsevier, 2019, pp. 431–461. ISBN: 9780128171356. DOI: 10.1016/b978-0-12-817135-6.09994-4.



Understanding the ABFM Induction

The ABFM is developed to be used for load calculations. However, as seen in subsection 3.1.2, the disk velocity $u_{d_{ABFM}}$ can explicitly be solved if the inflow is assumed to be homogeneous. As such, it is possible to use the ABFM to estimate the rotor induction factor if the freestream condition is known. In section A.1, it will be shown that the obtained induction is quite accurate for some cases, while it is significantly incorrect for other cases. It turns out that this plays a great role in achieving a successful coupling to the LES, which will be elaborated on in section A.2.

A.1. Induction Modeling using the ABFM

As presented in subsection 3.1.2, the homogeneous ABFM results in the system of equations of Equation 3.14 and Equation 3.15. If the turbine conditions, C_T , C_P , λ and U_0 are known, the system can be solved for q_0 and $u_{d_{ABFM}}$. As derived in section 3.1, the disk velocity can be obtained from Equation 3.17. Afterwards, the average induction factor, \bar{a} , can be found from Equation A.1.

$$\bar{a} = 1 - \frac{u_d}{U_0} \quad (\text{A.1})$$

These equations will now be used to evaluate the $\bar{a} - C_T$ curve of an ideal turbine with no losses in the wake. In this case, 1D momentum theory can be used to obtain the reference solution as in Equation A.2. To calculate the induction from the ABFM, the C_P and TSR are required as inputs. The power coefficient directly follows from the assumption of no rotational losses, resulting in the 1D expression for power in Equation A.3. For the tip-speed ratio, the parametrisation of Equation 3.40 for an IEA-15MW reference turbine is used, which results in $U_r = 10.59 \frac{m}{s}$ and $\lambda_r = 9.0$ [32]. The freestream velocity is obtained from the thrust curve parametrisation of Equation 3.38. Using these inputs, the induction profile of Figure A.1 is obtained.

$$a_{1D} = \frac{1}{2}(1 - \sqrt{1 - C_T}) \quad (\text{A.2})$$

$$C_P = 4a(1 - a)^2 \quad (\text{A.3})$$

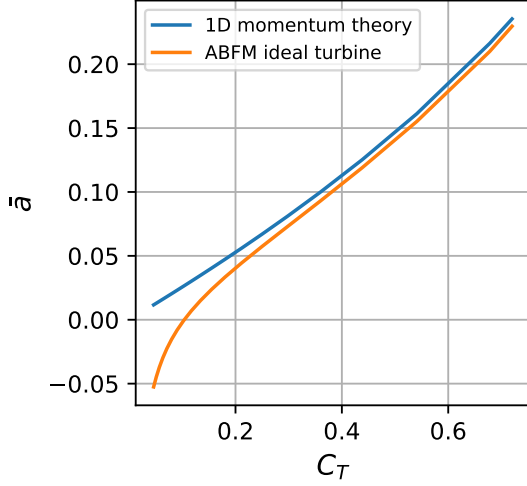


Figure A.1: The $\bar{a} - C_T$ curve for an ideal turbine with no rotational losses in the wake, according to 1D momentum theory and the homogeneous ABFM

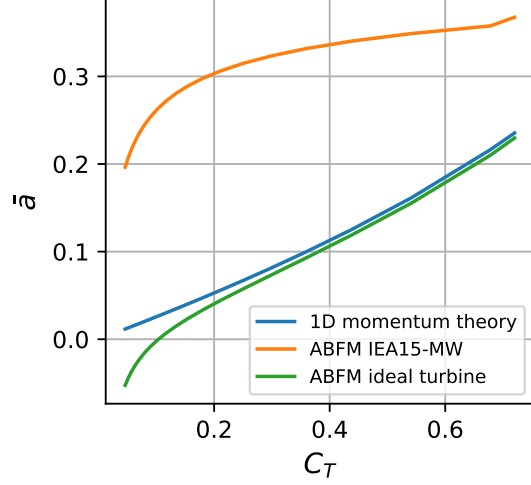


Figure A.2: The $\bar{a} - C_T$ curve of the ABFM based on the parametrised turbine curves of the IEA-15MW Reference turbine, compared to an ideal turbine and the 1D approximation

It can be seen that the induction from the ABFM matches the expected 1D profile quite well for moderate to high thrust coefficients. The outcome is slightly lower, because the ABFM by design accounts for the effect of the TSR. For $C_T < 0.3$, corresponding to low tip-speed ratios, the solution becomes significantly worse. For $C_T < 0.1$ the prediction induction even becomes negative, which is no longer a physical result. Still, for most operating conditions, the results are usable.

However, a real turbine will have significant losses in the wake. In this case, Equation A.2 most often still gives good results, but Equation A.3 is very optimistic in practice. Consider the IEA-15MW reference turbine, which has $C_{T_r} = 0.72$ and $C_{P_r} = 0.456$ [32]. Using the 1D approximation, on the other hand, would result in $a = \frac{1}{2}(1 - \sqrt{1 - C_T}) \approx 0.24$, which gives $C_P = 4a(1 - a)^2 = 0.55$. Therefore, the calculation has been repeated, but now the input C_P for the ABFM is determined from the turbine curve of Equation 3.39. This results in Figure A.2.

Although this turbine experiences significant wake losses, Equation A.2 is expected to still be a reasonable approximation of the expected induction. Then it is clear from Appendix A that the ABFM does not predict the induction of the IEA-15MW turbine. Instead, it greatly overpredicts the value for every thrust coefficient.

The reason for this can be understood by investigating the behavior of the ABFM. By considering the IEA-15MW, the input power coefficient is considerably lower than for an ideal turbine. From Equation 3.17 it then follows that the disk velocity is lower, resulting in a higher induction factor. This does neglect the coupling between u_d and q_0 through $F(x)$, but generally speaking this coupling effect is very small.

Further insights can be found by combining Equation 3.17, Equation 3.14, Equation 3.5 and Equation A.1. Rearranging the terms, Equation A.4 is obtained. As the integral is always positive, it can be concluded that an upper bound to this equation is given by Equation A.5. Noteworthy is that this upper bound is equivalent to Equation A.3. Thus, the term $2 \int_0^1 (\frac{u_\theta}{U_0})^2 x dx$ can be directly interpreted as wake losses.

$$\bar{a}_{ABFM} = 1 - \frac{C_P}{C_T - 2 \int_0^1 (\frac{u_\theta}{U_0})^2 x dx} \quad (\text{A.4})$$

$$\bar{a}_{upper} = 1 - \frac{C_P}{C_T} \quad (\text{A.5})$$

Looking at Figure A.3, it can be concluded that the ABFM generally predicts an induction value that is quite close to the upper bound and that thus the wake loss term is small with respect to C_T . By inspecting Equation 3.2 it can be seen that this corresponds to the induced azimuthal velocity being

small with respect to the tangential velocity of the turbine blade. Looking back at Figure 4.2 and Figure 4.3, this is a fair assumption, except for $x \approx \bar{\delta}$ at low tip-speed ratios. This explains why at low thrust coefficients, which are correlated to low TSR, the ABFM diverges further from this upper bound, as seen in Figure A.3.

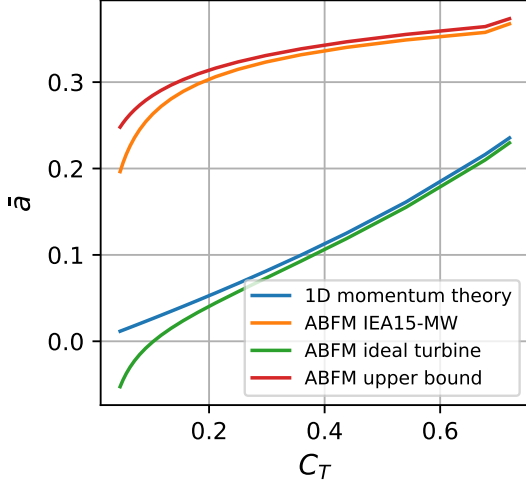


Figure A.3: The induction predicted by the ABFM for the IEA-15MW reference turbine, as compared to the upper bound for the induction

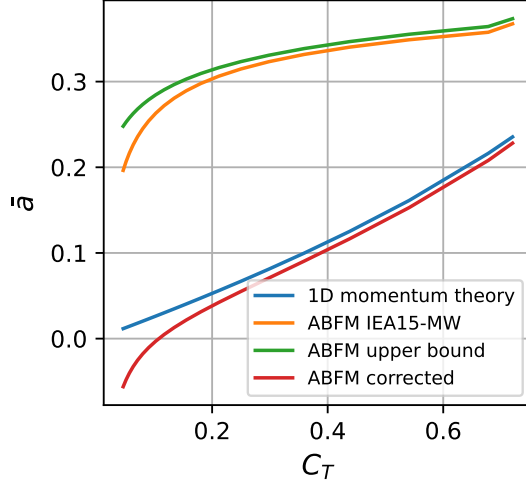


Figure A.4: Correction of the induction of the ABFM using Equation A.7. The upper bound and 1D approximation are given as a reference

This suggests that the wake losses predicted by the ABFM are too small. As such, the induction can only be predicted correctly if turbines with very low wake losses are considered, which matches with the observations in Figure A.1, where the ideal turbine induction is correctly resolved.

Interestingly enough, the observation that the ABFM induction is close to the upper bound can be used to define a correction. Combining Equation A.5 and Equation A.2, Equation A.6 can be obtained. The corrected induction is then found by realising that $\bar{a}_{corrected} \approx \bar{a}_{1D}$ and $\bar{a}_{upper} = \bar{a}_{ABFM}$, which results in Equation A.7.

$$\bar{a}_{1D} = \frac{\frac{1}{2}C_T(1 + \sqrt{1 - C_T})(\bar{a}_{upper} - 1)}{C_P} + 1 \quad (\text{A.6}) \quad \bar{a}_{corrected} = \frac{\frac{1}{2}C_T(1 + \sqrt{1 - C_T})(\bar{a}_{ABFM} - 1)}{C_P} + 1 \quad (\text{A.7})$$

The correction is plotted in Figure A.4. It can be seen that after the correction, the prediction is similar as for the ideal turbine in Figure A.1 and agrees well with the induction obtained from 1D momentum theory for most operating conditions.

One could wonder if the ABFM is even a useful model if it cannot predict the induction factors correctly. After all, the force distribution of Equation 3.4 is calculated directly from this factor. One would thus expect that the resulting forces would also be wrong. However, this turns out to not be the case. After all, the thrust and power coefficient are given as an input to the model, which ensures that the integral of the curves match. On top of that, most physics are captured good enough to represent the shapes of the distributions with acceptable accuracy. The model has been validated for different turbines and a large range of operating conditions. Although not all results are perfect, the results are quite realistic[72]. Still, based on the analysis of the current section it is expected that the wake losses are not fully captured and future models could improve this by further studying this behavior.

A.2. Consequences for Coupling the ABFM

In section A.1 it was seen that the ABFM does not always correctly model the induction, and thus the disk velocity. However, existing coupling approaches rely on providing the disk velocity to the model,

which can give inconsistencies if not accounted for. In subsection A.2.1 it will be discussed how current literature deals with this. The approach will then be generalised in subsection A.2.2.

A.2.1. Understanding the Coupling Procedure of Current Literature

For as far as known, coupling the ABFM to a LES has only been performed by Sørensen et al.[75] and Navarro Diaz et al.[49]. Their approach is largely the same and is based on providing the distribution of disk velocity, $u_d(x, \theta)$, as an input to the ABFM.

This is because the rotor plane is resolved in the LES and as such $u_d(x, \theta)$ is directly available. However, in the system of equations of Equation 3.14 and Equation 3.15, q_0 and u_d were taken as the degrees of freedom, giving $q_0 = f(u_d, C_T, C_P, \lambda, U_0)$ and $u_d = f(q_0, C_T, C_P, \lambda, U_0)$. However, since the disk velocity is provided as an input, the power is already determined. Trying to provide C_P as an input to the system will over-constrain the model. Alternatively, C_P can be seen as the new degree of freedom of the model, which is chosen such that Equation 3.15 is satisfied.

Since C_P is constrained, it is useful to know what value it will become. In section A.1 it was seen that if the C_P was obtained from a turbine curve, thus accounting for wake losses, the resulting induction would be unrealistically high, causing a severe underprediction of u_d . Only if the C_P value was chosen according to Equation A.3 for normal turbine operating conditions, ignoring all wake losses, would the disk velocity be accurately resolved.

Reversing this logic, if a realistic u_d is provided as input, as would be the case when LES values are used, the resulting C_P would collapse onto the 1D solution of Equation A.3. In section A.1 this value was found to be roughly 0.55 in rated conditions for the IEA-15MW, which is more than 17% higher than the actual value, $C_{P_r} = 0.456$ [32]. If the aim was to resolve the tangential force distribution of the turbine blades, this method will therefore give a significant positive bias.

Also, as seen in Figure A.1, the ABFM induction also fails for ideal turbines if $C_T < 0.3$. As such, it is expected that directly providing u_d to the ABFM will not give good results for these cases. All coupling attempts in literature[75, 49] only consider sub-rated speeds and therefore did not encounter this problem.

Still, the approach is not wrong per se. It enables a successful coupling of the LES to the ABFM, which allows the effects of turbulence on the loading to be studied. However, for many real-life practices, it is of great importance that the load distributions are consistent with the integral thrust and power of the turbine. With this coupling approach, this will not be the case if turbine curve values are used.

A.2.2. Generalising the Coupling Procedure

For many practical purposes it is desired to keep the power coefficient as an input to the model. This ensures that the integral of the force distributions matches the thrust and power curve. It was already seen that providing $u_{d_{LES}}$ results in an overestimation of the power. Since the ABFM overestimates the induction, it can thus be concluded that the correct power can only be obtained by providing a value of $u_{d_{ABFM}} < u_{d_{LES}}$. One thus has to actively differentiate between these two values, where only $u_{d_{LES}}$ has a physical meaning and this velocity should thus be used to evaluate all freestream conditions.

One possible way to do this is to apply Equation A.7 to map $u_{d_{LES}}$ into $u_{d_{ABFM}}$ before providing it to the model. The resulting disk velocity is no longer physical, but it is known that this is always the case if the ABFM is to predict a realistic power output. An advantage of this approach is that the complete distribution can be sampled and given as an input, such that the effect of turbulence on the tangential force distribution can be resolved. However, Equation A.7 is not perfect and also $u_{d_{LES}}$ is generally a bit too high due to smearing effects. Since the disk distribution is still explicitly provided to the ABFM, the exact power can still not be controlled and will not match the turbine curve exactly. However, the result will be closer to the actual power than when no correction is applied.

However, there is another option. Since it is desired to match the exact power of the power curve, the power coefficient has to be provided as an input. The only way to not overconstrain the system of equations is then to keep the disk velocity as an unknown. In this case, $u_{d_{ABFM}}$ does not carry much physical meaning anymore, but is used as a tuning parameter for the model. However, the system of equations can only be solved for 2 degrees of freedom, one of which is the rotor circulation, while u_d is

an entire distribution. It can be assumed that $u_{d_{ABFM}} = \text{constant}$, however, this way $u_{d_{LES}}$ is no longer coupled to the tangential force, such that turbulent influences are not resolved in Equation 3.4.

Instead, the distribution of disk velocity can be described by Equation 3.24, which maps the turbulence intensity of $u_{d_{LES}}$ onto $\overline{u_{d_{AFBM}}}$. For every input power coefficient, the system of equations will then converge to a value where $\overline{u_{d_{AFBM}}}$ satisfies this power.

It should be noted that this approach is a generalisation of the approach from literature. If $C_P = 4a(1 - a)^2$ is provided as an input, according to an ideal turbine with no wake losses, the resulting forces coincide with the case $u_{d_{LES}} = u_{d_{ABFM}}$, which is used to couple the model to LES in literature. However, by interpreting $u_{d_{ABFM}}$ as a tuning parameter, the user gains more freedom in how to use the model. Since the power coefficient can be given as an input, any turbine can be simulated with the correct integral power, as long as the turbine curve is available. Also, where the $u_{d_{LES}} = u_{d_{ABFM}}$ method is expected to perform poorly for $C_T < 0.3$, this generalisation actively accounts for mismatches in the induction and thus can still give reliable results.

B

BEM Model

Blade Element Momentum theory is a very popular method for estimating turbine loading, due to its combination of simplicity, efficiency, and accuracy. In this thesis, BEM will be used as reference material for verification and validation purposes.

Many different BEM solvers are available, but for this work OpenFAST[50] will be used. OpenFAST is an open-source turbine modeling software developed by NREL. It consists of a variety of different modules that can be used to assess the behavior of the turbine aerodynamics, structural properties, controller behavior and much more.

However, for this work, the main interest is verifying the ability of the ABFM to capture the aerodynamics of different turbine operating conditions. This will be analysed using the AeroDyn module[46], without further coupling to other FAST programs.

Apart from that, the tower module of AeroDyn is disabled, as no tower was included in the LES either. The effect of shaft tilt, overhang and precone are neglected and unsteady airfoil aerodynamics are not included. At the tip and the hub the Prandtl correction factor is applied.

To simulate a turbine, OpenFAST needs a definition of the entire geometry of the rotor. This includes twist and airfoil distributions along the radial coordinate and lift and drag polars for these airfoils. The turbine of choice is the IEA-15MW Reference turbine, the required data of this turbine is openly available[27].

With this setup, OpenFAST can simulate the forces on a turbine for a given freestream velocity, rotor RPM, blade pitch angle, and rotor yaw angle. In this work, yaw will not be considered and will be set to 0 for all simulations.

For easy reference, the above inputs will be transformed into a set of reference turbine curves. This is done in the following way. First, the turbine curve is divided into two parts, corresponding to Region 2 and Region 3 in Figure 3.5, for these regions the same control logic as in the turbine curve parametrisation of subsection 3.2.1 will be used.

For Region 2 it is assumed that the turbine is RPM-controlled and operating at zero blade pitch and constant tip speed ratios. The TSR was chosen such that the power is maximised, which was iteratively found to occur at $\lambda = 9.158$. The turbine thrust, power and load distributions below rated velocity can then be found by performing an OpenFAST run with these settings.

For region 3 it is assumed that the Rotor RPM is constant and equal to the RPM at rated velocity. In this region the turbine is blade pitch regulated and the value of the blade pitch is found iteratively, such that rated power is obtained.

Below cut-in speed and above cut-out speed, the thrust, power and rotor rpm are summed to be 0. The resulting turbine curves of thrust, power, rpm, and blade pitch are shown in Figure B.1, Figure B.2, Figure B.3, and Figure B.4, respectively. These curves have been generated for a uniform inflow. If

a sheared inflow is desired, for Region 2 the simulation can simply be repeated while providing the correct shear coefficient to OpenFAST. In Region 3, the pitch of the blades will have to be adjusted slightly to ensure that the turbine is still operating at rated power.

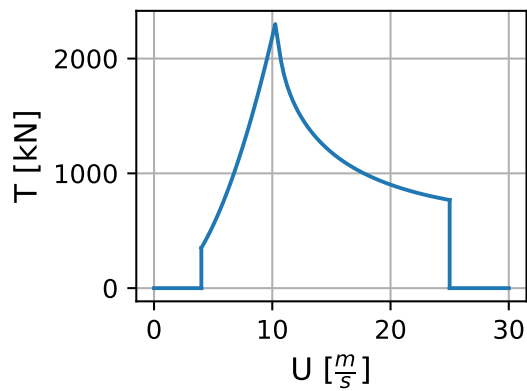


Figure B.1: Reference thrust curve of the IEA-15MW Reference turbine

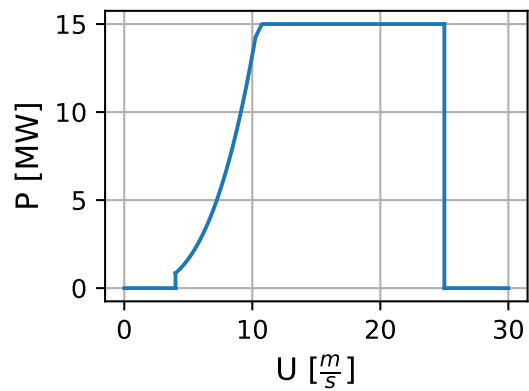


Figure B.2: Reference power curve of the IEA-15MW Reference turbine

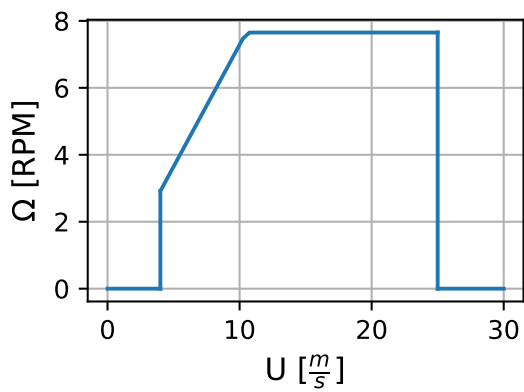


Figure B.3: Reference turbine RPM curve of the IEA-15MW Reference turbine

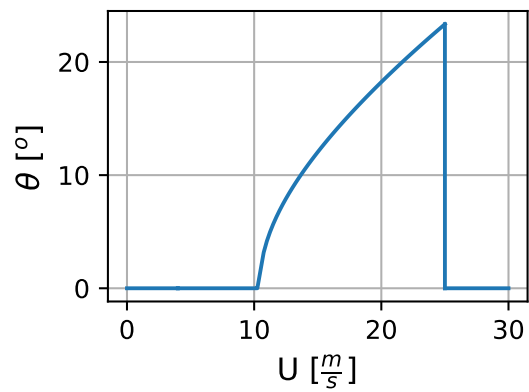


Figure B.4: Reference blade pitch curve of the IEA-15MW Reference turbine